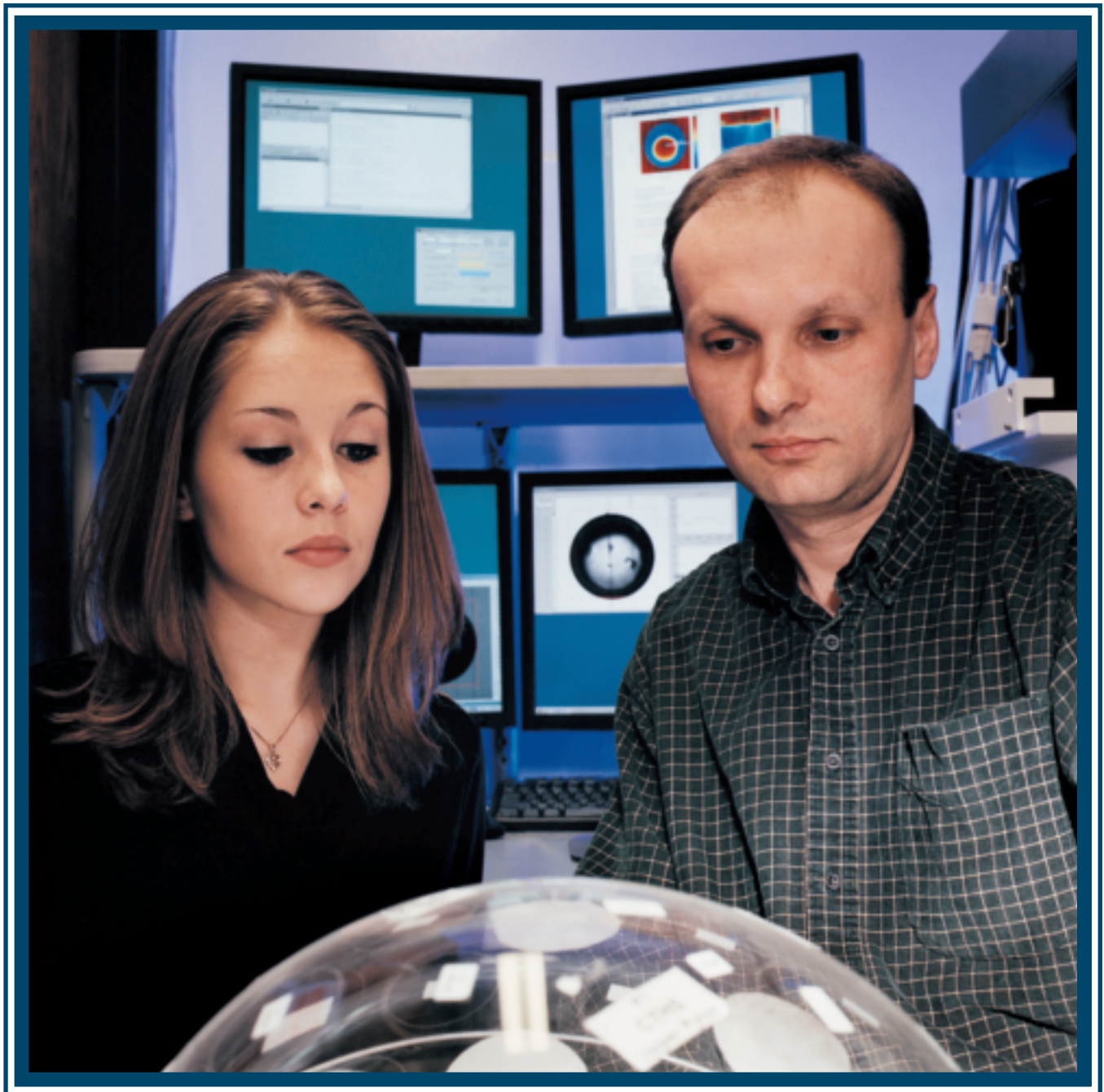


LLE Review

Quarterly Report



About the Cover:



The cover photograph shows Scientist Vladimir Smalyuk and Greece Arcadia High School senior Nicole Toscano (also a participant of LLE's 2003 Summer High School Research Program) discussing diagnostic configuration on OMEGA. The results of their experiment, presented in this issue, contain the characterization of a temperature-density profile of the cryogenic D₂ target at peak neutron production.

This report was prepared as an account of work conducted by the Laboratory for Laser Energetics and sponsored by New York State Energy Research and Development Authority, the University of Rochester, the U.S. Department of Energy, and other agencies. Neither the above named sponsors, nor any of their employees, makes any warranty, expressed or implied, or assumes any legal liability or responsibility for the accuracy, completeness, or usefulness of any information, apparatus, product, or process disclosed, or represents that its use would not infringe privately owned rights. Reference herein to any specific commercial product, process, or service by trade name, mark, manufacturer, or otherwise, does not necessarily constitute or imply its endorsement, recommendation, or favoring by

the United States Government or any agency thereof or any other sponsor. Results reported in the LLE Review should not be taken as necessarily final results as they represent active research. The views and opinions of authors expressed herein do not necessarily state or reflect those of any of the above sponsoring entities.

The work described in this volume includes current research at the Laboratory for Laser Energetics, which is supported by New York State Energy Research and Development Authority, the University of Rochester, the U.S. Department of Energy Office of Inertial Confinement Fusion under Cooperative Agreement No. DE-FC03-92SF19460, and other agencies.

Printed in the United States of America
Available from
National Technical Information Services
U.S. Department of Commerce
5285 Port Royal Road
Springfield, VA 22161

Price codes: Printed Copy A03
Microfiche A01

For questions or comments, contact Valeri N. Goncharov, *Editor*, Laboratory for Laser Energetics, 250 East River Road, Rochester, NY 14623-1299, (585) 275-5877.

Worldwide-Web Home Page: <http://www.lle.rochester.edu/>

LLE Review



Quarterly Report

Contents

In Brief	iii
Direct-Drive Cryogenic Target Implosion Performance on OMEGA	1
Hot-Core Characterization of a Cryogenic D ₂ Target at Peak Neutron Production in a Direct-Drive Spherical Implosion	11
Extended X-Ray Absorption Fine Structure Measurements of Laser Shocks in Ti and V and Phase Transformation in Ti	16
Picosecond Response of Ultraviolet Photodiodes on GaN	25
Self-Assembly of Coated Colloidal Particles for Optical Applications	28
A Tunable, High-Repetition-Rate, Harmonically Mode-Locked, Ytterbium Fiber Laser	36
Deterministic Microgrinding, Lapping, and Polishing of Glass-Ceramics	40
Publications and Conference Presentations	

In Brief

This volume of the LLE Review, covering October–December 2003, features “Direct-Drive Cryogenic Target Implosion Performance on OMEGA,” by P. W. McKenty, J. A. Delettrez, L. M. Elasky, R. Epstein, A. Frank (University of Rochester and LLE), V. Yu. Glebov, V. N. Goncharov, D. R. Harding, S. Jin, J. P. Knauer, R. L. Keck, S. J. Loucks, L. D. Lund, R. L. McCrory, F. J. Marshall, D. D. Meyerhofer, S. P. Regan, P. B. Radha, S. Roberts, W. Seka, S. Skupsky, V. A. Smalyuk, J. M. Soures, K. A. Thorp, and M. Wozniak; J. A. Frenje, C. K. Li, R. D. Petrasso, and F. H. Séguin–PSFC-MIT; K. A. Fletcher, S. Padalino, and C. Freeman–SUNY, Geneseo; and N. Izumi, J. A. Koch, R. A. Lerche, M. J. Moran, T. W. Phillips, G. J. Schmid, and C. Sorce–LLNL (p. 1). Layered and characterized cryogenic D₂ capsules have been imploded using high-contrast pulse shapes on the 60-beam OMEGA laser at the Laboratory for Laser Energetics. These experiments measure the sensitivity of the direct-drive implosion performance to parameters such as the inner-ice-surface roughness, the adiabat of the fuel during the implosion, and the laser power balance. The goal is to demonstrate a high neutron-averaged fuel ρR with low angular variance using a scaled $\alpha \sim 3$ ignition pulse shape driving a scaled all-DT ignition capsule. Results are reported with improvements over previous experiments in target layering and characterization and in laser pointing and target positioning on the OMEGA laser. These capsules have been imploded using up to 23 kJ of 351-nm laser light with an on-target energy imbalance of less than 2% rms, full beam smoothing (1-THz bandwidth, 2-D SSD, and polarization smoothing), and new, optimized, distributed phase plates. Pulse shapes include high-adiabat ($\alpha \sim 25$) square pulses and low-adiabat ($\alpha < 5$) shaped pulses. The data from neutron and charged-particle diagnostics, as well as static and time-resolved x-ray images of the imploding core, are compared with 1-D and 2-D numerical simulations. Scaling of target performance to a weighted quadrature of inner-ice roughness at the end of the acceleration phase is investigated.

Additional highlights of research presented in this issue include the following:

- V. A. Smalyuk, J. A. Delettrez, S. B. Dumanis (visiting scientist, Columbia University), R. Epstein, V. Yu. Glebov, D. D. Meyerhofer, P. B. Radha, T. C. Sangster, C. Stoeckl, and N. C. Toscano; J. A. Frenje, C. K. Li, R. D. Petrasso, and F. H. Séguin–PSFC-MIT; and J. A. Koch–LLNL (p. 11) characterize the compressed-core, temperature-density profiles of a cryogenic deuterium (D₂) target using measured primary deuterium–deuterium (DD) and secondary deuterium–tritium (DT) yields, neutron-averaged ion temperature, and x-ray images at peak neutron production. In addition, the authors infer the electron pressure and the areal density of the neutron production region to be 2.7 ± 0.4 Gbar and ~ 10 mg/cm², respectively.
- B. Yaakobi, D. D. Meyerhofer, and T. R. Boehly; J. J. Rehr–Dept. of Physics, University of Washington; B. A. Remington, P. G. Allen, and S. M. Pollaine–LLNL; and R. C. Albers–LANL (p. 16) use a laser-source-based, extended x-ray absorption fine structure (EXAFS) measurement to study the properties of laser-shocked metals on a nanosecond time scale. The ability of measuring shock-induced temperatures of the order of 0.1 eV is essentially unique to EXAFS. EXAFS measurements of vanadium shocked to ~ 0.5 Mbar with a 3-ns laser pulse yield a compression and temperature in good agreement with hydrodynamic simulations and shock-speed measurements. In laser-shocked titanium at the same pressure, the EXAFS modulation damping is much higher than warranted by the increase in temperature. This is explained by the α -Ti to ω -Ti phase transformation

known to occur around ~ 0.1 Mbar in the longer (μs) shocks obtained in gas-gun experiments. In the ω -Ti phase, the disparate neighbor distances cause a beating of the modulation frequencies and thus an increased damping. These results demonstrate that EXAFS measurements can be used for the study of nanosecond-scale shocks and phase transformations in metals.

- J. Li and W. R. Donaldson (p. 25) tested metal–semiconductor–metal ultraviolet photodiodes fabricated on GaN in the picosecond regime with an electro-optic sampling system. The best performance of a device with a feature size of $1\ \mu\text{m}$ showed a 1.4-ps rise time and 3.5-ps full width at half maximum, which represents the fastest ultraviolet GaN photodiode reported to date. The derived electron velocity in GaN was in good agreement with an independent photoexcitation measurement. A comparison with Monte Carlo simulation was made, and slower impulse response observed in a device with a smaller feature size of $0.5\ \mu\text{m}$ was discussed.
- M. Z. Yates, C. Wolfe, J.-C. Lin, and F. Caruso (Dept. of Chemical Engineering, University of Rochester) (p. 28) consider photonic crystals that offer great promise in a variety of applications in optoelectronics, from lasers to the creation of all-optical circuits for computing. The presented research project focuses on the creation of novel photonic crystals through the self-assembly of core-shell structured colloidal particles. Layer-by-layer electrostatic self-assembly was used to deposit polyelectrolyte shells around spherical colloidal particles. By exploiting electrostatic attraction, shells of controllable thickness were formed by alternating the deposition of positive- and negative-charged polyelectrolytes. The coated colloidal particles were deposited as thin films of hexagonally close-packed crystals onto glass slides. The crystalline films display a partial photonic band gap and preferentially reflect light of a wavelength dependent on the size of the particles making up the crystal. The chemical functional groups in the shell surrounding the colloidal particles offer a potential route to immobilize optically active species in the shell to enhance the photonic band gap of the crystal.
- N. Usechak, G. Agrawal, and J. D. Zuegel (p. 36) report on a ytterbium fiber laser mode-locked at its 280th harmonic, which corresponds to a repetition rate greater than 10 GHz. The laser produces linearly polarized, 2.6-ps chirped pulses with up to 38 mW of average output power. The mode-locked pulses are tunable over a 55-nm window centered on 1053 nm.
- J. C. Lambropoulos [also Dept. of Mechanical Engineering and the Center for Optics Manufacturing (COM)], B. E. Gillman (Zygo Corp.), S. D. Jacobs (also COM), and H. J. Stevens (Corning, Inc.) (p. 40) report on a series of microgrinding and polishing experiments on glass-ceramics. Microgrinding includes deterministic microgrinding (fixed infeed rate) and loose-abrasive lapping (fixed pressure). Material mechanical properties (Young's modulus, hardness, fracture toughness) and chemical properties (chemical susceptibility, or mass loss under chemical attack) are correlated with the quality of the resulting surface (surface microroughness and surface grinding-induced residual stresses). Deterministic microgrinding (at fixed infeed) and loose-abrasive microgrinding (at fixed pressure) are compared in terms of material removal rates and resulting surface quality.

Valeri N. Goncharov
Editor

Direct-Drive Cryogenic Target Implosion Performance on OMEGA

Introduction

Direct-drive, cryogenic inertial confinement fusion (ICF) capsule implosion experiments under investigation using the 30-kJ OMEGA laser system¹ at LLE will validate the scaled-ignition performance of low-adiabat, cryogenic DT capsules. This validation is pivotal in the development of direct-drive ignition target designs for the 1.6-MJ National Ignition Facility² (NIF), currently under construction at the Lawrence Livermore National Laboratory. The physical limitations of the target fabrication and laser subsystems on the NIF, however, place restrictions on the robustness of ICF ignition designs. Demonstrating the viability of the ignition designs driven under a variety of perturbation scenarios is critical to the success of direct-drive ICF.

Target designers have, in the past, had to trade target performance (thermonuclear gain) for increased target stability.³ Many studies have been undertaken to examine the minimum laser energy required to achieve ignition.^{4–7} All of these studies have concluded that the minimum energy required for ignition scales as $\sim\alpha^2$, where α is the shell adiabat, defined as the ratio of the local pressure to the Fermi-degenerate pressure. As the compressibility of the fuel is increased (α decreased), less laser energy is required to achieve ignition; however, more-compressible fuel develops thinner fuel layers during the implosion, resulting in reduced stability and, potentially, layer failure. As the nonuniformity levels are reduced, it becomes possible to field targets with lower fuel adiabat, examining regions of higher target gain for fixed laser energy. Eventually, targets with a fuel adiabat approaching $\alpha = 1$ will be used in direct-drive ignition.

The cryogenic implosion campaign at LLE is a staged program comprised of several concurrent efforts including experimental validation of target performance for progressively lower fuel adiabat target designs employing cryogenic D₂ fuel; physical minimization of the interfacial cryogenic surface roughness; and ultimately the implosion of cryogenic DT targets on the OMEGA laser system. Recent advances in all three of these efforts have LLE poised to demonstrate

scaled-ignition performance with DT on OMEGA by the end of FY05. Significant progress has been made in cryogenic implosion experiments evaluating target performance with high-adiabat solid-D₂ and wetted-foam targets and low-adiabat solid-D₂ targets. It has been shown that there is good agreement between the experimental observables and the results of two-dimensional *DRACO*⁸ simulations for targets imploded near target chamber center (TCC). The use of adiabat shaping⁹ has been shown theoretically to lead to increased stability for both the “all-DT” and wetted-foam direct-drive NIF point designs and the corresponding ignition-scaled experiments for OMEGA. Dramatic advances in cryogenic layer characterization and layering over the last year have resulted in the production of sub-2- μm inner surface ice layers in targets for implosion on OMEGA. The cryogenic DT fill and transfer station (FTS) is currently being qualified and will be DT-charged by the end of this fiscal year. With this system in place, full-scale layering studies of cryogenic DT targets will be undertaken, resulting in the fielding of ignition-scale cryogenic DT experiments on OMEGA.

This article reviews the performance characteristics of recent OMEGA cryogenic implosion experiments and outlines the theoretical basis for new cryogenic experiments that will examine low, $\alpha = 2$ implosions for OMEGA. In the following sections, (1) the experimental setup is presented; (2) results of the implosion experiments are compared with results from one- and two-dimensional (1-D, 2-D) radiation-hydrodynamics simulations; (3) the direct-drive ignition design is optimized for better hydrodynamic stability using a picket prepulse; and (4) the scaling of this design to OMEGA operating conditions is examined. Conclusions are presented in the last section.

Experimental Setup

1. Laser-System Configuration

Cryogenic capsules were imploded using two pulse shapes: a high-adiabat ($\alpha \sim 25$), 23-kJ, 1-ns square pulse and a low-adiabat ($\alpha \sim 4$), 17-kJ, 2.5-ns shaped pulse. The $\alpha \sim 4$ pulse shape has been scaled from the standard all-DT as shown in

Fig. 97.1. Full beam smoothing techniques were applied to each pulse using distributed phase plates (DPP's),¹⁰ polarization smoothing with distributed polarization rotators (DPR's),¹¹ and 2-D, single-color-cycle, 1-THz smoothing by spectral dispersion (SSD).¹² Laser power balance was optimized using techniques employing x-ray fluence measurements of standard OMEGA pointing targets.¹³ With these techniques the variance of incident energy imbalance among all 60 OMEGA beams is $\sim 2\%$ rms, with a 4- to 5-ps rms mistiming when taken to target.

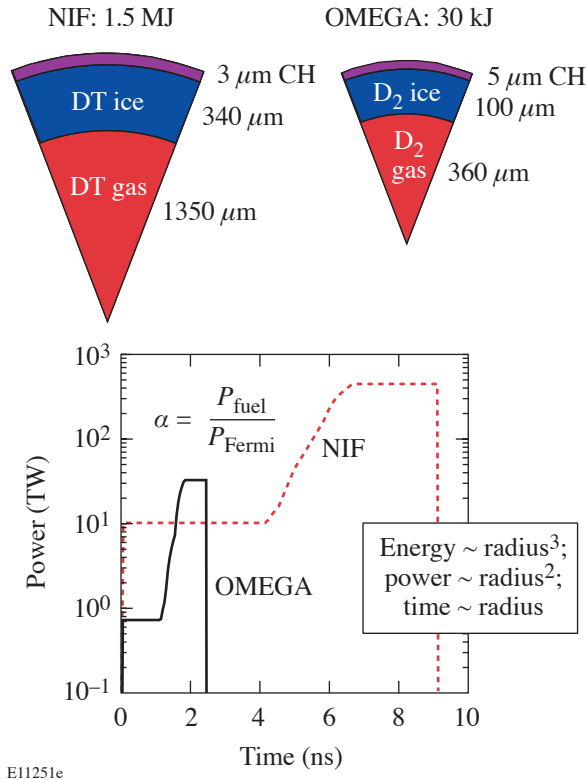


Figure 97.1
The direct-drive NIF point design target is shown with the corresponding OMEGA $\alpha = 4$, energy-scaled capsule. The scaled pulse shapes are given in the inset.

2. Capsule Metrology and Layering

Capsules used in these experiments fell into one of two categories: utilizing fuel layers comprised of either solid D_2 (SD) or a D_2 wetted-foam (WF) layer over a solid D_2 layer. The SD target employs a thin, plastic outer shell composed of a “strong GDP” (glow discharge polymer) (a high-strength plastic, $CH_{1.1}$ $\rho \sim 1.20$ g/cc) approximately $4 \mu\text{m}$ thick. This shell, nominally $850 \mu\text{m}$ in diameter, is permeation filled with

D_2 to pressures at room temperature in excess of 1000 atm, which, when properly cooled, forms an ice layer of approximately $100 \mu\text{m}$. Layering this surface requires the proper selection of the triple-point isotherm in the capsule, cooling gas pressure, and IR heating laser energy input. Currently a quality layer ($< 2 \mu\text{m}$ rms) requires several days of technician time. Optimization of this effort is being studied. Layer roughness for this study spanned a range of values from 2 to $7 \mu\text{m}$ rms.

The WF shell used in these experiments was not optimized for implosion on OMEGA but was part of initial foam-ice layering studies in collaboration with General Atomics. The shell consisted of a $4\text{-}\mu\text{m}$ CH layer overcoating a $62\text{-}\mu\text{m}$ foam shell. The foam had a dry density of 120 mg/cc, with fibers consisting of the same GDP mentioned above and an average cell size of less than $1 \mu\text{m}$. This shell underwent the same permeation fueling as the standard SD cryogenic target, which resulted in an inner ice layer estimated to be $65 \mu\text{m}$ in depth. Accurate knowledge of the wetted-foam density and the resultant ice-layer thickness depends on the modeling of the freezing of the liquid D_2 fuel within the foam matrix. For this experiment it was assumed that the foam, as it was cooled, became impermeable to the liquid D_2 , preventing any diffusion of liquid D_2 in or out of the foam matrix. Conserving mass, the wetted-foam density remains constant (~ 240 mg/cc) as densification proceeds.

While characterization of WF targets remains an issue due to significant diffraction of the incident probe light, the SD targets are characterized with white-light shadowgraphy similar to that first proposed and implemented by Koch.¹⁴ The shadowgraphy technique produces a wealth of experimental signal represented by a series of rings in the target image plane. Recent analysis¹⁵ has identified the source of the faint trace rings and confirmed the validity of the “bright ring” as the primary carrier of information about the interfacial ice roughness. After processing the information for a particular target orientation, the target is rotated about its polar axis and another sample is taken and processed. Such information can then be interpolated and processed to give a full, 3-D representation of the inner ice surface. The number of experimentally obtained traces, as was pointed out by Stephens,¹⁶ limits the spatial scale of this representation. OMEGA capsules undergo a minimum of 20 roughness scans, which describe the amplitude and nature of the first ten spherical harmonics. Complete spectral decomposition of the ice surface would require more than a hundred angular samples.

3. Target Positioning

Sangster¹⁷ reported the early problems with positioning cryogenic targets in the center of the OMEGA target chamber. At the heart of this problem was static mis-positioning due to image distortion through the shroud windows and dynamic mis-positioning due to target vibration. The static mis-positioning was corrected with careful and detailed procedures comparing and documenting the position of surrogate targets as viewed through the shroud windows and their true position after the shroud was retracted. Each of the four moving cryogenic transfer carts (MCTC's) was examined and given a unique set of positioning reticules for use with target experiments.

The target vibration was caused by two problems: (1) the vibration induced to the target stalk as the cryogenic shroud, used to maintain the correct environment for the ice layer, was pulled away from the target before laser irradiation, and (2) an occasional, weak collision between the articulated target stalk and the cryogenic shroud during this retraction. Many engineering improvements were applied to the target shroud and the MCTC. The most effective of these included the modification to the shroud control software allowing a slower retraction of the shroud and the replacement of the articulated target stalks with a simple, narrower staple design. The slower retraction speed allows transmitted vibrations to self-damp, while the narrower stalk reduces the possibility of a collision between the target and the retracting shroud.

With these modifications in place, the static mis-pointing has now been reduced to less than $40\ \mu\text{m}$ for all of the MCTC's, while target vibration has been virtually eliminated. All target implosions discussed in this article were located within $40\ \mu\text{m}$ of TCC, with many achieving $20\ \mu\text{m}$ at shot time.

4. Diagnostics

Cryogenic implosions on the OMEGA laser system are diagnosed with a large number of instruments, including laser scattering and absorption diagnostics; time-dependent and time-integrated x-ray imaging; time-dependent and time-integrated x-ray spectroscopy; time-dependent and time-integrated fusion yield measurement; and fusion product spectroscopy. The fusion product diagnostics include measurements of both neutrons and charged particles. Data presented here include measurements from the time-integrated x-ray imaging, primary¹⁸ and secondary fusion yield,¹⁹ neutron²⁰ and proton spectroscopy,²¹ and time-dependent neutron and proton emission.²²

Time-integrated x-ray imaging is used to determine the position of the target at the time of the shot. These measurements are made with both x-ray pinhole cameras and x-ray microscopes. Three x-ray microscopes and five x-ray pinhole cameras located in fixed positions around the target chamber allow several views of the target emission to be recorded. Subsequent analysis of the images locates the position of the target to within $\pm 10\ \mu\text{m}$.

The primary and secondary fusion product yields are measured with a combination of activation, scintillation, and track detectors. These provide a direct measure of the implosion performance. The ratio of secondary to primary product yields is a measure of the final core conditions. Neutron spectroscopy is used to determine the ion temperature, and the proton spectroscopy determines the total areal density of the implosion from the energy loss measured by wedged range filters.²³

Time-dependent neutron emission is measured with a scintillator coupled to an optical streak camera. The time evolution of the fusion emission is sensitive to the overall coupling of the laser energy to the target, and the emission from both the shock wave and compression can be observed. These data and those taken from laser absorption measurements are used to determine the accuracy of the hydrodynamic simulation of the implosion.

Implosion Results

1. High-Adiabatic Pulses

The cryogenic implosion campaign is divided into several phases dealing with the validation of stable implosions with progressively lower fuel adiabat. The first phase of these implosions used a high-adiabat (1-ns square, $\alpha = 25$) laser pulse to minimize the effects of laser imprint on target performance. This allows experimental investigation of the effect of ice roughness on target performance. Implosions were carried out using several SD targets and one WF target. For brevity we will examine one SD shot in detail and then speak briefly about the wetted-foam shot.

The SD capsule used was $\sim 875\ \mu\text{m}$ in diameter and contained a $92\text{-}\mu\text{m}$ D_2 -ice layer surrounded by a $3.8\text{-}\mu\text{m}$ GDP wall. The inner ice roughness was measured to be $\sim 4\ \mu\text{m}$ rms when averaged over 23 views. The power spectrum, shown in Fig. 97.2(a), is heavily weighted toward the lowest end of the spectrum with $\sim 90\%$ of the power contained in the first few modes ($\ell = 1$ to 3). The capsule was determined experimentally¹³ to be offset $22\ \mu\text{m}$ from target chamber center at the

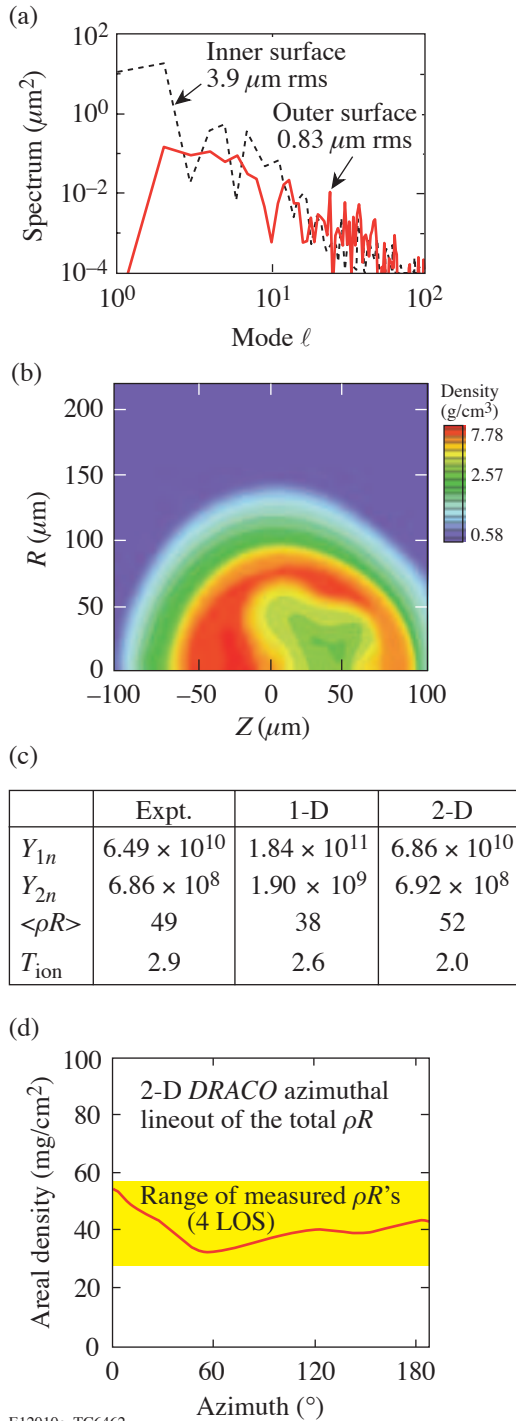


Figure 97.2

Two-dimensional *DRACO* input and results for shot 33599. (a) Input ice roughness spectrum, (b) isodensity contours drawn near the time of peak burn, (c) tabular comparison of secondary-neutron yields and neutron-averaged areal density and ion temperature, and (d) angular variation of the total areal density calculated from the isodensity contours. Yellow region represents the range of experimentally obtained areal-density measurements.

beginning of the implosion. This capsule produced a neutron yield of 6.5×10^{10} neutrons—roughly 36% of the simulated 1-D *LILAC*²⁴ yield. A *DRACO* simulation was run with the roughness spectra from Fig. 97.2(a) and an initial 4.4% rms $\ell = 1$ illumination nonuniformity corresponding to the 22- μm offset.¹³ The simulated neutron yield of 6.9×10^{10} falls very close to the experimental result. As can be seen from the isodensity contours given in Fig. 97.2(b) (taken near the time of peak neutron production), the core has developed under the strong influence of the low modes with the effect of the $\ell = 1$ and 2 most prominent. The secondary-proton yields and average-areal-density results, shown in Fig. 97.2(c), are also in good agreement between the experiment and the *DRACO* simulation. One of the more-interesting results from this implosion is the agreement between the range of experimentally observed areal-density measurements with those predicted by *DRACO* as shown in Fig. 97.2(d).

Additional results obtained for the other shots are compiled in Fig. 97.3. In Fig. 97.3 the experimental yield-over-clean [(YOC), the experimentally obtained yield divided by the 1-D simulated yield] for all shots in this series is compared with the trends of several series of perturbed *DRACO* simulations run with increasing initial ice roughness for a specific fixed target offset. The *DRACO* trend lines merge with increasing ice

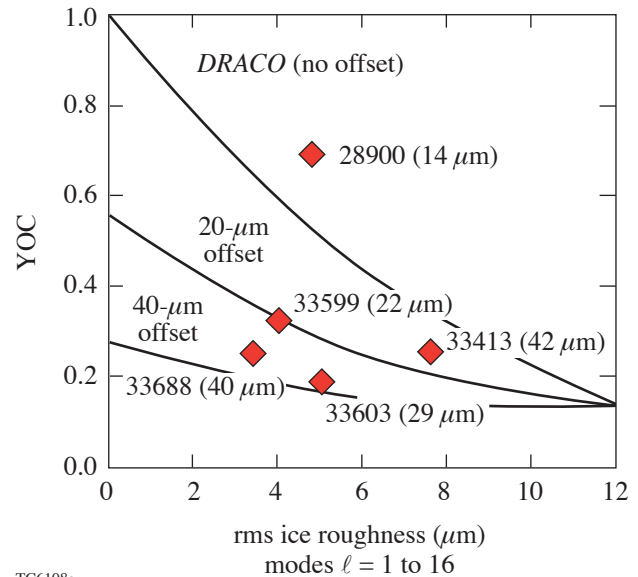


Figure 97.3

Analysis of experimental neutron YOC drawn as a function of the target's initial ice roughness. Curves are drawn for several series of *DRACO* runs analyzing the degradation of YOC with increasing ice roughness. Each of these series was computed with a different initial target offset.

roughness due to the dominance of the ice perturbation at these high levels. The experimental results are in good agreement with the *DRACO* predictions.

The other part of the high-adiabat cryogenic implosion series was the use of a WF target to measure the absorption fraction and shock speed in this material. Such experiments, carried out in spherical geometry, help to develop a predictive capability for target performance. The need for examining shock propagation within a wetted-foam matrix was pointed out earlier^{25,26} in theoretical studies analyzing shock propagation in foam. Studies at LLE use the 2-D astrophysical code AMRCLAW²⁷ that employs the adaptive-mesh-refinement (AMR) scheme to highly resolve the shock flow around and through the fiber elements. The results of such simulations are shown in Fig. 97.4 and indicate that shocks travel faster in wetted foam when compared to traditional Lagrangian hydrodynamics simulations that model the foam as a homogeneous mixture. Of particular interest to target designers, in addition to ascertaining the proper value of the shock velocity, are the perturbed nature of the shock front and mechanisms for the CH-DT homogeneous annealing in the wake of the shock. Both of these processes will be examined in more detail when a new three-dimensional (3-D) AMR code, ASTROBEAR,²⁷ becomes available.

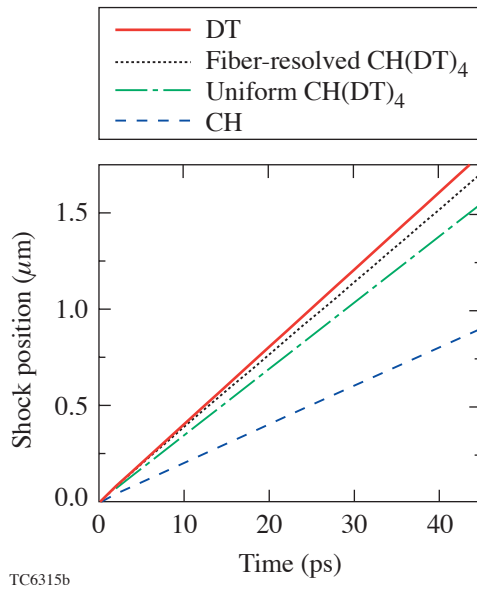


Figure 97.4 Numerical results detailing the difference in shock velocity for a variety of materials including CH, CH(DT)₄ mixture, fiber-resolved foam, and pure DT.

The first cryogenic wetted-foam implosion on OMEGA produced the highest-ever cryogenic neutron yield: 1.8×10^{11} . The target was imploded with the high-adiabat, 1-ns square pulse. The neutron burn history was obtained and is shown as the solid curve in Fig. 97.5. Several 1-D *LILAC* simulations were run with varying the wetted-foam density, and an example of the numerical burn history ($\rho_{WF} \sim 240$ mg/cc) is drawn as the dotted line in Fig. 97.5. Discrepancies between the simulated and experimental bang times may be attributed to lower shock velocities in low-density foams when modeled as a homogeneous mixture (as predicted in Refs. 25 and 26). The numerically obtained 1-D yield underestimates the experimental yield by roughly 15%.

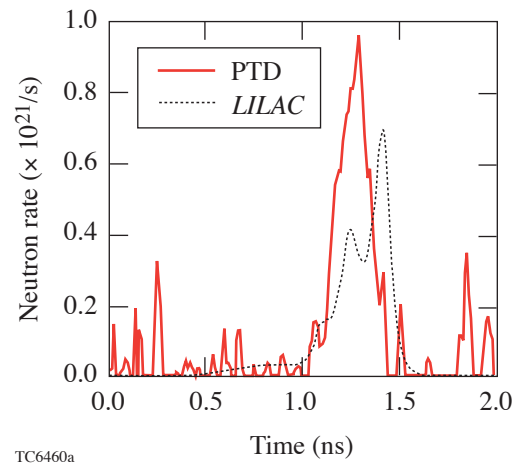


Figure 97.5 Comparison of neutron burn histories between the results of the particle temporal diagnostic (PTD) and *LILAC*.

Clearly, more work needs to be done in addressing the use of WF targets in ICF ignition experiments. Over the coming year we will repeat the spherical experiments for various density dry foams and couple this information with ongoing planar foam experiments studying shock transit with picket pulses in warm foams and standard shock development in cryogenic wetted foams. Additionally, techniques must be developed to characterize the ice layer within the foam shell.

2. Low-Adiabat Pulses

The next phase of the OMEGA cryogenic implosion program involves the validation of low-adiabat, ignition-scaled implosions on OMEGA. The first set of experiments in this phase employs the $\alpha = 4$ pulse shape, shown earlier in Fig. 97.1. Several implosions were undertaken using the

OMEGA laser, but, again, only a single SD shot will be described in detail.

The SD target was 865 μm in diameter with a 3.8-mm GDP overcoat, an ice layer of $\sim 92\text{-}\mu\text{m}$ depth, and an interior ice surface roughness of $\sim 4.5\ \mu\text{m}$. The power spectrum for this surface, as shown in Fig. 97.6(a), is again heavily weighted toward low-order modes. The capsule was determined to be 28 μm from target chamber center at the beginning of the implosion. The neutron yield for this implosion was 4.3×10^9 , which represents the highest-ever experimental yield obtained from a cryogenic $\alpha \sim 4$ implosion (YOC $\sim 16\%$). The spectra from Fig. 97.6(a) and an initial 5.6% $\ell = 1$ illumination nonuniformity, again due to the target offset, were used in a *DRACO* simulation (laser imprint was excluded from this calculation because the growth of these two perturbations, at these levels, overwhelms the effect of the imprint as was demonstrated in Ref. 3). The simulated yield was 5.9×10^9 . The secondary-yield comparison also showed the *DRACO* simulation slightly overpredicting the experimental result; however, the simulated average $\langle \rho R \rangle$ was again in good agreement as shown in Fig. 97.6(c) and the azimuthal variation in Fig. 97.6(d).

Previously,³ low-adiabat target performance has been presented as a compilation of all perturbation sources using a sum-in-quadrature representation of each source's contribution to the roughness of the inner ice layer at the end of the acceleration phase of the implosion. The scaling parameter $\bar{\sigma}$ is defined as

$$\bar{\sigma}^2 = 0.06 \times \sigma_\ell^2 (\ell < 10) + \sigma_\ell^2 (\ell \geq 10),$$

where σ_ℓ is the rms roughness computed over the mode range indicated. At this time during the implosion, this surface decouples from the ablation region of the target. As such, the effects of all major sources of perturbation leading to the initial seed of the deceleration-phase Rayleigh–Taylor (RT) instability have been set. An example of the $\bar{\sigma}$ scaling is shown in Fig. 97.7, where a comparison is made between the NIF $\alpha = 3$ and OMEGA $\alpha = 4$ designs.

Using the $\bar{\sigma}$ scaling with yield allows the experimental validation of the numerical modeling of current OMEGA experiments, which, in turn, lends credibility to the ability of these numerical models to predict ignition for direct-drive target designs on the NIF. The $\bar{\sigma}$ parameter and yield performance were extracted from the *DRACO* simulations of the

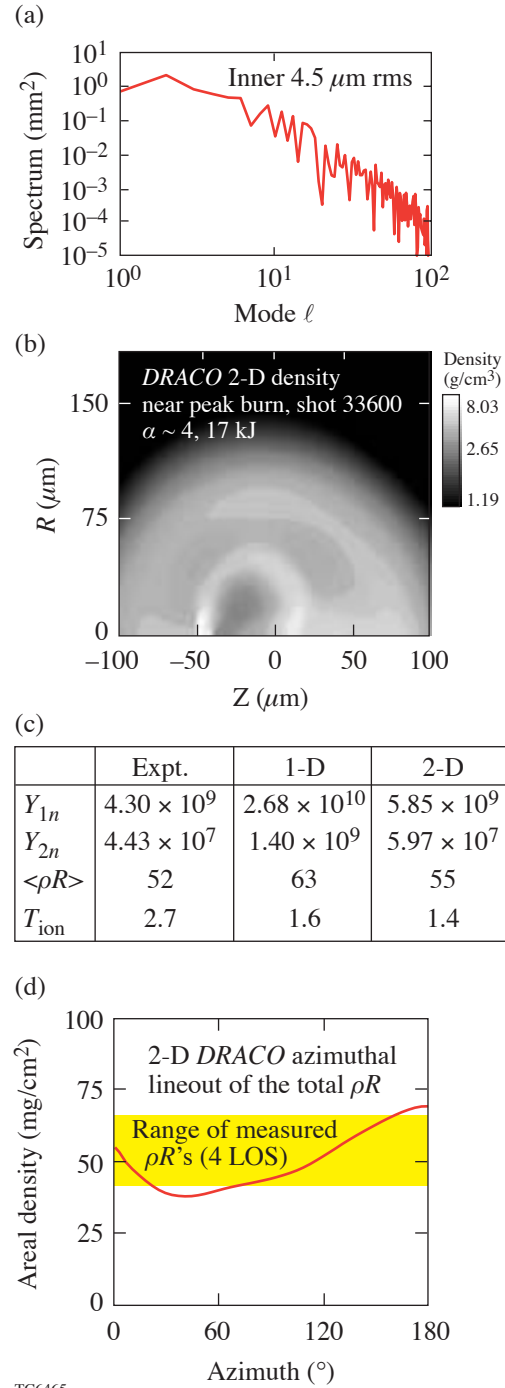


Figure 97.6

Two-dimensional *DRACO* input and results for shot 33600. (a) Input ice roughness spectrum, (b) isodensity contours drawn near the time of peak burn, (c) tabular comparison of secondary-neutron yields and neutron-averaged areal density and ion temperature, and (d) angular variation of the total areal density calculated from the isodensity contours. Yellow region represents the range of experimentally obtained areal-density measurements.

$\alpha = 4$ implosion experiments and placed on the graph in Fig. 97.7. It can be seen that the points are in reasonable agreement with the $\bar{\sigma}$ scaling. When nonuniformities on OMEGA are improved, implosion experiments will approach the $\sim 40\%$ YOQ goal for these implosions as denoted by the dashed lines in Fig. 97.7.

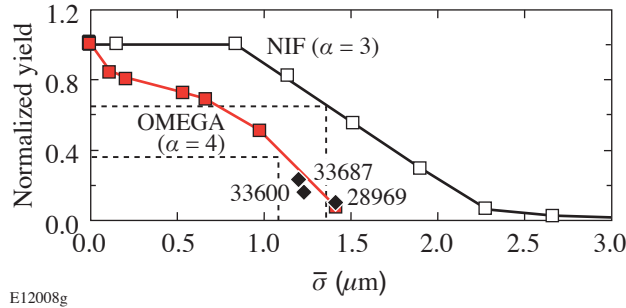


Figure 97.7
Comparison of the $\bar{\sigma}$ stability analysis for the NIF $\alpha = 3$ and the OMEGA $\alpha = 4$ designs. The dashed lines indicate the predicted value of $\bar{\sigma}$ and the corresponding target performance for each of the two designs when all NIF specifications for levels of nonuniformity are applied. The solid diamonds represent results from 2-D *DRACO* simulations of the noted OMEGA experiments.

Re-baseline of the Direct-Drive Point Design

The baseline direct-drive point design has not experienced any significant changes since its introduction by Verdon²⁸ in the early 1990s. The design, consisting of a levitated 340- μm -thick cryogenic DT layer coated with 3 μm of CH and irradiated with 1.8 MJ of 351-nm light, has undergone several design studies^{3,29,30} and has consistently been shown to be robust to moderate levels of perturbation. The design's only weakness, which can be attributed to low ablation velocities, is its strong susceptibility to laser imprint during the acceleration phase of the implosion. The limited ablation velocities cannot effectively stabilize the RT growth of the fast-growing, short-wavelength-laser nonuniformities present in the laser-beam profile. While several schemes have been adopted to smooth these nonuniformities,^{10–12} the maximum ratio of the perturbation amplitude to the in-flight shell thickness has been shown to approach 70% during the acceleration phase of the implosion.³¹

Recently, an old idea of modifying the seeds of RT growth within the ablation region using picket pulses³² has been examined for the point design.³³ Goncharov⁹ modified this process by employing a very narrow Gaussian picket added to the foot of the drive pulse to launch an early, unsupported shock

wave into the target. Because the shock wave is unsupported, it begins to decay after the rarefaction wave from the front surface (created at the end of the picket) catches up to it. As the shock decays, it creates a shaped adiabat within the fuel layer—low near the shock front and high near the ablation region. The high adiabat in the ablation region results in much higher ablation velocities, which, in turn, provide for increased stabilization of the RT growth present there.

The decaying shock technique has recently been applied to several direct-drive, high-gain target designs,^{34–36} including the Verdon point design. In all cases the scheme has been shown to dramatically reduce the deleterious effects of laser imprint. As such, the direct-drive-ignition design has been modified to include a 200-ps laser picket, and an energy-scaled design has been set for implosion experiments on OMEGA. The energy-scaled design serves as the basis of all following calculations.

The $\bar{\sigma}$ stability analysis mentioned previously becomes doubtful in cases of targets with very poor stability characteristics. This is because the analysis assumes a continuous inner ice layer to evaluate. For seriously perturbed implosions, however, the target shell can break apart, failing to provide the continuous interface. Such is the case for the $\alpha = 2$ design without the benefit of a stabilizing picket. The effective $\bar{\sigma}$ value for this design with the current levels of nonuniformities present on OMEGA is greater than 10 μm . As was shown in Ref. 9, the main fuel layer for this implosion was seriously perturbed and on the verge of breakup. Dramatic improvement in layer integrity was achieved, however, when a stabilizing picket was employed. The calculated $\bar{\sigma}$ for the $\alpha = 2$ with picket ($\alpha 2p$) falls close to 1 μm . With the addition of the picket it now becomes possible to evaluate $\alpha 2p$ target performance using the $\bar{\sigma}$ analysis.

Many 2-D *DRACO* simulations were run to evaluate the performance of the $\alpha 2p$ design under the influence of various levels of laser imprint, laser power imbalance, and cryogenic ice roughness. For example, we show two isodensity contours of the $\alpha 2p$ target imploded with a 1- μm inner ice roughness in Fig. 97.8(a). The image shows split contours taken at $t = 2.3$ ns (end of acceleration) and at $t = 2.7$ ns (peak neutron production). Analyzing the inner-ice-roughness spectrum at the first time yields the $\bar{\sigma}$ parameter for this run ($\bar{\sigma} = 0.52$), while the final neutron performance is determined by the core conditions at the second time (YOQ = 77%). A scan of target performance for the $\alpha 2p$ design as a function of ice roughness is shown in Fig. 97.8(b).

Such simulations provide the necessary information to develop the $\bar{\sigma}$ scaling for this design as shown in Fig. 97.9. From this graph it can be seen that the OMEGA $\alpha 2p$ design is almost as stable as the $\alpha = 4$ design. Such results allow for the confident fielding of low-adiabat direct-drive target designs on both OMEGA and the NIF. The design and testing of the laser picket required for the OMEGA $\alpha 2p$ target is already underway at LLE, and experiments should commence in mid-FY04.

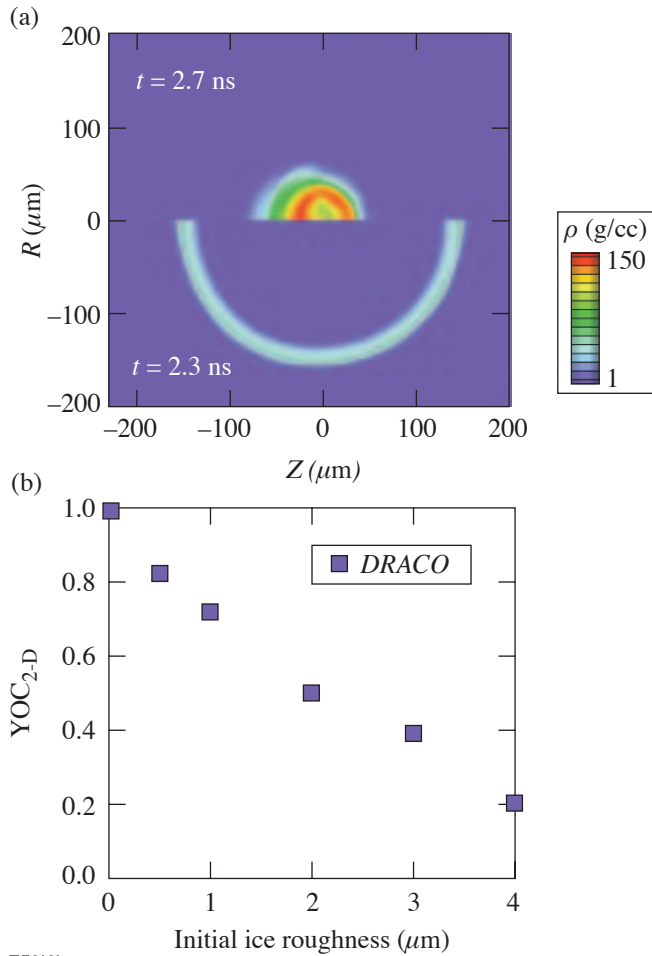


Figure 97.8 Results of a series of DRACO simulations evaluating YOC degradation due to increasing inner ice roughness. (a) Split isodensity contours drawn at $t = 2.3$ ns (end of acceleration phase) and at $t = 2.7$ ns (stagnation); (b) decay of YOC with increasing ice roughness.

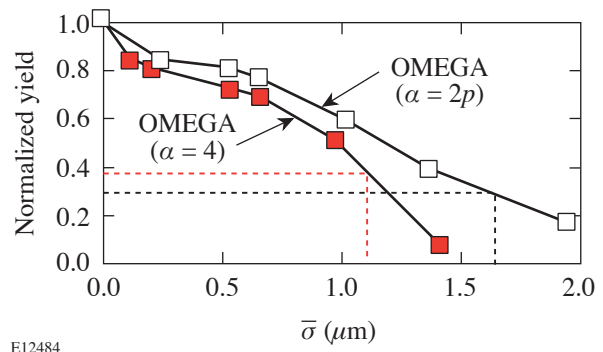


Figure 97.9 Comparison of the $\bar{\sigma}$ stability analysis for the OMEGA $\alpha = 4$ and the OMEGA $\alpha = 2p$ designs. The dashed lines indicate the predicted value of $\bar{\sigma}$ and the corresponding target performance for each of the two designs when all NIF specifications for levels of nonuniformity are applied.

Conclusion

The cryogenic implosion campaign at LLE is a staged program comprised of several concurrent efforts including the experimental validation of target performance for progressively lower fuel-adiabat target designs; the physical minimization of the interfacial cryogenic surface roughness; and ultimately the fielding and imploding of cryogenic DT targets on the OMEGA laser system. Recent advances in all three of these efforts have LLE poised to demonstrate scaled-ignition performance with DT on OMEGA by the end of FY05. In the area of target implosions, significant progress has been made with several series of cryogenic implosion experiments evaluating target performance with high-adiabat solid-D₂ and WF targets and low-adiabat solid-D₂ targets. It has been shown that there is good agreement between the experimental observables and the results of 2-D DRACO simulations for targets imploded near target chamber center. The use of adiabat shaping has led to increased stability for both the “all-DT” and wetted-foam direct-drive NIF point designs and the corresponding ignition-scaled experiments for OMEGA. Dramatic advances in cryogenic layer characterization and layering over the last year have resulted in LLE producing sub-2-μm ice layers in targets for implosion on OMEGA. The cryogenic DT fill and transfer station (FTS) is currently being qualified and will be DT-charged by the end of this fiscal year. With this system in place, full-scale layering studies of cryogenic DT ice will be undertaken, resulting in the fielding of ignition-scale cryogenic DT targets on OMEGA.

ACKNOWLEDGMENT

The authors are extremely grateful to the staff of the Laboratory for Laser Energetics for their tireless dedication to the cryogenic implosion program and the operation of the OMEGA laser system. In particular, the authors would like to acknowledge the efforts of the Cryogenic Target Fabrication Group for the production of layered and characterized capsules on a regular schedule. This work was supported by the U. S. Department of Energy Office of Inertial Confinement Fusion under Cooperative Agreement No. DE-FC03-92SF19460, the University of Rochester, and the New York State Energy Research and Development Authority. The support of the DOE does not constitute an endorsement by the DOE of the views expressed in this article.

REFERENCES

1. T. R. Boehly, D. L. Brown, R. S. Craxton, R. L. Keck, J. P. Knauer, J. H. Kelly, T. J. Kessler, S. A. Kumpan, S. J. Loucks, S. A. Letzring, F. J. Marshall, R. L. McCrory, S. F. B. Morse, W. Seka, J. M. Soures, and C. P. Verdon, *Opt. Commun.* **133**, 495 (1997).
2. W. J. Hogan, E. I. Moses, B. E. Warner, M. S. Sorem, and J. M. Soures, *Nucl. Fusion* **41**, 567 (2001).
3. P. W. McKenty, V. N. Goncharov, R. P. J. Town, S. Skupsky, R. Betti, and R. L. McCrory, *Phys. Plasmas* **8**, 2315 (2001).
4. R. Betti, K. Anderson, V. N. Goncharov, R. L. McCrory, D. D. Meyerhofer, S. Skupsky, and R. P. J. Town, *Phys. Plasmas* **9**, 2277 (2002).
5. W. K. Levedahl and J. D. Lindl, *Nucl. Fusion* **37**, 165 (1997).
6. M. C. Herrmann, M. Tabak, and J. D. Lindl, *Phys. Plasmas* **8**, 2296 (2001).
7. A. Kemp, J. Meyer-ter-Vehn, and S. Atzeni, *Phys. Rev. Lett.* **86**, 3336 (2001).
8. D. Keller, T. J. B. Collins, J. A. Delettrez, P. W. McKenty, P. B. Radha, B. Whitney, and G. A. Moses, *Bull. Am. Phys. Soc.* **44**, 37 (1999).
9. V. N. Goncharov, J. P. Knauer, P. W. McKenty, P. B. Radha, T. C. Sangster, S. Skupsky, R. Betti, R. L. McCrory, and D. D. Meyerhofer, *Phys. Plasmas* **10**, 1906 (2003).
10. T. J. Kessler, Y. Lin, J. J. Armstrong, and B. Velazquez, in *Laser Coherence Control: Technology and Applications*, edited by H. T. Powell and T. J. Kessler (SPIE, Bellingham, WA, 1993), Vol. 1870, pp. 95–104.
11. T. R. Boehly, V. A. Smalyuk, D. D. Meyerhofer, J. P. Knauer, D. K. Bradley, R. S. Craxton, M. J. Guardalben, S. Skupsky, and T. J. Kessler, *J. Appl. Phys.* **85**, 3444 (1999).
12. S. Skupsky, R. W. Short, T. Kessler, R. S. Craxton, S. Letzring, and J. M. Soures, *J. Appl. Phys.* **66**, 3456 (1989).
13. F. J. Marshall, J. A. Delettrez, R. Epstein, R. Forties, R. L. Keck, J. H. Kelly, P. W. McKenty, S. P. Regan, and L. J. Waxer, *Phys. Plasmas* **11**, 251 (2004).
14. J. Koch, Lawrence Livermore National Laboratory, private communication (2000).
15. S. Jin, *2002 Summer Research Program for High School Juniors at the University of Rochester's Laboratory for Laser Energetics*, Laboratory for Laser Energetics Report No. 329, NTIS document No. DOE/SF/19460-479 (2003). Copies may be obtained from the National Technical Information Service, Springfield, VA 22161.
16. R. Stephens, General Atomics, private communication (2003).
17. T. C. Sangster, J. A. Delettrez, R. Epstein, V. Yu. Glebov, V. N. Goncharov, D. R. Harding, J. P. Knauer, R. L. Keck, J. D.ilkenny, S. J. Loucks, L. D. Lund, R. L. McCrory, P. W. McKenty, F. J. Marshall, D. D. Meyerhofer, S. F. B. Morse, S. P. Regan, P. B. Radha, S. Roberts, W. Seka, S. Skupsky, V. A. Smalyuk, C. Sorce, J. M. Soures, C. Stoeckl, K. Thorp, J. A. Frenje, C. K. Li, R. D. Petrasso, F. H. Séguin, K. A. Fletcher, S. P. Padalino, C. Freeman, N. Izumi, J. A. Koch, R. A. Lerche, M. J. Moran, T. W. Phillips, and G. J. Schmid, *Phys. Plasmas* **10**, 1937 (2003).
18. V. Yu. Glebov, D. D. Meyerhofer, C. Stoeckl, and J. D. Zuegel, *Rev. Sci. Instrum.* **72**, 824 (2001).
19. F. H. Séguin, C. K. Li, D. G. Hicks, J. A. Frenje, K. M. Green, R. D. Petrasso, J. M. Soures, D. D. Meyerhofer, V. Yu. Glebov, C. Stoeckl, P. B. Radha, S. Roberts, C. Sorce, T. C. Sangster, M. D. Cable, S. P. Padalino, and K. Fletcher, *Phys. Plasmas* **9**, 2725 (2002).
20. T. J. Murphy, R. E. Chrien, and K. A. Klare, *Rev. Sci. Instrum.* **68**, 610 (1997).
21. C. K. Li, F. H. Séguin, D. G. Hicks, J. A. Frenje, K. M. Green, S. Kurebayashi, R. D. Petrasso, D. D. Meyerhofer, J. M. Soures, V. Yu. Glebov, R. L. Keck, P. B. Radha, S. Roberts, W. Seka, S. Skupsky, C. Stoeckl, and T. C. Sangster, *Phys. Plasmas* **8**, 4902 (2001).
22. C. Stoeckl, V. Yu. Glebov, S. Roberts, T. C. Sangster, R. A. Lerche, R. L. Griffith, and C. Sorce, *Rev. Sci. Instrum.* **74**, 1713 (2003).
23. R. D. Petrasso, J. A. Frenje, C. K. Li, F. H. Séguin, J. R. Rygg, B. E. Schwartz, S. Kurebayashi, P. B. Radha, C. Stoeckl, J. M. Soures, J. Delettrez, V. Yu. Glebov, D. D. Meyerhofer, and T. C. Sangster, *Phys. Rev. Lett.* **90**, 095002 (2003).
24. M. C. Richardson, P. W. McKenty, F. J. Marshall, C. P. Verdon, J. M. Soures, R. L. McCrory, O. Barnouin, R. S. Craxton, J. Delettrez, R. L. Hutchison, P. A. Jaanimagi, R. Keck, T. Kessler, H. Kim, S. A. Letzring, D. M. Roback, W. Seka, S. Skupsky, B. Yaakobi, S. M. Lane, and S. Prussin, in *Laser Interaction and Related Plasma Phenomena*, edited by H. Hora and G. H. Miley (Plenum Publishing, New York, 1986), Vol. 7, pp. 421–448.
25. G. Hazak *et al.*, *Phys. Plasmas* **5**, 4357 (1998).
26. A. D. Kotelnikov and D. C. Montgomery, *Phys. Fluids* **10**, 2037 (1998).
27. A. Frank, Department of Physics and Astronomy, University of Rochester, private communication (2003).

28. C. P. Verdon, *Bull. Am. Phys. Soc.* **38**, 2010 (1993).
29. S. V. Weber *et al.*, *ICF Quarterly Report* **7**, 43, Lawrence Livermore National Laboratory, Livermore, CA, UCRL-LR-105821-97-2 (1997).
30. Laboratory for Laser Energetics LLE Review **79**, 121, NTIS document No. DOE/SF/19460-317 (1999). Copies may be obtained from the National Technical Information Service, Springfield, VA 22161.
31. V. N. Goncharov, P. McKenty, S. Skupsky, R. Betti, R. L. McCrory, and C. Cherfils-Clérouin, *Phys. Plasmas* **7**, 5118 (2000).
32. M. Tabak, *ICF Program Annual Report 1989(U)*, Lawrence Livermore National Laboratory, Livermore, CA, UCRL-LR-116901-88/80, 141 (1989) (unpublished).
33. T. J. B. Collins and S. Skupsky, *Phys. Plasmas* **9**, 275 (2002).
34. T. J. B. Collins, Laboratory for Laser Energetics, private communication (2003).
35. J. Perkins, Lawrence Livermore National Laboratory, private communication (2003).
36. A. J. Schmitt *et al.*, "Large-Scale, High-Resolution Simulations of High-Gain, Direct-Drive ICF Targets," to be published in *Physics of Plasmas*.

Hot-Core Characterization of a Cryogenic D₂ Target at Peak Neutron Production in a Direct-Drive Spherical Implosion

In inertial confinement fusion¹ (ICF), a spherical shell is irradiated either directly by a large number of overlapping laser beams (direct drive) or by x rays produced in a high-Z “hohlraum” (indirect drive).² During the laser-driven acceleration phase of an implosion, the target compresses while it converges to the center, then decelerates to peak compression as the core of the target is heated to high temperatures, causing a thermonuclear burn within its fuel. The current goal of ICF research is to achieve ignition and a positive gain, where the amount of energy released through thermonuclear fusion is equal to or higher than the amount of laser energy used to drive the target. The combination of high temperature and areal density (ρR) in the compressed fuel is necessary to ignite the target.² This goal is expected to be achieved on the National Ignition Facility (NIF),² currently under construction at Lawrence Livermore National Laboratory. In the direct-drive ignition target design³ for the NIF, a 3.4-mm-diam, 350- μm -thick cryogenic deuterium–tritium (DT) shell is imploded by 192 overlapped laser beams with a total energy of 1.5 MJ. The fusion energy will be released through the nuclear reaction $\text{D} + \text{T} \rightarrow {}^4\text{He}$ (3.5 MeV) + n (14.1 MeV). An expected neutron yield of 2.5×10^{19} (corresponding to a gain of ~ 45) will be achieved at a fuel temperature of ~ 30 keV and an areal density of ~ 1200 mg/cm² at peak compression.

While cryogenic DT targets^{4,5} will be used for fusion energy production, the current implosion program on the 60-beam, 351-nm OMEGA laser system⁶ uses cryogenic D₂ targets to study the relevant implosion physics. The D₂ targets are hydrodynamically equivalent to DT targets, but much simpler to produce and more useful for diagnosing target conditions near peak compression. The primary fusion reaction in D₂ fuel has two branches: (a) $\text{D} + \text{D} \rightarrow {}^3\text{He}$ (0.82 MeV) + n (2.45 MeV), and (b) $\text{D} + \text{D} \rightarrow \text{T}$ (1.01 MeV) + p (3.02 MeV). The primary reaction product T reacts with D through the secondary reaction $\text{D} + \text{T}$ (0 to 1.01 MeV) \rightarrow ${}^4\text{He}$ + n (11.9 to 17.2 MeV). Experiments with plastic targets estimated target compression by using the size of the core emission and the ratio of secondary DT to primary DD neutron yields. This technique was first used by Azechi *et al.*⁷ and by Cable and

Hatchett.⁸ In their calculations, the core ρR was inferred from the ratios of secondary to primary yields, assuming the core had uniform temperature and density. For ICF to succeed, it is necessary to infer core temperature–density profiles and directly compare them with hydrocode simulations. Because the target ignition designs are based on hydrocode predictions, they should be benchmarked by the most-comprehensive set of measurements.

Recently Radha *et al.* modeled⁹ core temperature–density profiles at peak neutron production in plastic-shell targets. About ten different experimental observations with several different types of targets (having various dopants in a gas fuel and plastic shell) were necessary for a comprehensive characterization of the core conditions.⁹ Kurebayashi *et al.*¹⁰ studied the usefulness of secondary particles (neutrons and protons) for hot-core modeling of plastic and cryogenic capsules. The cryogenic D₂ targets cannot have dopants, but because they are much simpler (there is no complication of mixing of different materials in the core), it is possible to characterize them (with the same level of detail as plastic shells) with fewer experimental observables. This article describes experiments where measured primary DD and secondary DT neutron yields, neutron-averaged ion temperatures, and x-ray images at peak neutron production are used to infer the electron-pressure and temperature–density profiles in cryogenic D₂ implosions for the first time. The areal densities of neutron production and “triton-stopping” regions are introduced here to characterize target compression. These quantities are the compression measurements that are extended from the ρR inferred from the ratios of secondary to primary yields. Because they are derived from the temperature–density profiles consistent with experimental measurements, they provide more-accurate measurements of compression.

The experiments were direct-drive implosions of ~ 920 - μm -initial-diam targets with shells that consisted of ~ 100 - μm -thick inner D₂-ice layers and outer 5- μm -thick plastic CD layers.¹¹ The targets were imploded with a 1-ns square pulse shape with a total on-target energy of ~ 23 kJ on OMEGA.⁶

The laser beams were smoothed with distributed phase plates,¹² 1-THz two-dimensional smoothing by spectral dispersion,¹³ and polarization smoothing¹⁴ using birefringent wedges. The measured experimental yield ratios relative to the predicted yields using 1-D simulations were typically $\sim 30\%$ in a large number of similar implosions. In one implosion, the experimental yield was closer to the predicted yield (59%); therefore, this implosion was used for the analysis presented here. The measured primary DD and secondary DT neutron yields for this implosion were $Y_1 = 1.24 \times 10^{11} \pm 8 \times 10^8$ and $Y_2 = 1.17 \times 10^9 \pm 3 \times 10^7$, respectively.¹⁰ The measured neutron-averaged ion temperature was $T_i = 3.6 \pm 0.5$ keV and the neutron burn width was $\tau = 170 \pm 25$ ps.¹¹ The core images¹¹ were measured with an x-ray framing camera with a spatial resolution of ~ 10 μm , a temporal resolution of ~ 40 ps, and a 200- μm -thick beryllium filter (which transmitted x rays with energies of more than ~ 2 keV).

The target core at peak neutron production was characterized by choosing temperature [$T(\mathbf{r})$] and density [$n(\mathbf{r})$] profiles that produced the same primary and secondary neutron yields, the neutron-averaged ion temperature, and the size of x-ray images as measured within experimental uncertainties.⁹ In the first stage of modeling, only those temperature–density profiles that were consistent with the primary DD neutron yield and neutron-averaged ion temperature were selected from all possible combinations at a particular electron pressure (the hot core was assumed to be isobaric). In the second stage, profiles consistent with the secondary DT neutron yield were chosen from those selected in the first stage. Similarly, the temperature–density profiles consistent with all neutron measurements were chosen at each electron pressure in the range of 1 to 10 Gbar. Finally, only those temperature–density profiles that were consistent with the size of the x-ray core images were chosen to characterize the hot core at peak neutron production. The following assumptions were used in the core modeling: (1) the core plasma was a fully ionized ideal gas; (2) the core was isobaric [$P_e(\mathbf{r}) = \text{const}$] at stagnation; (3) the temperature–density profiles were spherically symmetric; (4) the electron and ion temperatures as well as the densities were equal;⁹ (5) the core was static during the time of neutron production τ (therefore, the inferred pressure and temperature–density profiles were considered to be neutron averaged); and (6) the temperature decreased monotonically from the center. These secondary DT neutron yields used Li and Petrasso’s plasma stopping powers¹⁵ to calculate the triton’s energy loss as it propagated through a 3-D core. The x-ray images were constructed using radiation-transport calculations in a fully ionized deuterium plasma with free-free emission and absorption.¹⁶

Figure 97.10(a) shows one of the grids used to construct temperature profiles. The temperature step was 250 eV, and the distance step was 20 μm (distance steps of 15, 10, and 5 μm were used in additional, more-detailed grids). The curves show examples of two (out of nearly $\sim 10^{10}$) temperature profiles $T(\mathbf{r})$ used in the modeling. The corresponding density profiles $n(\mathbf{r})$ were calculated using $P_e(\mathbf{r}) = n(\mathbf{r}) \times T(\mathbf{r})$. The range of temperatures that satisfy the measured DD neutron yield and neutron-averaged ion temperature (calculated in the first stage of modeling) is shown by the lightly shaded region in Fig. 97.10(b) at an electron pressure of 2.6 Gbar. The results of the second stage of modeling—the temperature profiles consistent with secondary DT neutron yield (in addition to primary DD yield and neutron-averaged ion temperature)—are shown by the darkly shaded region. Similar calculations were conducted for electron pressures in the range from 1 to 10 Gbar. As an example, the ranges of temperature profiles consistent with all neutron measurements for three different electron pressures (1.3, 2.6, and 5.2 Gbar) are shown in Fig. 97.11(a). It was found that for any electron pressure above 1.3 Gbar, temperature–density profiles consistent with all neutron measurements exist; therefore, neutron measurements by themselves are not sufficient to accurately characterize the target core at peak neutron production. The profiles at different pressures, however, would make different sizes of x-ray emission, as can be seen from the profiles shown in Fig. 97.11(b). Therefore, for various temperature–density profiles, the x-ray images were constructed and compared with the one measured at peak neutron production. In these calculations, the transmis-

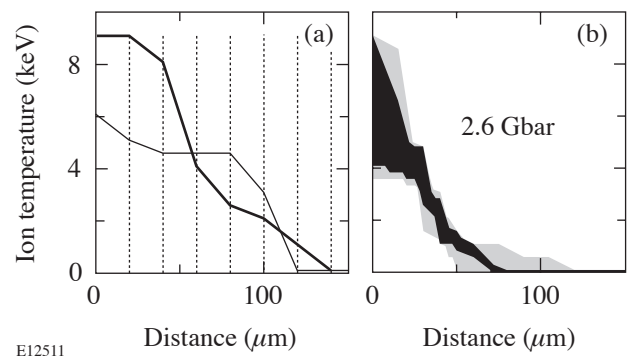
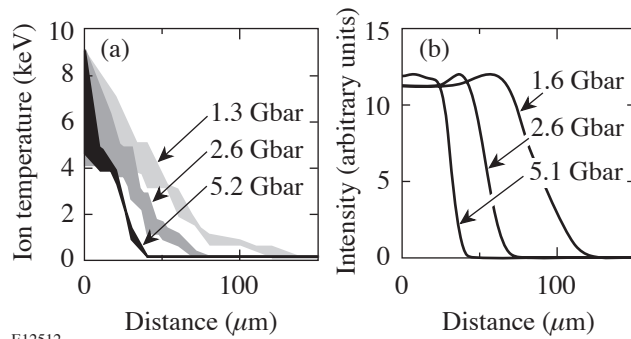


Figure 97.10

(a) The temperature–radius grid. The temperature step is 250 eV, and the distance step is 20 μm , as shown by the vertical dotted lines. The thick and thin solid lines show examples of monotonically decreasing temperature profiles as a function of distance used in core modeling. (b) The range of ion-temperature profiles consistent with the measured primary DD yield and neutron-averaged ion temperature (lightly shaded area), and in addition, the secondary DT yield (darkly shaded area), at electron pressure of 2.6 Gbar.

sion of the Be filter and the x-ray spectral response of the framing camera's gold photocathode were taken into account. The size of the x-ray image is very sensitive to the core pressure [see Fig. 97.11(b)]. The measured core image at peak neutron production is shown in Fig. 97.12(a). Figure 97.12(a) also shows two central lineouts of the measured image in horizontal and vertical directions by thick and thin solid lines. The image is slightly elliptical with FWHM's (full width at half maximum) ranging from about 94 to 100 μm in two perpendicular directions. The measured image is consistent with calculated images in the electron-pressure range from 2.3 to 3.1 Gbar. The shaded area in Fig. 97.12(a) is between the 2.3- and 3.1-Gbar



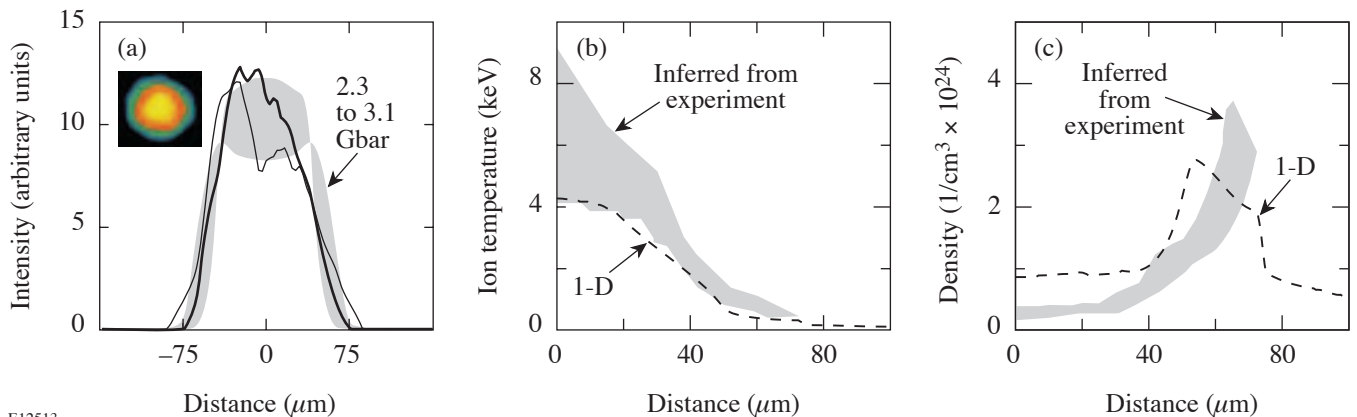
E12512

Figure 97.11

(a) The range of temperature profiles that satisfy measured primary DD, secondary DT yields, and neutron-averaged ion temperature, calculated for electron pressures of 1.6 (light), 2.6 (medium), and 5.1 Gbar (darkly shaded area). (b) Examples of x-ray radial lineouts (normalized to their highest values) calculated for the same pressures of 1.6, 2.6, and 5.1 Gbar.

lineouts, and the measured lineouts lie within this area. The ranges of inferred core temperature and density profiles, corresponding to this range of electron pressures, are shown in Figs. 97.12(b) and 97.12(c), respectively. As a result, only a relatively narrow range of temperature–density profiles is consistent with all neutron and x-ray measurements, simultaneously. The dashed curves correspond to simulations using the 1-D hydrocode *LILAC*,¹¹ which are discussed below.

Even though temperature–density profiles contain all information about the core condition, the core ρR has always been a simple and useful measurement^{7,8} of target performance in ICF. Modeling based on flat temperature–density profiles^{7,8} allows only approximate estimates of the areal density. Detailed temperature–density profiles consistent with all neutron and x-ray measurements are required for accurate determination of the core ρR . The solid line in Fig. 97.13(a) shows a cumulative DD neutron yield as a function of the core areal density, calculated using temperature–density profiles at an electron pressure of 2.6 Gbar. The ρR of the “burn” region of $\sim 10 \text{ mg}/\text{cm}^2$ was defined at 95% of the maximum value of the cumulative yield. The burn region ρR inferred from the temperature–density profiles at 1.3 Gbar [see Fig. 97.11(a)] is a factor of 2 smaller. Even though the 1.3-Gbar profiles are consistent with all neutron measurements, they were rejected because they did not predict the measured x-ray images. This means that the core ρR inferred solely from the yield ratio of primary to secondary neutrons (especially using flat profiles that are not consistent with all measurements) could be very

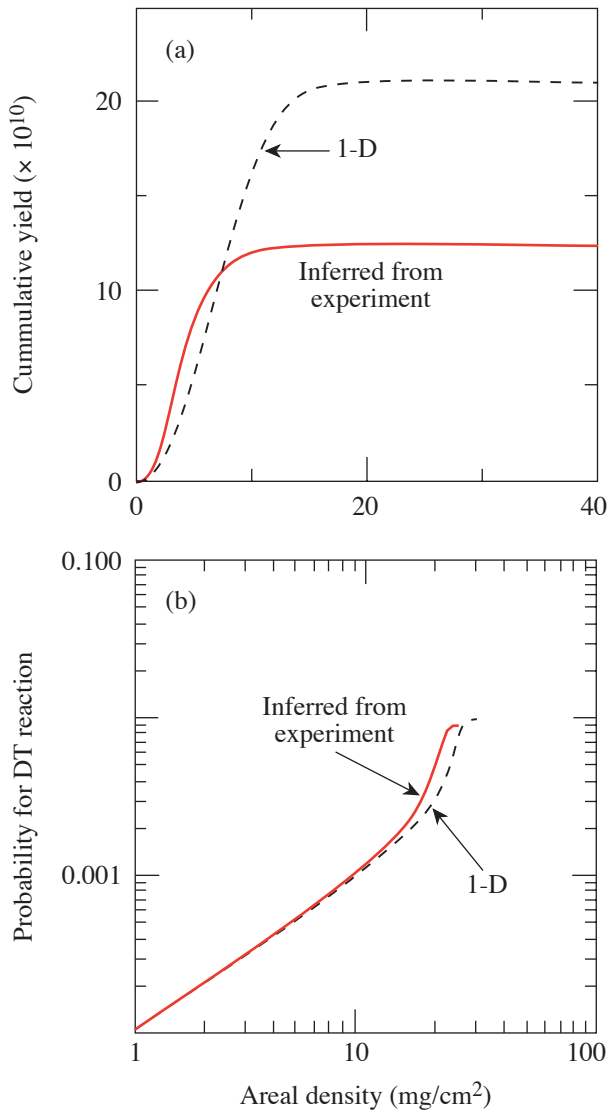


E12513

Figure 97.12

(a) X-ray framing camera image of the core at peak neutron production (upper left side); the horizontal and vertical lineouts of this image (thick and thin lines). The shaded area lies in between the lineouts of calculated images at electron pressures of 2.3 and 3.1 Gbar. All lineouts are normalized to the integrated intensities under the curves. The range of (b) core temperature and (c) density profiles corresponding to electron pressures in the range from 2.3 to 3.1 Gbar, which produce sizes of x-ray emission consistent with that of the measured x-ray image (shown by gray areas). The 1-D *LILAC* predictions are shown by dashed lines.

inaccurate. The total target ρR was measured to be $\sim 61 \text{ mg/cm}^2$ at peak neutron production using a downshift in the secondary proton spectra.¹⁰



E12430

Figure 97.13

(a) Cumulative yields as a function of core ρR , inferred from the experiment, for an electron pressure of 2.6 Gbar (solid curve), and from a 1-D simulation (dashed curve). The ρR 's of the "burn" regions (~ 10 and $\sim 15 \text{ mg/cm}^2$, respectively) were defined at 95% of the maximum value of the cumulative yield. (b) Probability for a secondary DT reaction (equal to a ratio of DT to DD yields) as a function of core ρR , calculated for an electron pressure of 2.6 Gbar (solid curve). The triton probes a core ρR of $\sim 23 \text{ mg/cm}^2$ before being stopped in the core. The dashed curve corresponds to a 1-D simulation with a "triton-stopping" ρR of $\sim 27 \text{ mg/cm}^2$.

The ρR of a "triton-stopping" region is another useful parameter describing the extent of the hot core that is probed by the neutron measurements. The tritons are born in the neutron-production region through the DD fusion reaction. They are slowed down while they move through the core¹⁵ until they are stopped in the target. The triton-slowing rate depends strongly on plasma temperature and density: it is higher in colder, less-dense plasmas;^{7,8} therefore the ρR of a triton-stopping region (or the ρR necessary to stop the triton) is higher in hotter, denser cores. As the triton propagates in the core, it can react with deuterium through a secondary DT reaction, producing a secondary DT neutron.^{7,8} Figure 97.13(b) shows (by a solid line) the probability for the DT reaction as a function of the core areal density, calculated for the same conditions as in Fig. 97.13(a) at an electron pressure of 2.6 Gbar. In this calculation, the triton is born at the core center and propagates toward the outer surface until it is stopped after probing $\sim 23 \text{ mg/cm}^2$ of the core plasma. The probability for the DT reaction dramatically increases right before the triton is stopped because the DT-reaction cross section increases as the triton slows down in the plasma. Therefore, the secondary DT neutron yield is very sensitive to the temperature–density conditions in the outer part of the hot core, while the primary DD yield is more sensitive to conditions in the central part of the core.

The modeling results were compared with the predictions¹¹ of a 1-D *LILAC* simulation (dashed lines in Figs. 97.12 and 97.13). The predicted DD neutron yield of 2.1×10^{11} was close to the measured yield of 1.24×10^{11} , while the simulated neutron-averaged ion temperature of 3.1 keV was a little lower than that measured 3.6 keV. As a result, the simulated temperature profile [see Fig. 97.12(b)] was a little lower than the temperature range inferred from the experiment, while the density profile was a little higher [see Fig. 97.12(c)]. In the 1-D simulation, the burn and triton-stopping region ρR 's were very close to those inferred from the experiment. In the simulation, the burn ρR was $\sim 15 \text{ mg/cm}^2$ ($\sim 10 \text{ mg/cm}^2$ in the experiment) and the triton-stopping region ρR was $\sim 27 \text{ mg/cm}^2$ ($\sim 23 \text{ mg/cm}^2$ in the experiment), as shown in Fig. 97.13. Measurements based on monochromatic differential imaging^{17,18} of core x rays are planned to infer the time-resolved evolution of D_2 -core profiles in the near future, using techniques similar to those described elsewhere.¹⁹

In conclusion, the compressed-core, electron temperature–density profiles of a cryogenic deuterium (D_2) target have been characterized using measured primary DD and secondary DT yields, neutron-averaged ion temperature, and core x-ray im-

ages at peak neutron production. The inferred temperature–density profiles are in good agreement with predictions of the 1-D hydrocode *LILAC*. The electron pressure, burn, and triton-stopping region ρR 's were inferred to be 2.7 ± 0.4 Gbar, ~ 10 mg/cm², and ~ 23 mg/cm², respectively.

ACKNOWLEDGMENT

One of the authors (V.A.S.) would like to thank D. C. Wilson for helpful discussions. This work was supported by the U.S. Department of Energy Office of Inertial Confinement Fusion under Cooperative Agreement No. DE-FC03-92SF19460, the University of Rochester, and the New York State Energy Research and Development Authority. The support of DOE does not constitute an endorsement by DOE of the views expressed in this article.

REFERENCES

1. J. Nuckolls *et al.*, *Nature* **239**, 139 (1972).
2. J. D. Lindl, *Phys. Plasmas* **2**, 3933 (1995).
3. P. W. McKenty, V. N. Goncharov, R. P. J. Town, S. Skupsky, R. Betti, and R. L. McCrory, *Phys. Plasmas* **8**, 2315 (2001).
4. R. L. McCrory, J. M. Soures, C. P. Verdon, F. J. Marshall, S. A. Letzring, S. Skupsky, T. J. Kessler, R. L. Kremens, J. P. Knauer, H. Kim, J. Delettrez, R. L. Keck, and D. K. Bradley, *Nature* **335**, 225 (1988).
5. Y. Kitagawa *et al.*, *Phys. Rev. Lett.* **75**, 3130 (1995).
6. T. R. Boehly, D. L. Brown, R. S. Craxton, R. L. Keck, J. P. Knauer, J. H. Kelly, T. J. Kessler, S. A. Kumpan, S. J. Loucks, S. A. Letzring, F. J. Marshall, R. L. McCrory, S. F. B. Morse, W. Seka, J. M. Soures, and C. P. Verdon, *Opt. Commun.* **133**, 495 (1997).
7. H. Azechi *et al.*, *Appl. Phys. Lett.* **49**, 555 (1986).
8. M. D. Cable and S. P. Hatchett, *J. Appl. Phys.* **62**, 2233 (1987).
9. P. B. Radha, J. Delettrez, R. Epstein, V. Yu. Glebov, R. Keck, R. L. McCrory, P. McKenty, D. D. Meyerhofer, F. Marshall, S. P. Regan, S. Roberts, T. C. Sangster, W. Seka, S. Skupsky, V. Smalyuk, C. Sorce, C. Stoeckl, J. Soures, R. P. J. Town, B. Yaakobi, J. Frenje, C. K. Li, R. Petrasso, F. Séguin, K. Fletcher, S. Padalino, C. Freeman, N. Izumi, R. Lerche, and T. W. Phillips, *Phys. Plasmas* **9**, 2208 (2002).
10. S. Kurebayashi, J. A. Frenje, F. H. Séguin, J. R. Rygg, C. K. Li, R. D. Petrasso, V. Yu. Glebov, J. A. Delettrez, T. C. Sangster, D. D. Meyerhofer, C. Stoeckl, J. M. Soures, P. A. Amendt, S. P. Hatchett, and R. E. Turner, "Use of Secondary Nuclear Particles for Studying the Areal Density of D₂-Filled Inertial Confinement Fusion Capsules," to be published in *Physics of Plasmas*.
11. T. C. Sangster, J. A. Delettrez, R. Epstein, V. Yu. Glebov, V. N. Goncharov, D. R. Harding, J. P. Knauer, R. L. Keck, J. D. Kilkenny, S. J. Loucks, L. D. Lund, R. L. McCrory, P. W. McKenty, F. J. Marshall, D. D. Meyerhofer, S. F. B. Morse, S. P. Regan, P. B. Radha, S. Roberts, W. Seka, S. Skupsky, V. A. Smalyuk, C. Sorce, J. M. Soures, C. Stoeckl, K. Thorp, J. A. Frenje, C. K. Li, R. D. Petrasso, F. H. Séguin, K. A. Fletcher, S. Padalino, C. Freeman, N. Izumi, J. A. Koch, R. A. Lerche, M. J. Moran, T. W. Phillips, and G. J. Schmid, *Phys. Plasmas* **10**, 1937 (2003).
12. Y. Lin, T. J. Kessler, and G. N. Lawrence, *Opt. Lett.* **20**, 764 (1995).
13. S. P. Regan, J. A. Marozas, J. H. Kelly, T. R. Boehly, W. R. Donaldson, P. A. Jaanimagi, R. L. Keck, T. J. Kessler, D. D. Meyerhofer, W. Seka, S. Skupsky, and V. A. Smalyuk, *J. Opt. Soc. Am. B* **17**, 1483 (2000).
14. T. R. Boehly, V. A. Smalyuk, D. D. Meyerhofer, J. P. Knauer, D. K. Bradley, R. S. Craxton, M. J. Guardalben, S. Skupsky, and T. J. Kessler, *J. Appl. Phys.* **85**, 3444 (1999).
15. C. Li and R. D. Petrasso, *Phys. Plasmas* **2**, 2460 (1995).
16. W. J. Karzas and R. Latter, *Astrophys. J. Suppl. Ser.* **6**, 167 (1961).
17. J. A. Koch, S. W. Haan, and R. C. Mancini, "Multispectral Imaging of Continuum Emission for Determination of Temperature and Density Profiles Inside Implosion Plasmas," to be published in the *Journal of Quantitative Spectroscopy and Radiative Transfer*.
18. V. A. Smalyuk, V. N. Goncharov, J. A. Delettrez, F. J. Marshall, D. D. Meyerhofer, S. P. Regan, and B. Yaakobi, *Phys. Rev. Lett.* **87**, 155002 (2001).
19. I. Golovkin, R. Mancini, S. Louis, Y. Ochi, K. Fujita, H. Nishimura, H. Shirga, N. Miyanaga, H. Azechi, R. Butzbach, I. Uschmann, E. Förster, J. Delettrez, J. Koch, R. W. Lee, and L. Klein, *Phys. Rev. Lett.* **88**, 045002 (2002).

Extended X-Ray Absorption Fine Structure Measurements of Laser Shocks in Ti and V and Phase Transformation in Ti

Introduction

Recently, x-ray diffraction has been used to study dynamic material response to shocks of high pressure (~ 0.1 to 1 Mbar) and high strain rate ($\sim 10^7$ to 10^8 s $^{-1}$).¹⁻³ The goal of this work is to demonstrate the use of extended x-ray absorption fine structure (EXAFS)⁴ as a complementary characterization of such laser-shocked metals. EXAFS is the modulation in the x-ray absorption above the *K* edge (or *L* edge) due to the interference of the photoelectron wave packet with the waves reflected from neighboring atoms. Unlike synchrotron experiments where the imposed temperature is known independently and the main emphasis is on the study of the chemical structure, in this experiment the emphasis is on the measurement of the compression and temperature of the shocked material through the EXAFS spectrum itself. The frequency of EXAFS modulations is related to the interparticle distance, hence to the compression. The damping rate of the modulation can yield the lattice temperature, *which is not available by other methods*. The assumption of three-dimensional compression, required to relate the EXAFS-determined inter-atomic distance to the density, was verified by comparison with measurements of the shock speed, which yield the compression (through the known Hugoniot equation of state).

EXAFS measurements were performed on vanadium and titanium shocked to ~ 0.5 Mbar with a 3-ns laser pulse. The radiation source for the EXAFS measurement was obtained by imploding a spherical target using the 60-beam OMEGA laser.⁵ For vanadium (where no phase transformation exists below ~ 1 Mbar) the measurements demonstrate that EXAFS is a useful method for measuring the compression and temperature of sub-Mbar shocks. For Ti, where an α -Ti to ω -Ti crystal phase transformation is known to occur around ~ 0.1 Mbar, over longer time scales (μ s) behind a steady shock,^{6,7} the measurements show that EXAFS can be used to study such transformations over subnanosecond time scales.

In a previous paper⁸ we showed that a CH shell imploded by a multibeam laser system constitutes a ~ 120 -ps source of intense and relatively smooth spectrum of x-ray radiation,

suitable for EXAFS measurements. Using the 60-beam OMEGA laser, the measured room-temperature Ti EXAFS spectrum agreed with synchrotron results under similar conditions.

The subject of laser-shocked metals can be viewed from two complementary points of view: as a problem in solid-state physics and/or as a problem in plasma physics. The EXAFS measurements in this experiment, and particularly the diffraction measurements¹⁻³ of similar laser shocks, indicate that laser-shocked metals for pressures under ~ 1 Mbar largely retain their crystal-order properties. This is why the crystal phase transformation in Ti could be demonstrated with laser-driven shock waves. The shock dynamics have been simulated with a plasma-physics hydrodynamic code (see **Hydrodynamic Simulations**). The laser-deposition region where the shock is generated is certainly a plasma region and can be simulated only with a plasma-physics code. However, the same code is used to simulate both shock generation and propagation through the sample, thus relating the incident laser intensity to the resulting shock strength. The hydrodynamic code can well simulate the compressed solid because the semi-empirical equation of state⁹ is normalized to known experimental properties of the metal (such as specific heat, Grüneisen parameter, and bulk modulus). The comparison of the code and experimental results forms the basis for the study of the compressed solid, which apart from its crystalline order is also a high-density or strongly coupled plasma. Such plasmas are of great interest in understanding the interior of planets and the behavior of matter under extreme conditions.

Experimental

Figure 97.14 shows a schematic view of the target used to measure EXAFS spectra in laser-shocked targets. Of the 60 OMEGA laser beams, 57 beams of ~ 21 -kJ total energy are focused on an empty CH shell whose implosion generates the radiation source for measuring the absorption spectrum in V or Ti. In previous laser-based EXAFS experiments^{10,11} a planar high-Z target was used where the spectrum was dominated by spectral-line emission and was thus not smooth. The low-Z imploding target used here produces a very intense and smooth

continuum spectrum,⁸ appropriate for absorption measurements. The three remaining OMEGA beams are stacked and used to launch a planar shock wave in the metal target. The laser pulse shape was 1 ns square (each of energy ~50 J); thus the three-stacked beams formed a 3-ns-long square pulse. These beams were focused onto the planar target in a 3.8-mm-diam focal spot, giving an irradiance of 0.4 to 0.5 TW/cm². The delay time of the three-stacked beams with respect to the remainder of the beams was adjusted so that peak implosion (and emission) of the spherical target occurred when the shock wave had just exited the metal layer. The spherical target had a diameter ~950 μm and a CH wall thickness ~20 μm. The planar target consisted of 10-μm-thick polycrystalline V or Ti, coated on both sides with a 17-μm-thick CH layer. The purpose of the front CH layer was to prevent laser heating and ablation of the metal. The purpose of the back CH layer was to prevent shock unloading at the back metal surface. The heat shield (0.5-mm-thick CH foil) minimizes the heating of the metal layer due to soft radiation from the imploding spherical target.

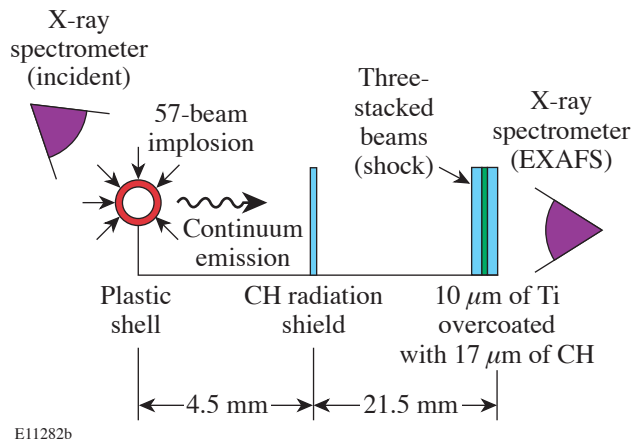


Figure 97.14 Schematic view of the experimental configuration. The imploding spherical target serves as a radiation source for EXAFS measurements. The three-stacked beams launch a shock through the Ti (or V) layer.

Two cross-calibrated x-ray spectrometers measured the spectrum on calibrated film. One spectrometer measured the EXAFS spectrum, the other the incident spectrum. The spectra were measured simultaneously on a single target shot. A typical record of the transmitted spectrum showing EXAFS modulation is shown in Fig. 97.15. As explained in Ref. 8, the high incident intensity enabled us to choose a relatively thick sample (giving an optical depth of 3.5 just above the Ti *K*

edge), which yields high relative modulation amplitude in the measured spectrum. However, the spectrum below the *K* edge is then saturated; to accurately determine the *K*-edge position and below-the-edge signal intensity, we used an Al attenuator on part of the entrance slit, as seen in Fig. 97.15. A typical incident spectrum is shown in Fig. 2(a) of Ref. 8. The spectral resolution of the spectrometer, limited by the source size, was ~5 eV, much smaller than a typical EXAFS modulation period (~60 eV).

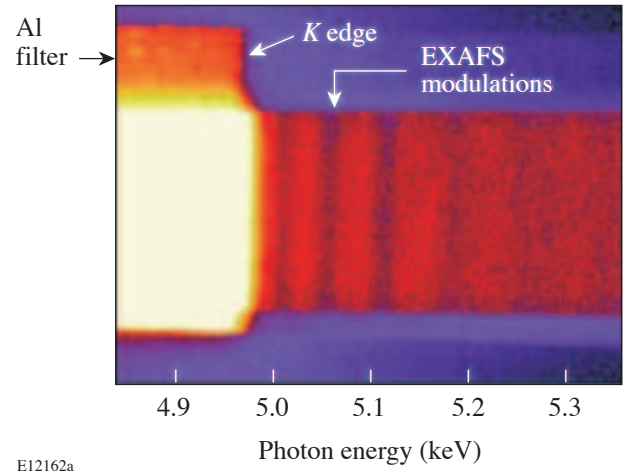


Figure 97.15 Typical record of the transmitted spectrum (from unshocked Ti) showing EXAFS modulations above the *K* edge.

Although the EXAFS measurement is time integrated, a meaningful shock diagnosis can be obtained without streaking the spectrum in time because the x-ray pulse width is ~120 ps,⁸ much shorter than the shock transit time through the metal (~2 ns). The timing of the shock relative to the implosion-induced backlighter pulse was measured by the method of active shock breakout (ASBO),¹² a method that uses a frequency-doubled YAG laser probe, reflected from the backside of the target. Figure 97.16 shows a schematic of the setup and a typical streak result; $\tau(\text{Ti})$ and $\tau(\text{CH})$ are the times when the shock has traversed the metal layer and the back CH layer, respectively. This measurement determines the correct timing between the implosion beams and shock-producing beams. It also yields the shock speed in the metal (~5 μm/ns), from which, using the known Hugoniot equation of state, the shock compression and pressure can be obtained. Finally, images such as in Fig. 97.16 indicate a lateral nonuniformity (due to the laser's focal-spot distribution) of ±10% in the shock speed, thus also in the shock compression.

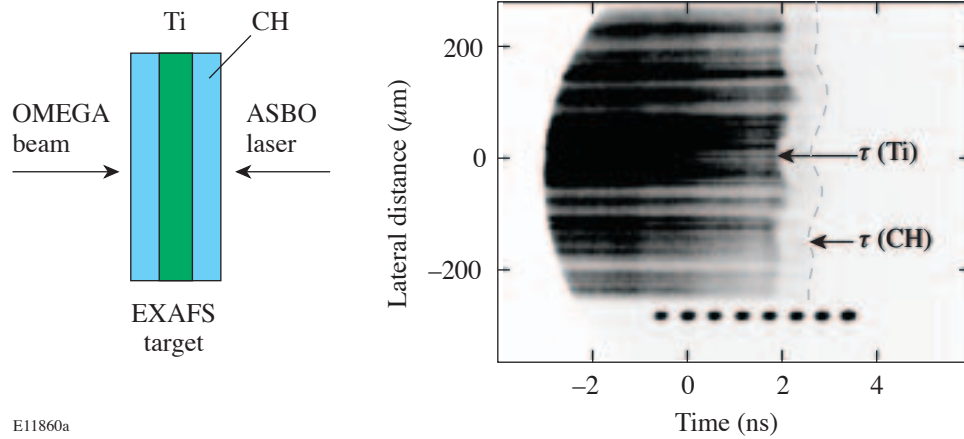


Figure 97.16

Schematic and a typical streak of the ASBO probe beam reflected from the backside of the target. $\tau(\text{Ti})$ and $\tau(\text{CH})$ are the times when the shock exits the metal layer and the back CH layer, respectively. This measurement provides (a) the correct timing between the capsule-implosion beams and shock-producing beams, (b) the shock speed in the metal, and (c) the lateral shock uniformity.

Hydrodynamic Simulations

The expected shock strength and the properties of the shocked vanadium and titanium were determined using one-dimensional simulations with the hydrodynamic code *LASNEX*.¹³ The profiles of pressure, density, and temperature versus position are shown for V in Fig. 97.17 and for Ti in Fig. 97.18, at the time of arrival of the shock at the rear surface of the metal layer for an incident laser intensity of $\sim 0.5 \text{ TW/cm}^2$. The range (around the volume average) of parameter values within the V layer is (1) pressure: $0.43 \pm 0.03 \text{ Mbar}$; (2) temperature: $980 \pm 160 \text{ K}$; and (3) volume compression: 1.19 ± 0.05 . These variations in the axial direction are larger than the lateral variations due to laser nonuniformity; for this reason a one-dimensional simulation of the shocked metals is adequate. For Ti the comparable ranges are (1) pressure: $0.33 \pm 0.05 \text{ Mbar}$; (2) temperature: $900 \pm 130 \text{ K}$; and (3) volume compression: 1.2 ± 0.06 . The EXAFS measurements (in the case where the metals were shocked) are averaged over the shocked volume; thus, the volume averages are the appropriate theoretical quantities to compare with the experiment.

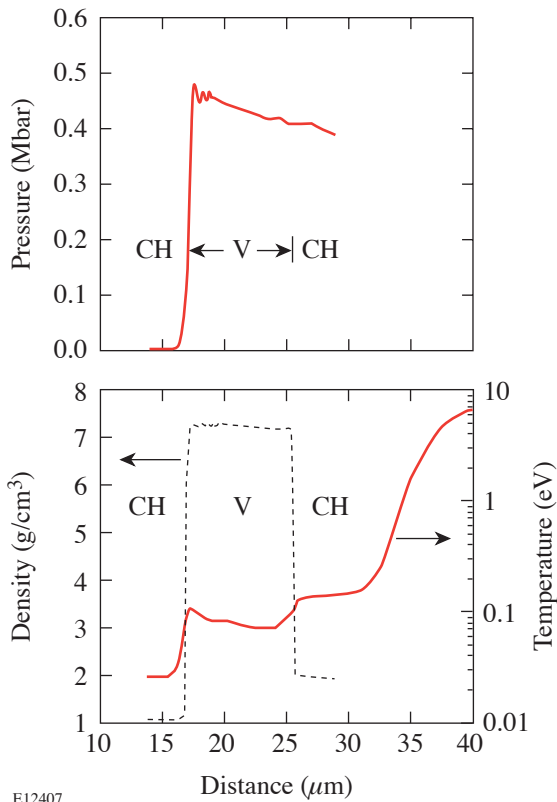
Theory

The measured spectra were analyzed with the FEFF8 *ab initio* EXAFS software package.¹⁴ The basic theory of EXAFS⁴ yields an expression for the relative absorption $\chi(k) = \mu(k)/\mu_0(k) - 1$, where $\mu(k)$ is the absorption coefficient and $\mu_0(k)$ is the absorption of the isolated atom. The wave

number k of the ejected photoelectron is given by the de Broglie relation $\hbar^2 k^2 / 2m = E - E_K$, where m is the electron rest mass, E is the absorbed photon energy and E_K is the energy of the K edge. The basic EXAFS formula for a single reflection in the plane-wave approximation is given by⁴

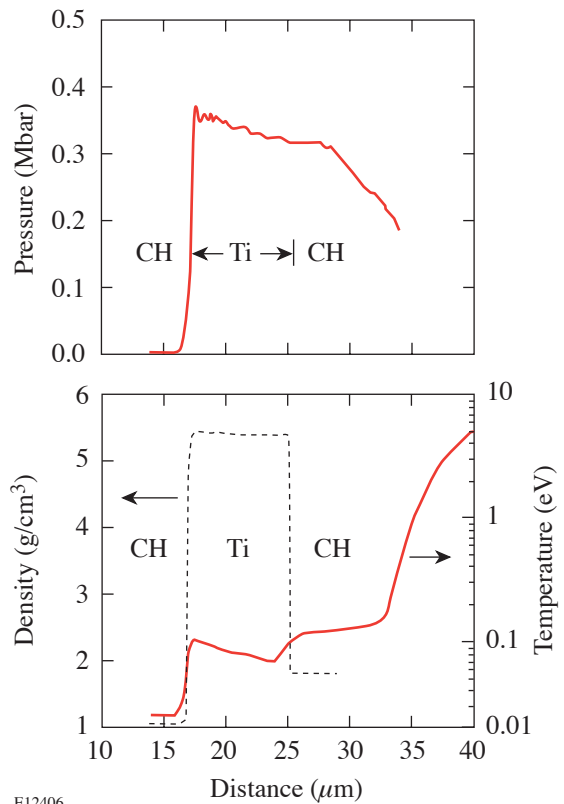
$$\chi(k) = \sum_j N_j S_0^2 F_j(k) \exp[-2\sigma^2 k^2 - 2R_j/\lambda(k)] \times \sin[2kR_j + \phi_j(k)] / kR_j^2, \quad (1)$$

where N_j is the number of atoms in the j -th shell, that is, the number of atoms surrounding the absorbing atom at a distance R_j , and $\lambda(k)$ is the electron mean free path for collisions. FEFF8 uses the scattering potential to calculate the amplitude and phase shift of the photoelectron waves scattered from several shells of neighboring atoms including multiple-scattering paths. The total $\chi(k)$ is constructed in the curved-wave approximation (i.e., the assumption of plane wave is removed) and iteratively fitted to the experimental $\chi(k)$. The main fitting parameters are the nearest-neighbor distance R and the vibration parameter σ^2 appearing in the Debye–Waller term. R yields the density or compression if we assume three-dimensional compression. The agreement of the resulting compression with the value derived from the shock-speed measurement justifies this assumption. The vibration



E12407

Figure 97.17 One-dimensional shock profiles versus position calculated by the hydrodynamic code *LASNEX* for the instant when the shock has just traversed the V layer, assuming an incident laser intensity of ~ 0.5 TW/cm² in a 3-ns square pulse.



E12406

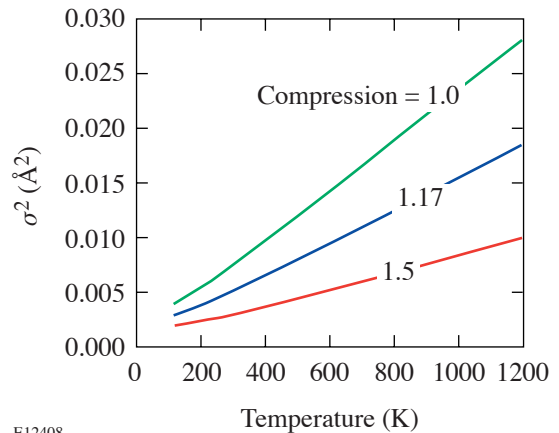
Figure 97.18 One-dimensional shock profiles versus position calculated by the hydrodynamic code *LASNEX* for the instant when the shock has just traversed the Ti layer, assuming an incident laser intensity of ~ 0.5 TW/cm² in a 3-ns square pulse.

amplitude σ^2 depends mainly on the temperature but also on the compression. σ^2 is calculated as a function of temperature, using the Debye model¹⁵ for the phonon density of states, including correlation between the motions of the absorbing and neighboring atoms; σ^2 depends on the density through the Debye temperature. The density dependence of the Debye temperature was calculated using an empirical model.⁹ Figure 97.19 shows the resulting σ^2 for V as a function of temperature and compression. As seen, compression increases the amplitude of the EXAFS signal because of the decrease in σ^2 . Similar curves have been calculated for titanium. Thus, knowing the compression and σ^2 , the temperature can be derived.

Results and Analysis

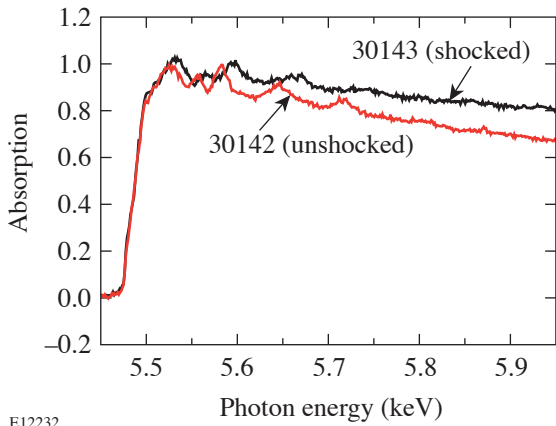
1. Vanadium

The measured absorption spectra from V are shown in Figs. 97.20 and 97.21. Figure 97.20 shows the total absorption curve in V, with and without shocking. The frequency of the



E12408

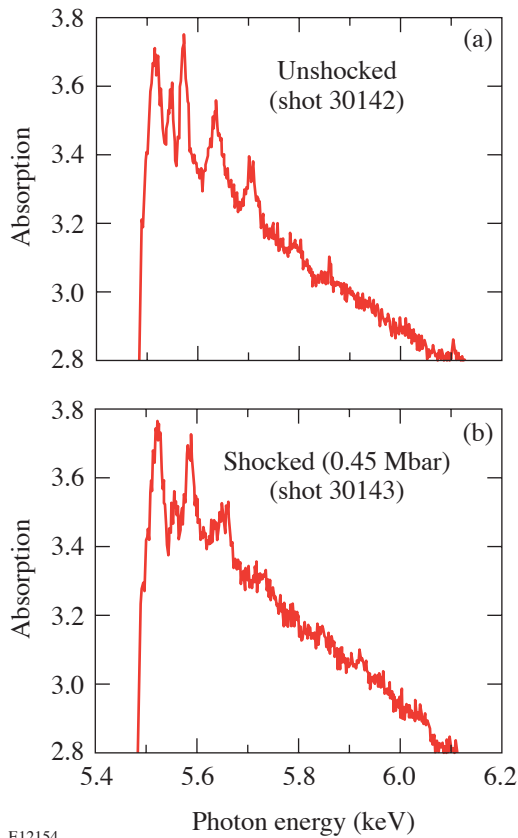
Figure 97.19 Calculated σ^2 due to thermal vibrations for V from a correlated Debye model.



E12232

Figure 97.20

Measured absorption in V (normalized to 1), with and without shocking. The lengthening of the period of EXAFS modulation in the shocked case is evidence for compression. The shock pressure was 0.45 Mbar.



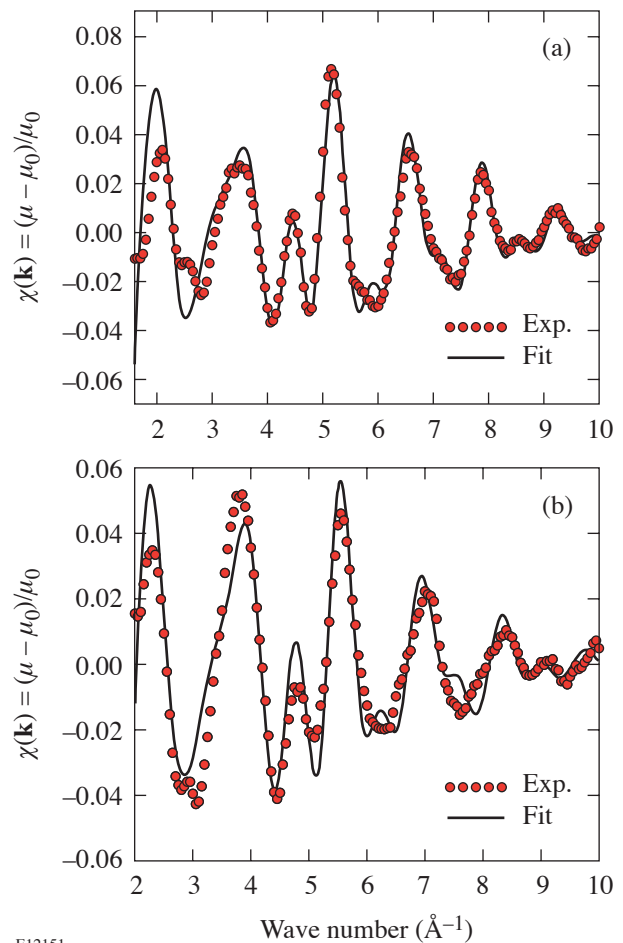
E12154

Figure 97.21

Expanded view of the EXAFS modulations in V shown in Fig. 97.20 for the unshocked case (a) and the shocked case (b). The modulations are clearly seen to decay faster when the V is shocked, due to the increased temperature. This comparison demonstrates the usefulness of EXAFS spectra in measuring the temperature of shocked metals.

EXAFS oscillations is seen to become smaller when the shock is applied. Since that frequency (in k space) is proportional to the distance R to the nearest neighbors [see Eq. (1)], the lowering of the frequency indicates a smaller R , thus a shock compression. Figure 97.21 shows a magnified view of the EXAFS modulations for the unshocked case (a) and the shocked case (b). The modulations are clearly seen to decay faster when the vanadium is shocked, due to the increased temperature. *This comparison demonstrates the usefulness of EXAFS spectra in measuring the temperature of shocked metals in the range of $T \sim 10$ to 100 meV.*

The results of fitting the V EXAFS spectra with the FEFF8 code¹⁴ for the unshocked and shocked cases are shown in Fig. 97.22. For the unshocked case, the fitting parameters were (for the first shell) $R = (2.585 \pm 0.008) \text{ \AA}$ and $\sigma^2 = (0.0111 \pm 0.0006) \text{ \AA}^2$. In the vanadium crystal (body-centered



E12151

Figure 97.22

Fitting the measured V EXAFS spectra for the unshocked case (a) and the shocked case (b) with the FEFF8 code.

cubic), the first shell has eight atoms at a distance of $(3/5)^{1/2}a$, where the crystallographic parameter a is 3.02 Å, yielding for the nearest neighbors a distance of 2.615 Å. Thus, the R found here is smaller than the expected value by ~ 0.03 Å; interestingly, the value found for R (vanadium) in V EXAFS synchrotron experiment¹⁶ was also 2.58 Å, in agreement with our value. From the measured value of σ^2 , we derive (using Fig. 97.19) the temperature 530 ± 25 K. The increase of ~ 130 K over room temperature is due to the radiation heating caused by the imploding target.

For the shocked case, the fitting parameters (for the first shell) were $R = (2.570 \pm 0.013)$ Å and $\sigma^2 = (0.0157 \pm 0.0011)$ Å². Comparing R for the unshocked and shocked cases, we derive a volume compression of $(2.585/2.570)^3 \sim 1.15$. The value of σ^2 results in a temperature of 900 ± 70 K. This increase in temperature includes the effect of radiation heating; the net temperature due to the shock alone is 770 ± 70 K.

Table 97.I summarizes the measured and computed parameters for the shocked-V experiment. EXAFS results indicate a weaker shock than predicted by *LASNEX*, but they are in agreement with the shock-speed measurement (as seen by the compression values). The measured values are accompanied by their uncertainties, whereas the *LASNEX* values are accompanied by their ranges in the axial direction. The uncertainty in the EXAFS measurement is determined by the fitting procedure and is smaller than the axial or the lateral non-uniformities described above. The EXAFS-derived values relate to the average over the shock volume. Likewise, the compression in the last column of Table 97.I is derived from the shock speed averaged (laterally) over the streak record, and its uncertainty is smaller than the range of variation in the speed.

2. Titanium

Phase transformations in shocked metals can be measured by a discontinuity in the Hugoniot curves or directly by x-ray diffraction. EXAFS can indicate a phase transformation if the Debye–Waller factor σ^2 undergoes an abrupt increase.¹⁷ This can occur if the transformation is to a disordered state or if the nearest-neighbor distances in the new crystal are disparate and

the beating of the frequencies corresponding to the various distances causes a stronger modulation damping. Shocked titanium (at much longer duration than here) is known to undergo an α -Ti to ω -Ti phase transformation at a pressure in the range of 0.029 to 0.09 Mbar, depending on sample purity.^{6,7} The pressure in this experiment is well above this range. It is not known, however, whether the transformation can occur on the nanosecond time scale. Figure 97.23 shows the EXAFS spectra from Ti, before (a) and after (b) being compressed with an ~ 0.5 Mbar shock. The experimental conditions were the same as in the vanadium experiment except

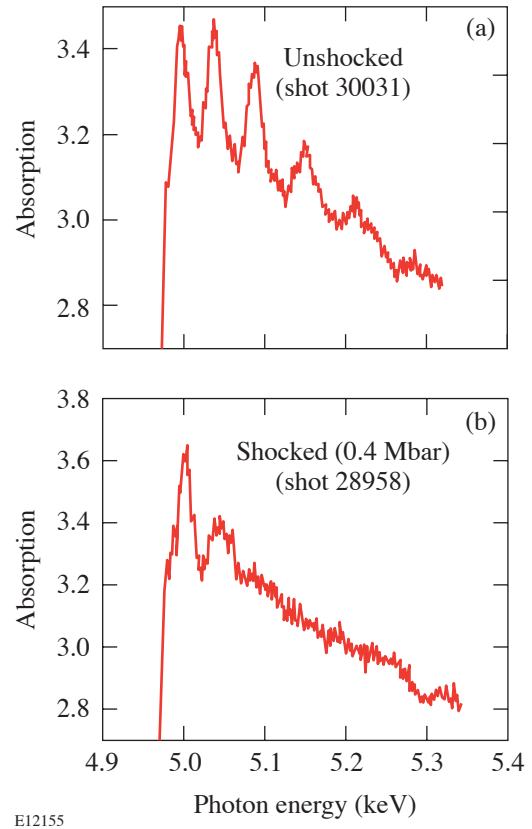


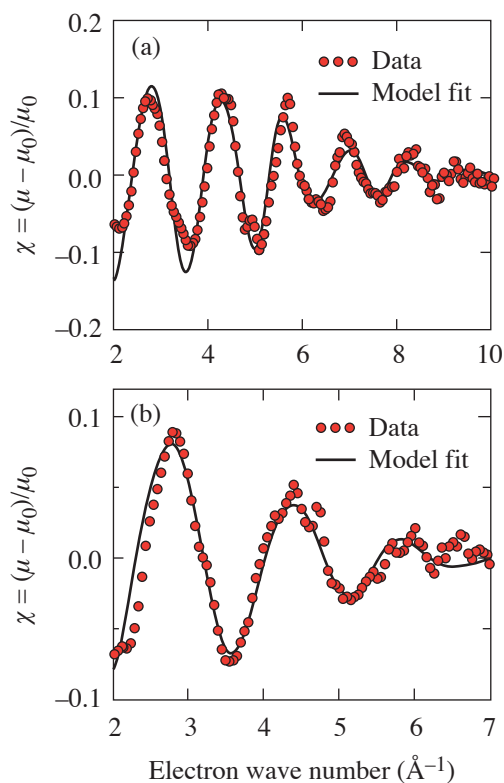
Figure 97.23 EXAFS spectra from Ti, before (a) and after (b) being compressed by a ~ 0.5 Mbar shock. The modulation with shocking is seen to be strongly damped. This is shown to reflect an α -Ti to ω -Ti phase transformation.

Table 97.I: *LASNEX*-calculated and measured parameters for shocked vanadium.

LASNEX Parameter Ranges		EXAFS Measurement		Shock-Speed Measurement
Compression	Temperature	Compression	Temperature	Compression
1.19±0.05	980±160 K	1.15±0.01	770±70 K	1.15±0.06

that the laser intensity was 0.5 TW/cm^2 . As in the case of vanadium (Fig. 97.20), the EXAFS modulations in the shocked case have a lower frequency than in the unshocked case, indicating shock compression. However, the modulations in the shocked case are seen to be much more strongly damped than in the case of vanadium. This is shown below to reflect an α -Ti to ω -Ti phase transformation.

Figure 97.24 shows the fitting of the FEFF8 EXAFS code to the measured Ti EXAFS spectra taken before (a) and after (b) the shock, assuming α -Ti for both. The first-shell fitting parameters result in a volume compression of 1.2 ± 0.03 . This compares well with the *LASNEX* value of 1.2 ± 0.06 , but the error is much larger than for vanadium. The σ^2 value of the unshocked case is 0.0088 \AA^2 , which corresponds to a temperature of 380 K. For the shocked case, $\sigma^2 = 0.029 \pm 0.008 \text{ \AA}^2$, which corresponds to a temperature of $T = 2100 \pm 570 \text{ K}$. The obtained temperature is in sharp disagreement with the *LASNEX*-predicted value ($\sim 900 \text{ K}$). This strongly suggests that the large

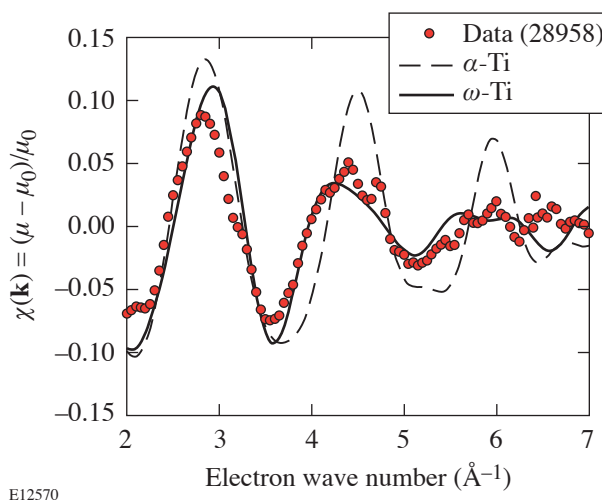


E12409

Figure 97.24

Fitting the FEFF8 EXAFS code to the measured Ti EXAFS spectra taken before (a) and after (b) being compressed by a $\sim 0.5 \text{ Mbar}$ shock, assuming α -Ti phase.

σ^2 value is not due to a high temperature but due to a structural rearrangement such as a phase transformation. The large fitting errors also suggest that the assumed crystal structure (*hcp*) is not the correct structure for the shocked titanium. These conclusions are supported by the good agreement between measurements and simulation for comparable shocks in vanadium (Fig. 97.22), where no phase transformation is expected. In fact, whereas each α -Ti atom has six equidistant neighbors, ω -Ti atoms have two possible atomic environments:⁶ at site A there are 15 neighbors at two different distances, and at site B there are 11 neighbors at three different distances. Different distances translate to different EXAFS frequencies that, through beating, cause enhanced damping. Figure 97.25 shows this to be the case. Here FEFF calculations assuming the ω -Ti crystal structure, averaging over sites A and B, were carried out for the *LASNEX*-predicted temperature of 900 K. Only the compression was adjusted to fit the experiment, and the resulting value of 1.23 is close to the predicted value of 1.2. It should be noted that the α -Ti to ω -Ti phase transformation entails an $\sim 2\%$ volume compression.⁷ Also shown is the FEFF calculation for the α -Ti phase, using the *LASNEX*-predicted temperature and adjusting the compression to agree with the data. Figure 97.25 clearly shows that assuming the ω -Ti phase agrees with the experiment much better than assuming the α -Ti phase. Thus, the damping is dominated by the crystal structure of ω -Ti rather than by the temperature.



E12570

Figure 97.25

Fitting the FEFF8 EXAFS code to the measured Ti EXAFS spectrum, assuming the α -Ti phase (the *hcp* phase at normal conditions) and the ω -Ti phase. Only the compression was adjusted (to fit the frequency of modulation) and the *LASNEX*-predicted temperature $T = 900 \text{ K}$ was assumed.

A critical test of the assumption of phase transformation can be obtained by repeating the measurement for successively weaker shocks. Figure 97.26 shows the transmitted spectrum from a Ti sample for four different values of laser intensity (volume-averaged pressures from *LASNEX* are indicated). The reduction of the intensity by a factor ~ 2 to 0.23 TW/cm^2 shows no significant change in the spectrum. This clearly proves that the high damping rate is not due to a high temperature. At an intensity of $\sim 0.12 \text{ TW/cm}^2$ (corresponding to a pressure of $\sim 0.12 \text{ Mbar}$) the damping rate is intermediate between the unshocked and shocked cases. Thus, the results are consistent with a phase transformation occurring, very roughly, around 0.12 Mbar .

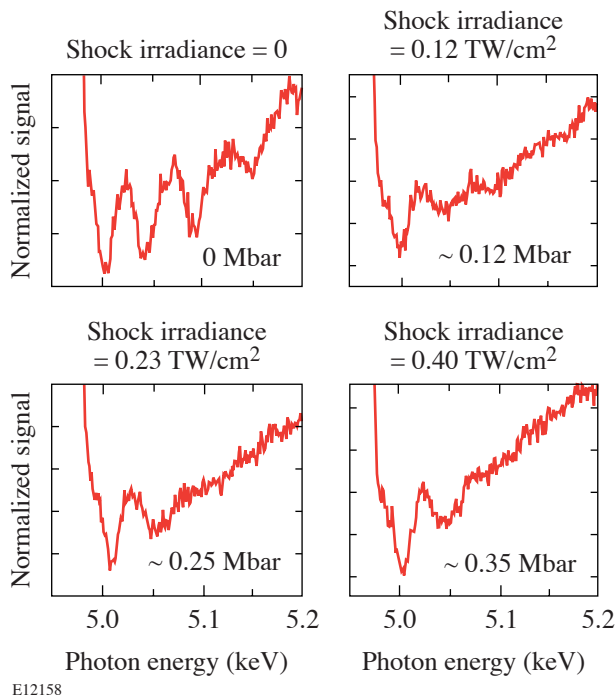


Figure 97.26 Transmitted intensity from the Ti sample for four different values of laser intensity (average pressure values from *LASNEX* are also shown). The comparison indicates that a phase transformation occurs for laser intensity of $\sim 0.12 \text{ TW/cm}^2$, which corresponds to a pressure of $\sim 0.12 \text{ Mbar}$.

Laser-shocked monocrystalline silicon was found¹⁻³ to compress uniaxially, at least during the $\sim 5\text{-ns}$ time scale of the diffraction measurement. The question arises as to whether the fast damping of the Ti EXAFS spectrum could be the result of such elastic (1-D) compression, where the varied neighbor distances would lead to beating of the corresponding EXAFS frequencies. To address this question we calculated the first-shell Ti EXAFS spectrum under the assumption of 1-D com-

pression for $\alpha\text{-Ti}$. The result is compared in Fig. 97.27 with a calculated first-shell EXAFS curve for a 3-D compression as well as with the experimental result (in Ti the contribution of more-distant shells is relatively small). The assumed 1-D and 3-D compressions (both for $T = 900 \text{ K}$) were adjusted to yield agreement between the measured and calculated EXAFS modulation frequency. In each case the coordinates of a cluster of atoms around the absorbing atom were adjusted to reflect the assumed compression. The ratio R_0/R is the reduction in distances in the direction of shock propagation (in the 1-D case). In the case of 1-D compression, the results depend on the direction of compression with respect to the atomic planes, whose orientation is different for each crystallite of the poly-

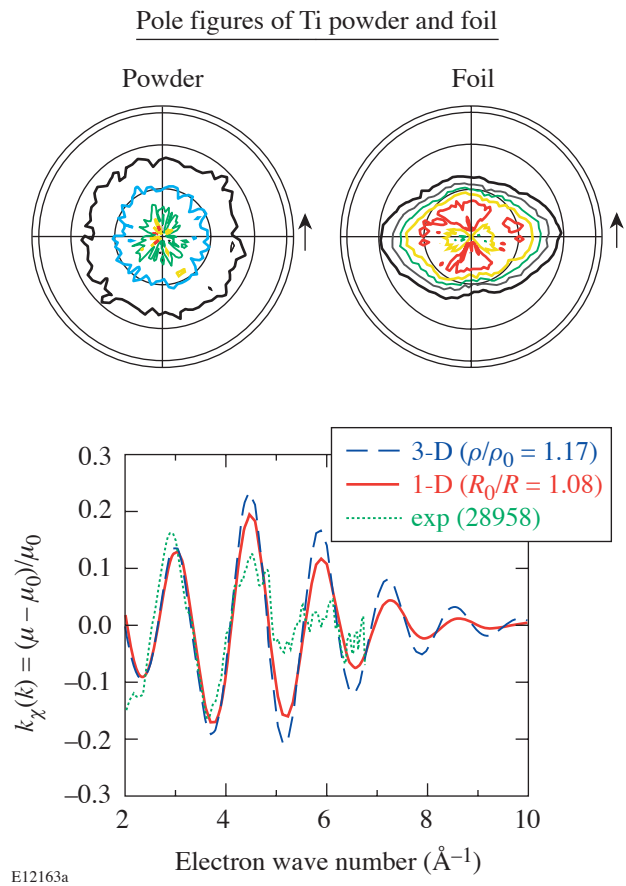


Figure 97.27 Demonstration that the fast damping of EXAFS from shocked Ti is not due to a 1-D compression. The calculated 1-D compression in $\alpha\text{-Ti}$ (in the polycrystalline sample) was averaged over all directions of (0002) poles in space, weighted by the measured pole figure of the Ti sample. The latter was normalized to the pole figure of an equivalent powdered-Ti sample.

crystalline sample. To account for this, we measured the pole figure of a Ti sample (Fig. 97.27, labeled “foil”), i.e., the statistical distribution map of the normals (or poles) to the (0002) basal planes. Since the pole-figure measurement of this distribution has an instrumental component, we corrected the result by deconvolving the measured pole figure of a powdered, i.e., an isotropically distributed, Ti sample (see Fig. 97.27). The 1-D curve in Fig. 97.27 was obtained by averaging the EXAFS spectrum of the compressed cluster over all pole directions in space, weighted by the pole figure (normalized as explained above). Figure 97.27 shows that 1-D compression does increase the EXAFS damping rate but not nearly enough to explain the measurements. We therefore conclude that the observed high damping rate in shocked Ti is very likely due to the α -Ti to ω -Ti phase transformation. Furthermore, the agreement of compression in Ti and V deduced from shock-speed and EXAFS measurements indicates 3-D compression, since the latter has been assumed in order to arrive at a compression value from the EXAFS results.

ACKNOWLEDGMENT

The pole figures obtained by Prof. S. Burns are gratefully acknowledged. This work was supported by the U.S. Department of Energy Office of Inertial Confinement Fusion under Cooperative Agreement No. DE-FC03-92SF19460, the University of Rochester, and the New York State Energy Research and Development Authority. The support of DOE does not constitute an endorsement by DOE of the views expressed in this article.

REFERENCES

1. D. H. Kalantar *et al.*, Phys. Plasmas **7**, 1999 (2000); D. H. Kalantar *et al.*, Phys. Plasmas **10**, 1569 (2003).
2. L. Loveridge-Smith, A. Allen, J. Belak, T. Boehly, A. Hauer, B. Holian, D. Kalantar, G. Kyrala, R. W. Lee, P. Lomdahl, M. A. Meyers, D. Paisley, S. Pollaine, B. Remington, D. C. Swift, S. Weber, and J. S. Wark, Phys. Rev. Lett. **86**, 2349 (2001).
3. P. A. Rigg and Y. M. Gupta, Phys. Rev. B, Condens. Matter **63**, 094112 (2001).
4. P. A. Lee *et al.*, Rev. Mod. Phys. **53**, 769 (1981).
5. T. R. Boehly, R. S. Craxton, T. H. Hinterman, J. H. Kelly, T. J. Kessler, S. A. Kumpan, S. A. Letzring, R. L. McCrory, S. F. B. Morse, W. Seka, S. Skupsky, J. M. Soures, and C. P. Verdon, Rev. Sci. Instrum. **66**, 508 (1995).
6. S. K. Sikka, Y. K. Vohra, and R. Chidambaram, Prog. Mater. Sci. **27**, 245 (1982).
7. C. W. Greeff, D. R. Trinkle, and R. C. Albers, J. Appl. Phys. **90**, 2221 (2001).
8. B. Yaakobi, F. J. Marshall, T. R. Boehly, R. P. J. Town, and D. D. Meyerhofer, J. Opt. Soc. Am. B **20**, 238 (2003).
9. R. M. More *et al.*, Phys. Fluids **31**, 3059 (1988).
10. R. W. Eason *et al.*, J. Phys. C, Solid State Phys. **17**, 5067 (1984).
11. B. A. Shiwai *et al.*, Laser Part. Beams **10**, 41 (1992).
12. P. M. Celliers *et al.*, Appl. Phys. Lett. **73**, 1320 (1998).
13. G. B. Zimmerman and W. L. Kruer, Comments Plasma Phys. Control. Fusion **2**, 51 (1975).
14. J. J. Rehr, R. C. Albers, and S. I. Zabinsky, Phys. Rev. Lett. **69**, 3397 (1992).
15. E. Sevilano, H. Meuth, and J. J. Rehr, Phys. Rev. B, Condens. Matter **20**, 4908 (1979).
16. G. Hug *et al.*, Ultramicroscopy **59**, 121 (1995).
17. A. Yoshiasa *et al.*, J. Synchrotron Radiat. **6**, 43 (1999).

Picosecond Response of Ultraviolet Photodiodes on GaN

Experimental results on the fabrication, packaging, and testing of very fast metal-semiconductor-metal photodiodes (MSM-PD's) made on gallium nitride (GaN) have been previously reported.¹ The devices—with feature sizes ranging from 0.3 μm to 5 μm —were packaged in a circuit that was designed to easily couple the electrical transients out of the device, thus making them suitable for practical applications. A temporal response of 55 ± 5 -ps full width at half maximum (FWHM) was measured in all devices, independent of feature size. External bias was changed from 1 V to 10 V, and the device area was decreased by a factor of 4 to reduce the total capacitance, neither of which had a significant effect on the measured speed. Only high illumination levels produced a change in the device response. This change was attributed to space-charge screening effect. These results led to the conclusion that the device response was dominated by the packaging and measurement system. Theoretical calculations^{2–5} have predicted, however, that the steady-state peak electron velocity in GaN is around 3×10^7 cm/s, which is higher than that in GaAs. This implies that the inherent speed in GaN detectors should be substantially faster than in GaAs devices. Joshi *et al.*,⁶ in particular, using Monte Carlo simulations, studied the dynamic response of GaN MSM-PD and predicted a FWHM of 3.5 ps for a device with 0.25- μm feature size under low-bias and low-level illumination.

To explore the inherent device response, a double-pulse measurement was performed¹ by splitting the optical beam into two parts with an adjustable delay and then recombining them to excite the device under test. Separable pulses from a typical device were observed at delays of less than 26 ps, confirming a much-faster inherent response.

In this article results measured with electro-optic (EO) sampling are reported.^{7,8} This technique is connector-free and has a bandwidth of more than 1 THz, corresponding to a temporal resolution of 360 fs, providing a much-faster measurement system. To minimize the capacitance effect inherent to the MSM structure, small devices with active area of $25 \times 25 \mu\text{m}^2$ were selected. The sampling point, defined by the

laser spot, was close to the active device area. A sufficient time window existed (about 15 ps) before the transient reflections from the circuit terminals set in, ensuring that the measurement of the intrinsic response could be separated from the packaging circuit.

The devices were made on GaN wafers (2- μm thickness) grown on c-plane sapphire and purchased from a commercial source. The residual impurities produced an electron concentration below $1 \times 10^{16} \text{ cm}^{-3}$. Fabrication was carried out at the Cornell Nanofabrication Facilities (CNF) using electron-beam lithography. Metallization used to form Schottky contacts was either Ni/Au or Ti/Pt. Details of the device fabrication can be found in Ref. 1.

The device was excited by beams from a femtosecond, frequency-doubled, Ti:sapphire, mode-locked laser tuned at $\lambda = 720$ nm, with a 76-MHz repetition rate and an average power of 1 mW. The fundamental beam was used to probe the photogenerated electrical signal via a movable LiTaO₃ electro-optic crystal positioned close to the active area (Fig. 97.28), which served as a detector of the electrical transient. The excitation beam was focused down to the active area without passing through the electro-optic (EO) crystal. To maximize the EO coupling, the sampling beam was precisely focused on the edge of the metal pad, where the strongest electric field is located. The distance between the ends of the metal pads (1.3 mm in Fig. 97.28) defines the onset of the first reflection of the electric pulse and was seen in the evanescent portion of the transient. The dc bias needed to generate the dark electric field between the fingers was applied via wire bonds.

It should be noted that even though the optical wavelength of 360 nm was only 5 nm above the energy gap of the GaN film, the penetration depth was around 370 nm, as determined by transmission measurement at this wavelength. This is significantly shorter than the 2- μm thickness of GaN film and the 1- μm distance of the finger spacing. Therefore, the deep-carrier effect as observed in a silicon MSM diode⁹ is negligible here.

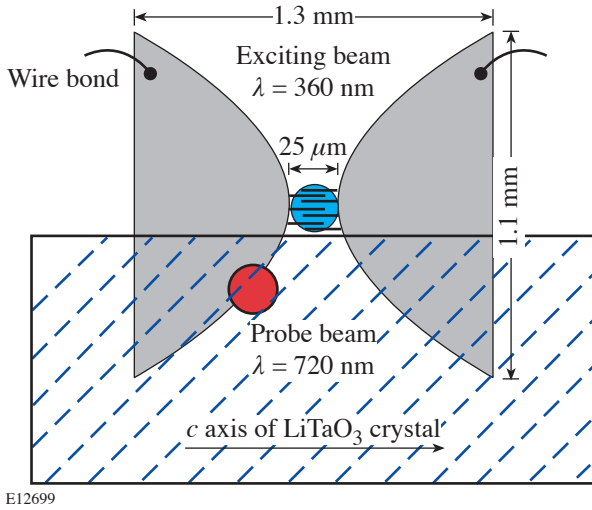


Figure 97.28
A schematic view of the sample configuration for measuring the electrical response of the MSM GaN photodiodes.

Figure 97.29 shows the fastest temporal response of the photodiode with 1-μm finger width and spacing and 25 × 25-μm² active area, under 12-V bias. The pulse shape in Fig. 97.29 is strongly asymmetrical: the 1.4-ps rise time is limited by the optical pulse width and by the RC time constant

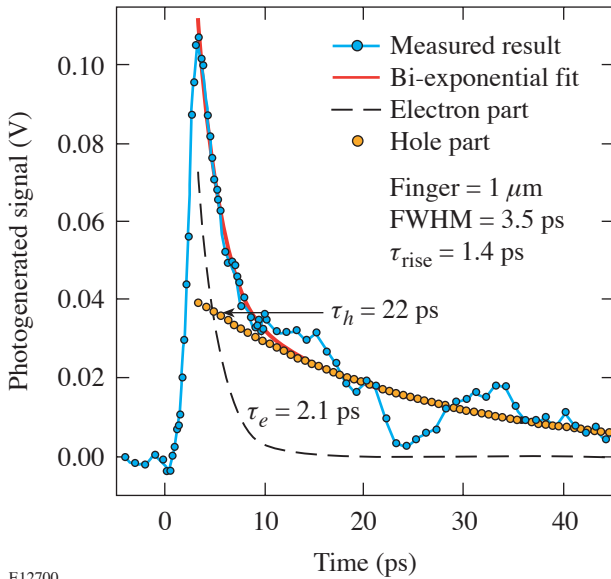


Figure 97.29
Electrical pulses generated by illumination of 360-nm photons and the bi-exponential fitting. The finger spacing and width of the diode are both 1 μm.

in the MSM structure and pads. The slower trailing transient, determined by the carrier transit across the finger gap, can be fitted with a bi-exponential function with time constants of 2.1 ps and 22 ps. They are attributed to the electron and the hole components, respectively. It should be pointed out that while the faster electron part is closely fitted with an exponential, the slower hole component is masked with reflections from the ends of the metal pads.

The electron velocity from the ratio of the half-distance between the electrodes (0.5 μm) to the measured FWHM (3.5 ps) is estimated to be $1.43 \pm 0.1 \times 10^7$ cm/s. This result compares favorably with the value of 1.5×10^7 cm/s measured^{10,11} under an electric field of 120 kV/cm in a femto-second optical time-of-flight experiment that monitors the change in the electro-absorption associated with the transport of photogenerated carriers in a GaN *p-i-n* diode.

The dependence of pulse duration and electron velocity on the electric field was extracted by changing the bias voltage from 5 V to 14 V. The inset in Fig. 97.30 shows the measured FWHM as a function of average electric field, which is calcu-

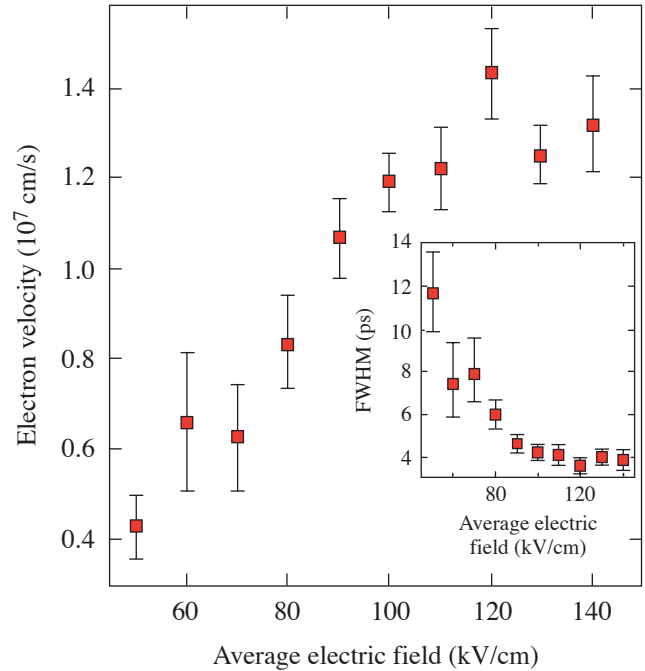


Figure 97.30
The experimentally determined electron velocity and measured FWHM (inset) as a function of average electric field.

lated by dividing the bias voltage by 1- μm finger spacing. In the low-field region, the experimentally determined electron velocity, shown in Fig. 97.30, increases with bias. Above 100 kV/cm, the electron velocity begins to flatten, reaching a plateau at 120 kV/cm. If the average of the plateau region is used, rather than the peak, then the estimated electron velocity becomes $1.3 \pm 0.1 \times 10^7$ cm/s. The fact that the peak velocity measured in our experiment is lower than the calculated steady-state peak electron velocity for GaN² may be attributed to the high defect density in the device and/or the capacitance effect of MSM structure that are not accounted for by theory.

The high-field results of Fig. 97.30 can be compared with Monte Carlo simulations.⁶ For a device with 0.25- μm finger spacing, the corresponding FWHM is expected to be around 1 ps, based on our measured electron speed. This is substantially faster than the simulated results of 3.5 ps.⁶ To check further, a device with 0.5- μm finger spacing was tested. A typical transient, shown in Fig. 97.31, shows two features distinct from the 1- μm device: a slower rise time of 3.2 ps and a broader FWHM of 6.2 ps. This result is at first surprising; however, it is consistent with an increased capacitance that dominated the measured response from the smaller device. In the MSM structure, the device capacitance increases with

smaller finger spacing. For our samples, the capacitances are calculated¹² to be 0.0126 pF and 0.0263 pF for the 1- μm and 0.5- μm devices, respectively. With a measured package-circuit impedance of 63 Ω ,¹ the corresponding RC time constant would increase with increased capacitance and gives a 10%–90% rise time of 3.7 ps for the 0.5- μm device, essentially accounting for the slower response observed in Fig. 97.31. Further comparison with theory will then require devices fabricated with much smaller detection areas.

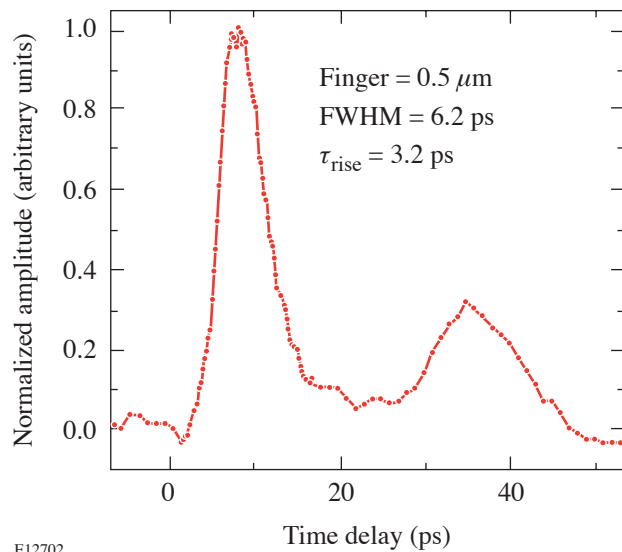
In summary, EO sampling has been used to test the intrinsic response of GaN MSM photodiodes. The best performance measured from devices with 1- μm feature size showed a fast 10%–90% rise time of 1.4 ps and FWHM of 3.5 ps. This result represents the fastest ultraviolet GaN photodiode reported to date. The peak velocity of electrons in GaN was determined to be 1.43×10^7 cm/s, which compares favorably with independent photoexcitation experiments.

ACKNOWLEDGMENT

This work was supported by the U.S. Department of Energy Office of Inertial Confinement Fusion under Cooperative Agreement No. DE-FC03-92SF19460, the University of Rochester, and the New York State Energy Research and Development Authority. The support of DOE does not constitute an endorsement by DOE of the views expressed in this article.

REFERENCES

1. J. Li, W. R. Donaldson, and T. Y. Hsiang, *IEEE Photonics Technol. Lett.* **15**, 1141 (2003).
2. U. V. Bhapkar and M. S. Shur, *J. Appl. Phys.* **82**, 1649 (1997).
3. J. D. Albrecht *et al.*, *J. Appl. Phys.* **83**, 4777 (1998).
4. J. Kolnik *et al.*, *J. Appl. Phys.* **78**, 1033 (1995).
5. B. Gelmont, K. H. Kim, and M. Shur, *J. Appl. Phys.* **74**, 1818 (1993).
6. R. P. Joshi, A. N. Dharamsi, and J. McAdoo, *Appl. Phys. Lett.* **64**, 3611 (1994).
7. S. Alexandrou, R. Sobolewski, and T. Y. Hsiang, *IEEE J. Quantum Electron.* **28**, 2325 (1992).
8. U. D. Keil and D. R. Dykaar, *Appl. Phys. Lett.* **61**, 1504 (1992).
9. C.-C. Wang, S. Alexandrou, D. Jacobs-Perkins, and T. Y. Hsiang, *Appl. Phys. Lett.* **64**, 3578 (1994).
10. M. Wraback *et al.*, *Appl. Phys. Lett.* **76**, 1155 (2000).
11. M. Wraback *et al.*, *Appl. Phys. Lett.* **79**, 1303 (2001).
12. Y. C. Lim and R. A. Moore, *IEEE Trans. Electron Devices* **ED-15**, 173 (1968).



E12702

Figure 97.31
Impulse response measured from a device with 0.5- μm finger width and spacing. Both rise time and FWHM are longer than those from a device with 1- μm finger width and spacing as discussed in text.

Self-Assembly of Coated Colloidal Particles for Optical Applications

Introduction

Nearly two decades ago, theoretical predictions indicated the possibility of creating omnidirectional photonic-band-gap materials that would prevent the propagation of certain wavelengths of light in all directions, while allowing transmission of other light wavelengths.^{1,2} Since that time, there has been a growing interest in creating these materials experimentally due to the wide variety of potential applications afforded by the control of light propagation, including use in optical computing and telecommunications.³ Researchers have taken two approaches to construction of photonic-band-gap materials: (1) lithographic technologies similar to that used in microelectronics manufacture and (2) colloidal self-assembly of spherical particles. The self-assembly approach is promising due to its simplicity and low cost.

Under appropriate conditions, spherical colloidal particles will self-assemble to form a hexagonal close-packed structure called a “colloidal crystal.” There are regularly spaced air voids in the interstitial regions between colloidal particles making up the crystal. Since air has a much lower refractive index than the particles, the refractive index of the crystal varies periodically on a length related to the diameter of the particles making up the crystal. The periodic variation of refractive index within the colloidal crystal leads to preferential reflection of certain wavelengths of light. The maximum reflectance occurs at a wavelength equal to roughly twice the diameter of the particles making up the crystal. Therefore, the position of the band gap and thus the color of the crystal may be adjusted by adjusting the size of the particles making up the crystal. Colloidal crystals are often referred to as “photonic crystals” due to the photonic-band-gap properties. They are also referred to as “artificial opals” due to the similarity with gemstone opal. Naturally occurring opal is a colloidal crystal of spherical silica particles. The “opalescence” observed in gemstone opal is caused by preferential reflection of light within the photonic band gap.

Colloidal crystals exhibit a “pseudo” photonic band gap; that is, only a portion of the light in the photonic band gap is

reflected while some fraction propagates into the crystal. The rejected fraction of light can be enhanced by increasing the refractive index contrast between the particles and air voids in the structure. The photonic band gap is also very sensitive to the quality of the crystal. A few faults or dislocations in the crystal structure will greatly diminish the intensity of the reflected light. It is desirable to have a complete photonic band gap with 100% of the light in the band gap reflected. Theoretical predictions have indicated, however, that even with a perfect colloidal crystal, a full band gap may not be attained, no matter how high the refractive index contrast.⁴ Since a simple colloidal crystal is unable to form a complete band gap, researchers have focused on creating more complex structures to attempt to create a complete photonic band gap. One approach is to form binary colloidal crystals made up of two different-sized particles.⁵ Another approach is to use the colloidal crystal as a template for creating an “inverse opal” structure in which the air voids within a colloidal crystal are filled and then the colloidal particles are removed, leaving spherical hexagonally close packed holes in a solid matrix.⁶ The inverse opal structure has been shown to yield a complete photonic band gap.³ Yet another approach is to form colloidal crystals from core-shell structured particles.⁷ Theoretical predictions indicate that colloidal crystals of some types of core-shell particles should exhibit a full photonic band gap.⁸

In the present study, core-shell structured particles were formed using electrostatic layer-by-layer self-assembly as depicted in Fig. 97.32. In the layer-by-layer technique, coatings of polyelectrolytes with alternating charges are deposited onto colloidal particles through electrostatic attraction.⁹ In addition to polyelectrolytes, other charged species may be deposited during the coating process, including proteins and luminescent nanoparticles.¹⁰ The thickness of the polyelectrolyte shell surrounding the particle may be adjusted by the number of layers deposited. Each layer deposited is typically of the order of 1 nm thick. Layer-by-layer self-assembly is a simple, versatile technique for controlling size and composition of colloidal particles with nanometer-scale precision. Typically, only a small fraction of the ionic groups in the

polyelectrolytes are neutralized during deposition. After coating, therefore, ionic species such as organic dyes or fluorophores may be immobilized in the shell via ion exchange with the polyelectrolyte counterions. By introducing luminescent or high-refractive-index species in the shell surrounding the particles, the technique offers potential as a simple route for creating optically modified particles that may be used to create photonic crystals with enhanced properties.

A variety of techniques may be employed to crystallize electrostatically charged colloidal particles. The simplest technique is simple evaporation of a few drops of an aqueous colloid on a clean, flat surface. If the surface has the same electrostatic charge as the suspended particles, opalescent colloidal crystals will form as the water evaporates. At room temperature, complete drying occurs in a few hours. Crystals are generally deposited on the outer fringes of where the droplets were placed on the surface, similar to “coffee ring” formation. While simple evaporation provides a relatively rapid route to crystallization, crystal quality is usually poor with small domain sizes. Also, it is not possible to control crystal area and thickness to obtain a uniform crystalline film over a large area of the surface.

If the liquid interface is moved across the surface at a constant velocity while evaporating, a colloidal crystal can be deposited as a uniform thin film. Colvin *et al.*¹¹ demonstrated that a uniform crystalline film can be deposited as a liquid interface moves down a solid surface, referred to as “vertical deposition.” The technique involves placing a clean glass slide oriented perpendicular to the liquid surface of the colloidal suspension so that the glass is partially submerged. As the solvent evaporates, a crystalline deposit forms where the

meniscus meets the slide surface. A thin crystal film forms over a large area of the slide surface as the meniscus slowly moves downward due to solvent evaporation. Vertical deposition was first reported for colloidal silica suspended in ethanol and is effective because of the relatively rapid rate of evaporation of ethanol. For aqueous colloids, vertical deposition is also effective, but the lower rate of evaporation makes the time required prohibitively long. Fujishima *et al.*¹² recently modified the vertical deposition technique by slowly lifting the glass slide from the colloidal suspension, as shown in Fig. 97.33. By lifting, aqueous colloids can be crystallized more rapidly than in the case where the meniscus moves

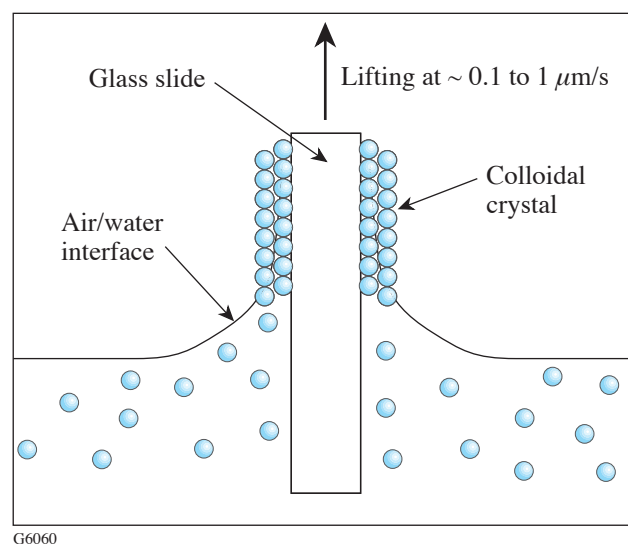
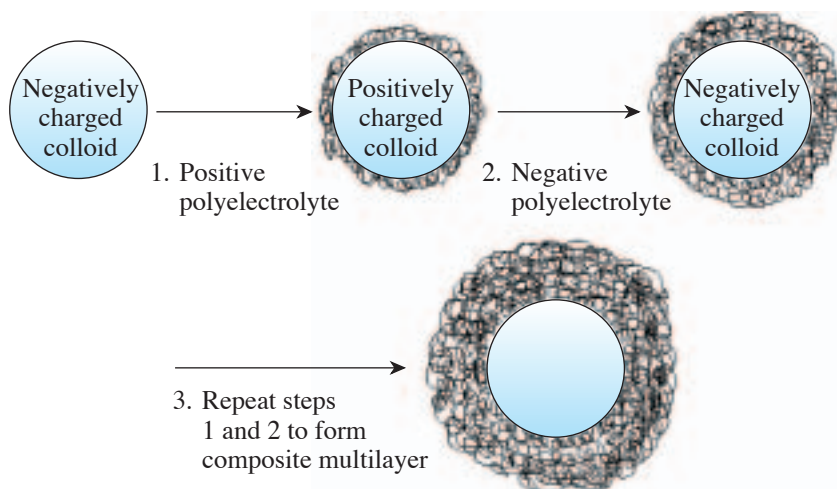


Figure 97.33
Vertical deposition technique for colloidal crystallization.



G6059

Figure 97.32

Layer-by-layer electrostatic self-assembly technique for coating colloidal particles with polyelectrolytes. The technique may also be employed to coat particles with a variety of electrostatically charged species including nanoparticles and proteins. After shell formation, charged species may be immobilized through ion exchange with the polyelectrolyte counterions.

downward by solvent evaporation. In addition, the thickness of the crystal may be adjusted by varying the lifting velocity, with thinner crystals forming with higher lifting velocity. Fujishima's technique was used in the present study to crystallize core-shell structured particles.

Experimental

Monodisperse-sized polystyrene particles (640 and 270 nm in diameter) were purchased from Microparticles GmbH Berlin, Germany. Poly(sodium 4-styrene sulfonate) (PSS, MW = 70,000 g/mol), poly(allylamine hydrochloride) (PAH, MW = 15,000 g/mol), sodium chloride (NaCl, 99%), hydrogen peroxide (30% aqueous solution), and ammonium hydroxide (28% aqueous solution) were purchased from Sigma-Aldrich and used as received. Glass microscope slides (Fisher Scientific) were cleaned prior to use by heating at 70°C for 15 min in a solution of hydrogen peroxide, ammonium hydroxide, and deionized water in a ratio of 1:1:5, respectively, by volume. After cleaning, microscope slides were stored under deionized water until used. Particles were crystallized through vertical deposition from an ~1-wt% colloidal suspension by lifting a clean glass slide at a velocity of 0.15 $\mu\text{m/s}$.

Findings

1. Crystallization of Uncoated Colloidal Particles

Vertical deposition of 270-nm-diam polystyrene particles produced the crystals shown in Fig. 97.34. Figure 97.34(a) is a high-magnification image (1- μm bar) showing hexagonal packing and long-range order of the crystal on the surface. The crystal quality is very good, although there are some faults and

dislocations in the structure. In addition, there are periodically cracks in the crystal due to contraction of the crystal upon drying. Figure 97.34(b) is a low-magnification image (10- μm bar) of the same sample showing drying cracks in the crystalline film. It was not possible to eliminate drying cracks in the sample. Overall, however, vertical deposition produces the highest-quality crystals of the techniques investigated. A crystalline film covering a 1-cm² area can be formed rapidly (in approximately 12 h), and several crystals can be formed in parallel. In addition, the optical properties of the crystals can be studied using standard reflectance or transmission spectroscopy since the crystals form in a thin film on a microscope slide. Vertical deposition with controlled lifting was used exclusively for crystallization of coated colloidal particles because of the numerous advantages of the technique over the others that were studied.

2. Crystallization of Coated Colloidal Particles

Initial coating experiments were conducted using 640-nm-diam polystyrene colloids that had sulfate groups on their surface. These negatively charged particles were coated with alternating PAH/PSS layers using an established procedure from the literature.⁷ The coating procedure has been optimized for particles near 640 nm in diameter. Briefly, each polyelectrolyte layer was deposited from an aqueous solution containing 1 mg/mL of polyelectrolyte and 0.25 M of NaCl. The high salt concentration has been shown to produce thicker polyelectrolyte layers by screening electrostatic repulsion in the polyelectrolyte chain to allow a more-coiled polymer conformation. After each coating step, the particles were washed three times

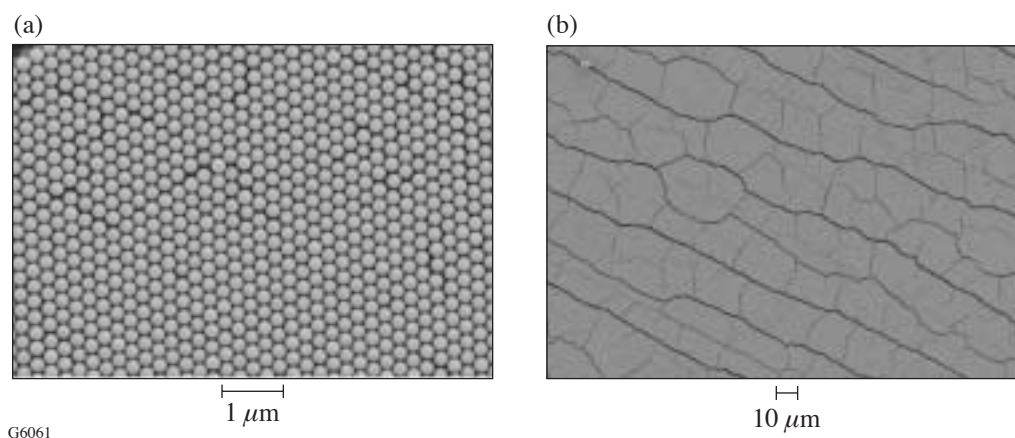


Figure 97.34

Crystals of uncoated polystyrene colloids (270-nm diam) formed through vertical deposition. (a) A high-magnification image (1- μm bar) shows the hexagonal packing and long-range order of the crystal. (b) A low-magnification view (10- μm bar) of the same sample shows drying cracks in the crystalline film.

with pure deionized water using repeated centrifugation/redispersion steps prior to coating the next layer. Particles coated in this manner had minimal aggregation and could be crystallized rapidly by placing a few drops of an ~ 1 -wt% suspension onto a clean glass slide and allowing it to evaporate as reported by Liang.⁷ While crystal formation is rapid, the crystal area is small and difficult to control, as discussed above. We focused on vertical deposition to create high-quality crystals from coated colloids over a large surface area.

The position of the photonic band gap is at a wavelength equal to roughly twice the diameter of the particles making up the crystal, which, for 640-nm-diam particles, places the band gap in the near-infrared region. Our interest is in creating photonic crystals with band gaps in the visible-light wavelength range (~ 400 to 700 nm). Therefore, we began investigating methods to coat and crystallize smaller 270-nm-diam particles. An initial attempt at coating these smaller particles was made using the same coating procedure that had been effective for 640-nm-diam particles. It was found, however, that gross aggregation of the particles occurred after the first layer was deposited. The particles were very difficult to redisperse after centrifugation. Aggregation could be minimized by placing the particles into an ultrasonic cleaning bath to disperse. Once dispersed, the particles were centrifuged slowly for several minutes to sediment aggregated particles. The aggregated particles were redispersed by the ultrasonic cleaning bath. This sedimentation/redispersion process was repeated several times to minimize aggregation of particles; however, aggregation could not be completely eliminated.

In the first attempts to crystallize the coated 270-nm particles via vertical deposition, nothing was deposited onto the glass surface because of slow flocculation of the particles. It was postulated that some rearrangement of the polyelectrolyte multilayers was occurring and leading to flocculation. If the polyelectrolytes rearrange so that portions of the oppositely charged layer beneath the outermost layer are exposed, this will lead to patches of both positive and negative electrostatic charge on the particle surface. Flocculation will then occur via electrostatic attraction between particles. To maintain electrostatic repulsion, the coated particles were kept in a dilute solution (0.1 mg/mL) of polyelectrolyte with the same charge as the outermost layer on the particle surface. If any oppositely charged patch is exposed, the free polyelectrolyte in solution around the particles can adsorb to cover it more rapidly than a charged particle will attach via flocculation. The stability of the particles was greatly enhanced by the small excess polyelectrolyte. In pure water, the 270-nm-diam polyelectrolyte-

coated polystyrene particles flocculated and sedimented in less than one day. In 0.1 -mg/mL polyelectrolyte solution, there was no visible flocculation of the particles even after two weeks.

The PAH/PSS-coated, 270-nm polystyrene particles were crystallized via vertical deposition from an ~ 1 -wt% aqueous suspension (containing 0.1 mg/mL of PSS for maintaining colloidal stability). Figure 97.35 shows scanning-electron-microscopy images of the crystalline deposit. Figure 97.35(a) is the deposit formed by particles coated with two polyelectrolyte layers. By comparison with crystals of uncoated particles (Fig. 97.34), it can be seen that the coated particles produce a much-lower-quality crystal. Hexagonal packing is present, but there are many areas where the crystal structure is disrupted. Figure 97.35(b) shows the deposit formed from particles

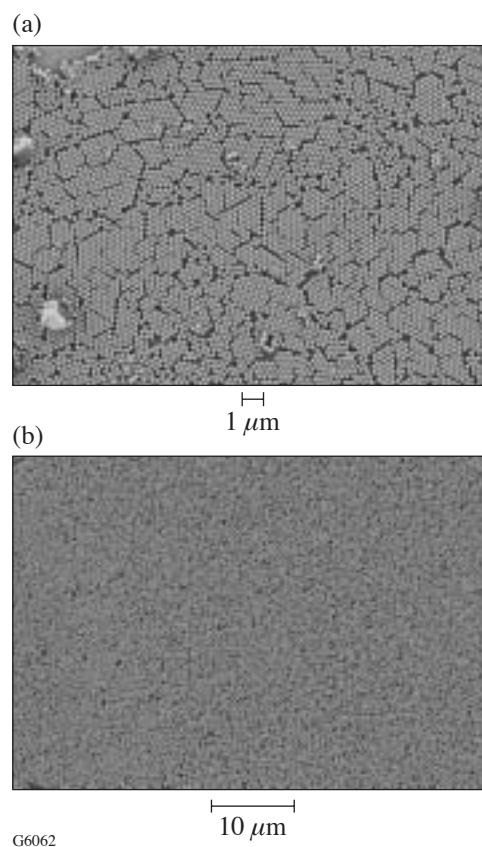
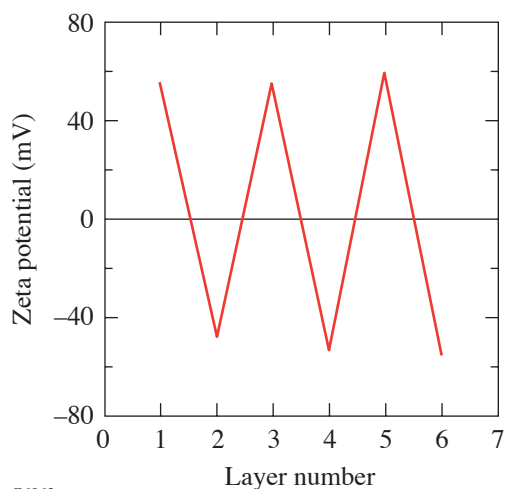


Figure 97.35 Crystals of 270-nm-diam polystyrene particles coated using the “standard” coating procedure with 0.25 -M NaCl concentration. (a) Particles coated with two polyelectrolyte layers (1 - μ m bar). Some hexagonal packing is observed, but crystal quality is poor. (b) Particles coated with four alternating polyelectrolyte layers (10 - μ m bar). Crystallization is completely disrupted due to aggregation of the particles during the coating process.

coated with four alternating PAH/PSS layers. After four coating layers, the crystal structure is completely disrupted. The coating process introduces aggregation of the particles, and aggregation increases after each layer is coated. The procedure developed for coating 640-nm particles is clearly not as effective for coating the smaller 270-nm particles.

A greatly improved coating procedure was developed following modifications suggested recently by Gittins.¹³ In Gittins' study, gold nanoparticles as small as 11-nm diameter were coated with polyelectrolyte layers without inducing particle aggregation. It was reported that much-lower salt concentration (1 mM) was required to prevent aggregation of the particles. It is well known that salt reduces electrical double-layer repulsion between particles. By lowering the salt concentration, electrostatic repulsion could be maintained while coating the particles. The same approach was applied for coating 270-nm polystyrene colloids. The particles were coated with alternating layers of PAH and PSS using solutions containing 1 mg/mL of polyelectrolyte and 1 mM of NaCl (instead of 0.25 M of NaCl). With the lower salt concentration, the aggregation of particles was greatly reduced. Upon centrifugation of the coated particles, the sediment appeared opalescent, indicating crystal formation. The crystal formation in the sediment also suggested there was very little particle aggregation and strong electrostatic repulsion was being maintained throughout the coating process.

To test if the new procedure was coating the particles as expected, the zeta potential was measured after each layer was deposited. Figure 97.36 shows the zeta potential results. The zeta potential is related to the surface charge of the particles.



G6063

The sign of the zeta potential alternates from positive to negative as expected when the alternating polyelectrolyte layers are deposited. The high magnitude of the zeta potential (>40 mV for every layer) indicates that good colloidal stability is maintained. Unfortunately, we could not measure the growth of the polyelectrolyte layers using single-particle light scattering because the particles are too small for accurate measurement. We can infer, however, that the polyelectrolytes are being deposited from the zeta potential measurements.

The particles coated using the improved procedure were crystallized through vertical deposition from an ~1-wt% aqueous colloidal suspension (containing 0.1 mg/mL of PSS). Figure 97.37 shows the crystalline deposit formed by particles coated with two polyelectrolyte layers. The image shown in Fig. 97.37(a) depicts a broken section of the crystalline film, showing that it is approximately ten particle layers thick. The image shown in Fig. 97.37(b) depicts the hexagonal packing and long-range order of the crystal. There are numerous drying cracks present, but overall crystal quality is very good. The quality of the crystals formed from the two-layer-coated, 270-nm particles is very nearly the same as that for the uncoated particles (shown in Fig. 97.34).

Figures 97.38(a) and 97.38(b) show crystals of particles coated with four and six alternating polyelectrolyte layers, respectively. The particles coated with four polyelectrolyte layers produce very good crystals. There are drying cracks where the crystal has contracted, but the overall packing of the crystal is good. There are some areas where the crystal structure is disrupted. Particles coated with six polyelectrolyte layers produce noticeably poorer-quality crystals [Fig. 97.38(b)].

Figure 97.36

Zeta potential of 270-nm-diam polystyrene particles as a function of layer number during layer-by-layer deposition of PAH/PSS with improved coating procedure. The polyelectrolytes were deposited from a 1-mg/mL solution containing 1 mM of NaCl. Layer 1 is PAH (positive), layer 2 is PSS (negative), and additional layers are deposited with an alternating polyelectrolyte charge. The alternating sign of the zeta potential implies that the polyelectrolytes are adsorbing onto the particles via electrostatic attraction.

There are regions where the particles are randomly oriented, probably due to aggregation during the coating process. Since the crystal quality degrades as a function of number of layers coated, it can be inferred that some small amount of particle aggregation occurs during the coating process. Each layer applied leads to additional aggregation and further reduction in crystal quality.

The photonic band gap of the crystals was probed with reflectance spectroscopy as shown in Fig. 97.39. The peak reflectance located near 575 nm is due to the photonic band gap. The band gap causes the crystals to appear green in color. The most-prominent feature of the reflectance spectra of the samples is the decrease in band-gap intensity with an increasing number of polyelectrolyte layers coating the particles. The

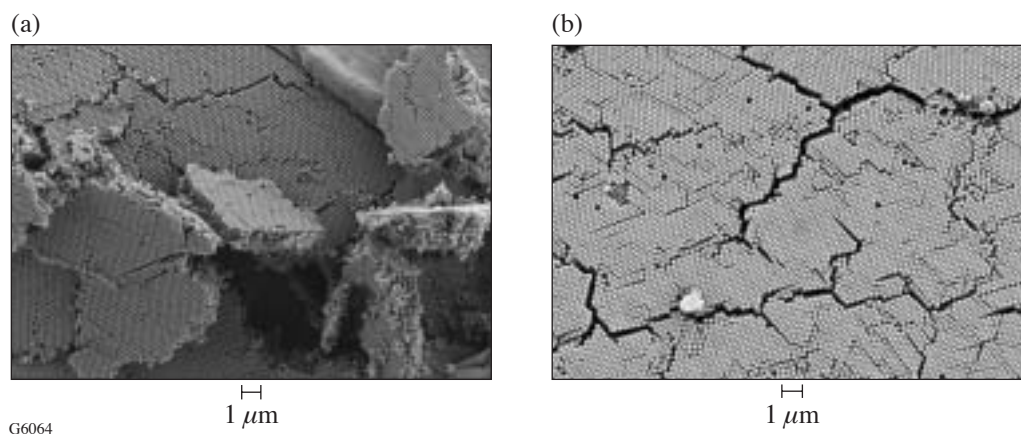


Figure 97.37

Crystals of 270-nm-diam polystyrene particles coated with two polyelectrolyte layers using the improved coating procedure. (a) Image of a broken section of the film showing the crystal thickness (1- μ m bar). (b) Surface of the crystal showing the long-range-hexagonal, close-packed structure with drying cracks visible (1- μ m bar).

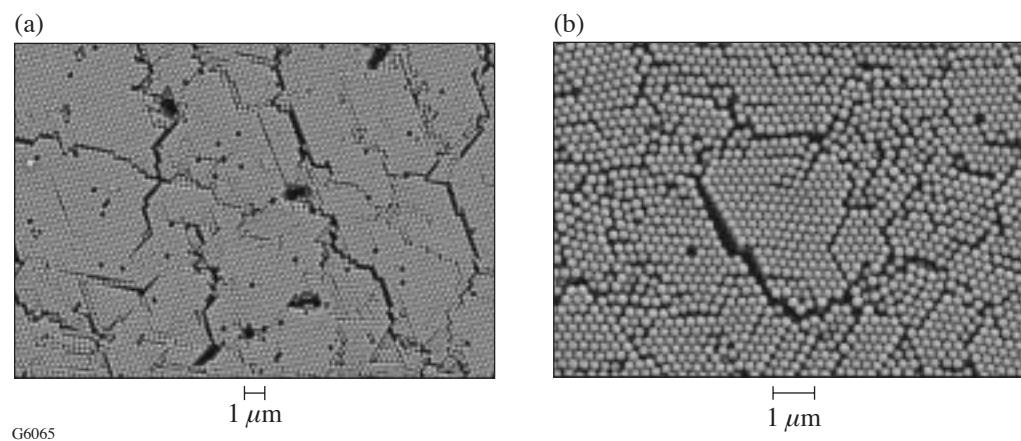


Figure 97.38

Crystals of 270-nm-diam polystyrene particles coated with (a) four alternating PAH/PSS layers (1- μ m bar) and (b) six alternating PAH/PSS layers (1- μ m bar). As the number of polyelectrolyte layers increases, the crystal quality decreases. In image (b), regions of randomly aggregated particles are visible.

intensity decreases and the width of the band gap increases due to poorer crystal quality. The optical data in Fig. 97.39 confirm the observation in Figs. 97.37 and 97.38 that crystal quality decreases with an increasing number of polyelectrolyte layers. Even with the improved coating technique, a small amount of particle aggregation occurs during each coating. Particles coated with two polyelectrolyte layers produce crystals nearly as high in quality as the uncoated particles. High-quality crystals are obtainable with up to four polyelectrolyte coatings, but poorer quality is produced with six-layer-coated particles.

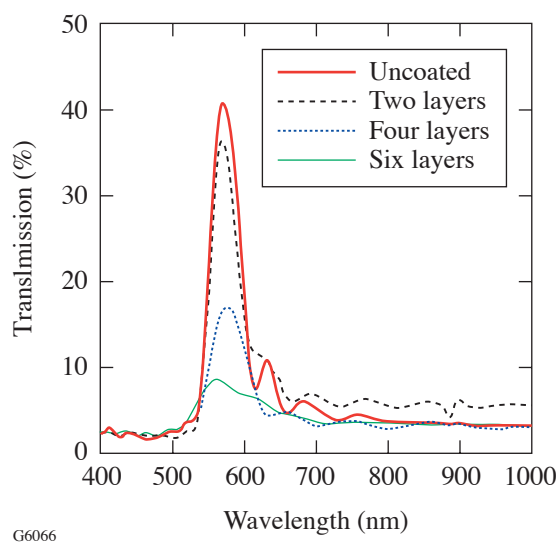


Figure 97.39 Reflectance spectra of colloidal crystals in Figs. 97.34, 97.37, and 97.38 taken at a 6° angle. The crystals have a pseudophotonic band-gap reflectance peak located at ~ 575 nm, which visually gives them a green appearance. The peak height and sharpness decrease with an increasing number of polyelectrolyte layers coating the particles because of poorer crystal quality. The decrease in crystal quality is most likely due to a small amount of particle aggregation in each coating step.

It is notable that the band gap does not significantly shift position when coated. Since the position of the band gap is related to the particle diameter, one would expect a shift to longer wavelengths as the particle diameter becomes larger due to deposition of polyelectrolytes. The band gap of the sample coated with two layers is actually slightly shifted to shorter wavelengths. It is unclear at this point why the blue shift occurs. The band gap is slightly shifted to longer wavelengths for the crystals formed with particles coated with four layers. Further coating broadens and weakens the peak so that

the shift is not discernible. It is known that salt increases the thickness of the polyelectrolyte layers during deposition. Since our improved coating process uses less salt, we expect the thickness to be small; unfortunately, we were unable to actually measure the layer thickness. The small layer thickness would cause the band gap to shift only slightly. Coupled with a blue shift, the net effect is that the band gap stays in nearly the same position. Further work is needed to fully understand the optical properties.

Conclusions and Future Directions

We have demonstrated that high-quality crystals of polyelectrolyte-coated particles may be formed by vertical deposition. The colloidal crystals display preferential reflection of light due to the pseudo band gap of the crystal. The crystal quality degrades with the number of polyelectrolyte layers coated on the particles. It is postulated that there is slight particle aggregation during the coating process that disrupts crystallization. The crystal degradation is apparent from the reduction in the maximum intensity of reflected light. Particles coated with two polyelectrolyte layers have a maximum intensity of reflectance nearly the same as the uncoated particles. The reflectance intensity decreases for particles coated with four layers, and there is almost no reflectance for particles coated with six layers. Further work is needed to completely eliminate particle aggregation during the particle-coating process.

The polyelectrolyte-coated particles offer intriguing possibilities for controlling and enhancing the optical properties of the colloidal crystals. The polyelectrolyte shells surrounding the particles have a high number of free ionic groups. A variety of optically active species may be immobilized in the shell through ion exchange. For example, ionic fluorophores may be immobilized in the polyelectrolyte shell by simply dispersing the particles in an aqueous solution of the dye.¹⁴ In addition, optically active species, including fluorescent quantum dots, may be introduced into the shells during the coating process.^{15,16} It should be possible to enhance the band gap by choosing a dye that adsorbs near the band-gap maxima. In addition, it should be possible to choose luminescent compounds that emit light at a wavelength near the photonic-band-gap maxima. It has been shown recently that lasing from colloidal crystals is possible when a dye that emits in the band-gap wavelength is incorporated into the structure.¹⁷

ACKNOWLEDGMENT

We acknowledge support from the NSF International Research Fellowship Program and the Laboratory for Laser Energetics.

REFERENCES

1. S. John, Phys. Rev. Lett. **58**, 2486 (1987).
2. E. Yablonovitch, Phys. Rev. Lett. **58**, 2059 (1987).
3. A. Blanco *et al.*, Nature **405**, 437 (2000).
4. K. M. Ho, C. T. Chan, and C. M. Soukoulis, Phys. Rev. Lett. **65**, 3152 (1990).
5. K. P. Velikov *et al.*, Science **296**, 106 (2002).
6. D. J. Norris and Y. A. Vlasov, Adv. Mater. **13**, 371 (2001).
7. Z. Liang, A. S. Susha, and F. Caruso, Adv. Mater. **14**, 1160 (2002).
8. A. Moroz, Phys. Rev. Lett. **83**, 5274 (1999).
9. F. Caruso, Adv. Mater. **13**, 11 (2001).
10. D. Wang, A. L. Rogach, and F. Caruso, Nano Lett. **2**, 857 (2002).
11. P. Jiang *et al.*, Chem. Mater. **11**, 2132 (1999).
12. Z. Z. Gu, A. Gujjishima, and O. Sato, Chem. Mater. **14**, 760 (2002).
13. D. I. Gittins and F. Caruso, J. Phys. Chem. B **105**, 6846 (2001).
14. F. Caruso *et al.*, Macromolecules **32**, 2317 (1999).
15. W. Yang *et al.*, J. Colloid Interface Sci. **234**, 356 (2001).
16. A. S. Susha *et al.*, Colloid Surf. A, Physiochem. Eng. Aspect **163**, 39 (2000).
17. M. N. Shkunov *et al.*, Adv. Funct. Mater. **12**, 21 (2002).

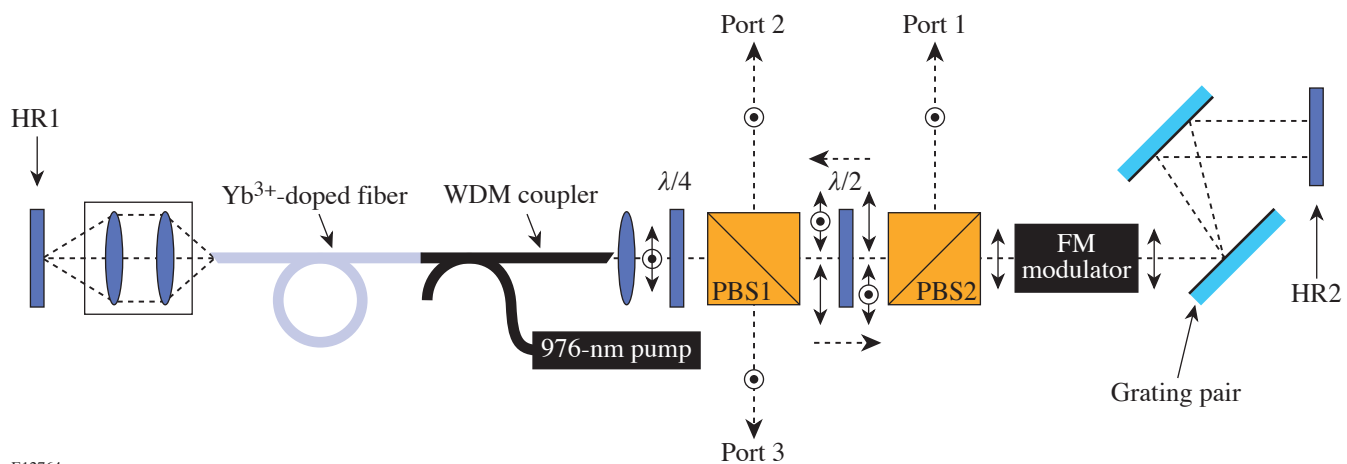
A Tunable, High-Repetition-Rate, Harmonically Mode-Locked, Ytterbium Fiber Laser

Fiber laser and amplifier development in the wavelength region near 1 μm has experienced significant progress owing to the exceptional efficiency and gain bandwidth of ytterbium-doped fibers.^{1–5} In fact, both ytterbium fiber lasers and amplifiers are becoming more attractive than their bulk counterparts due to their confined spatial mode, impressive bandwidth, good pump absorption, ease of alignment, and inherent compatibility with optical fiber. To date, however, experimental efforts regarding ytterbium fiber lasers have been directed only toward fundamental mode-locking, which typically limits pulse repetition rates below 100 MHz.^{1–5}

This article focuses on another important parameter of mode-locked lasers that has thus far attracted little attention in this wavelength regime—high repetition rate. High-repetition-rate ytterbium fiber lasers would be a useful source of ultrafast picket-fence pulse trains that have been proposed to improve the performance of fusion laser systems.⁶ In this scheme, shaped nanosecond pulses are replaced by a train of ultrafast “picket” pulses that deliver the same average power

while increasing the third-harmonic conversion efficiency. A high-repetition-rate and broadly tunable source would also be useful for synchronously pumping multi-GHz optical parametric oscillators.⁷

The laser considered in this research uses a 976-nm pumped linear cavity, shown in Fig. 97.40, similar to that reported by Lefort *et al.* in 2002.² A bulk phase modulator⁸ actively FM mode-locks the laser, enabling synchronization to an external reference frequency. Velocity matching between the optical and microwave fields in the modulator’s LiNbO₃ crystal, in conjunction with a resonant design, offers efficient phase modulation at the device’s resonance frequency ≈ 10.3 GHz. A synthesized microwave signal generator (HP model 83732B) amplified by a traveling-wave tube amplifier (Hughes model 8010H) provides up to 10 W of microwave power to the modulator. To reduce intracavity loss, the crystal facets were antireflection coated, resulting in an insertion loss of $<1\%$ at 1053 nm.



E12764

Figure 97.40

Laser cavity configuration: HR, high-reflectivity mirrors; PBS, polarizing beam splitters; WDM, 976/1050-nm wavelength division multiplexer. The double-sided arrows and the dots surrounded by circles represent the horizontal and vertical polarizations, respectively.

The laser delivers output to three different ports, as shown in Fig. 97.40. The combination of a half-wave plate ($\lambda/2$) and a polarizing beam splitter not only provides variable output coupling, yielding up to 38 mW from port 1 and up to 6.5 mW from port 2, but also selects the optimum polarization for the FM modulator and grating pair. Depolarization in the fiber section of the cavity results in 2.5 mW of leakage from port 3.

The mode-locking threshold was measured to be as low as 30 mW, but the pump laser was operated at a power of 150 mW in an effort to maximize the output power and facilitate autocorrelation measurements. All of the results presented in this article were obtained using this pump power and the output from port 1, where the laser had a slope efficiency of 32% (if we consider all three ports the slope efficiency is 40%). The cavity also incorporates a grating pair, which compensates the normal dispersion introduced by 1 m of ytterbium-doped fiber and 1.2 m of fiber associated with the 976/1050 WDM coupler.

A typical mode-locked pulse spectrum, measured with an optical spectrum analyzer (Ando model AQ6315A), reveals a bandwidth of 0.9 nm, as seen in Fig. 97.41. This spectrum is best fit by a sech^2 function shown by the dashed curve. Considering this to be the spectral shape, a 0.9-nm bandwidth (FWHM) implies a 1.3-ps (FWHM) transform-limited sech pulse. According to the simple FM mode-locking theory, an FM modulator in a purely linear dispersionless cavity should

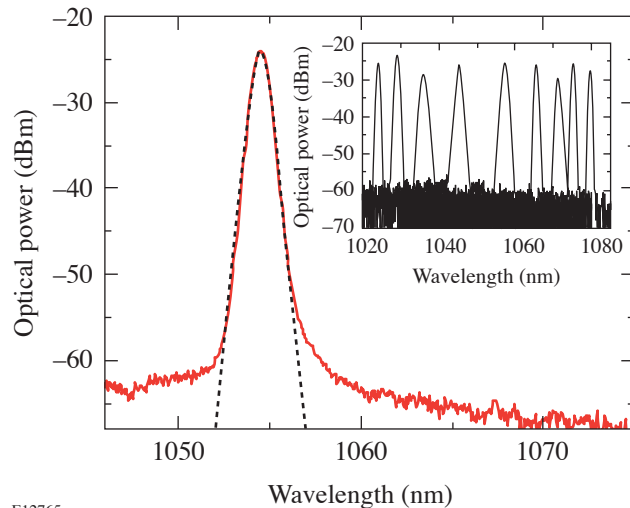


Figure 97.41
Mode-locked optical pulse spectrum and its associated sech^2 fit. The inset contains superimposed mode-locked spectra illustrating the 1025- to 1080-nm tuning range.

produce chirped Gaussian output pulses with Gaussian spectra.⁹ In light of this, our spectral measurements suggest that cavity dispersion and fiber nonlinearity play a role in shaping the laser pulses.

An interferometric autocorrelator employing two-photon absorption (TPA) in the photocathode of a photomultiplier tube was used to perform autocorrelation measurements (Fig. 97.42).¹⁰ This sensitive diagnostic was required to measure the ≤ 4 -pJ pulses resulting from the extremely high repetition rate. The autocorrelation trace was also best fit by the TPA response to a sech pulse, indicating a pulse width of 2 ps (FWHM).¹¹ Comparing the fit with the 1.3-ps pulse expected for a transform-limited field, the output pulses are found to be broadened by a factor of ≈ 1.5 due to chirp and resulting in a time-bandwidth product of 0.49.

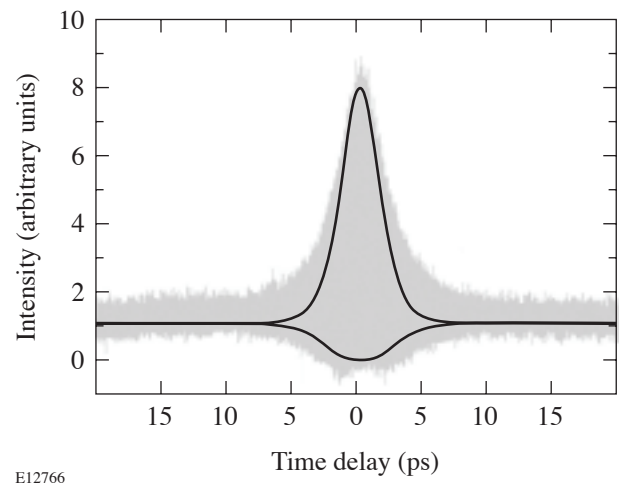


Figure 97.42
Autocorrelation results. The fit shown in this figure was obtained by using the two-photon absorption response to a 2-ps hyperbolic-secant pulse.

Mode-locked operation was achieved with central wavelengths ranging from 1022 nm to 1080 nm by inserting a razor blade in front of HR2 (not depicted in Fig. 97.40) and adjusting its position. The central wavelength also depended on the driving modulation frequency, the cavity length, and the angular position of mirror HR2. The effect of tuning on the pulse spectrum is shown in the inset of Fig. 97.41, where several different spectra in the tuning range of 1022 to 1080 nm have been superimposed on one another. The spectral shape varies little over the tuning range, although the spectral width increases as the center wavelength is decreased.

Side-mode suppression and timing jitter are two common figures of merit used to evaluate the quality of a mode-locked pulse train. These quantities are derived from the pulse-train power spectrum shown in Fig. 97.43 and obtained using a 25-GHz photodetector with a nominally flat frequency response (New Focus model 1414) and a 26.5-GHz microwave spectrum analyzer (Agilent model E4407B). As expected, the microwave spectrum shown in the inset of Fig. 97.43 is composed of peaks at the 10.31455-GHz driving frequency, its harmonics, and much weaker structures spaced by the 36.8-MHz fundamental repetition rate of the laser cavity (not visible in the figure), which are due to supermode noise.¹² A side-mode suppression of greater than 72 dB was measured with respect to the largest of these side modes. Dividing the laser's mode-locked repetition rate by its fundamental repetition rate reveals that there are 280 pulses simultaneously circulating in this cavity.

Since Fig. 97.43 shows that each peak is δ -function-like, having a FWHM narrower than the minimum resolution (1 Hz)

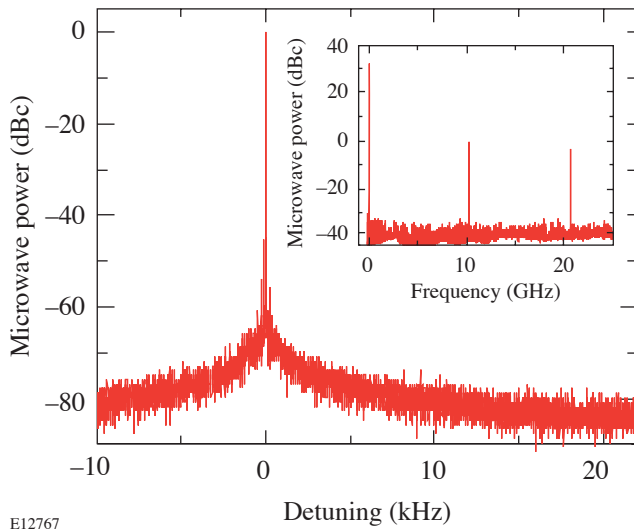


Figure 97.43

The microwave spectrum of the laser versus detuning from the 10.31455-GHz modulation frequency. The figure reveals that the signal at the modulation frequency is located 80 dBs above the noise floor. The inset shows the signal at 0 Hz, the ≈ 10.3 -GHz repetition rate, and the first harmonic located at ≈ 20.6 GHz. Note that the strength of the noise floor has increased (in the inset) due to the reduced resolution of the spectrum analyzer over the broad frequency range used.

of the spectrum analyzer, the timing jitter and pulse energy fluctuations of the output pulse train were characterized. An upper bound on rms timing jitter is related to the integrated spectral power over the offset frequency range f_l - f_h according to¹³

$$\sigma = \frac{1}{2\pi f_m} \left[2 \int_{f_l}^{f_h} L(f) df \right]^{1/2},$$

where σ is the rms timing jitter, f_m is the repetition frequency of the m^{th} harmonic around which this measurement is made, and $L(f)$ is the single-sided phase-noise spectral density detuned from f_m . Integration of the ~ 20 -GHz peak over an offset range from 10 Hz to 12 kHz yields an upper bound on rms timing jitter of 370 fs, which is only slightly larger than the 283-fs jitter measured for the microwave signal generator using the same range. Above 12 kHz, $L(f)$ was dominated by the ≈ -81 -dBc electronic noise floor (seen in Fig. 97.43 at the 20-kHz detuning) of the detector/spectrum analyzer combination, prohibiting an accurate jitter quantization over the typically quoted range (10 Hz to 10 MHz). The rms-energy fluctuations were quantified¹³ over the 10-Hz to 10-MHz range, indicating an rms fluctuation of 16.9 fJ, which corresponds to an energy fluctuation of 0.85% for the 2-pJ pulses.

In conclusion, a tunable, high-repetition-rate, mode-locked, ytterbium fiber laser has been demonstrated. The hyperbolic-secant pulse spectrum indicates that the chirp introduced by the FM modulator is interacting with the cavity dispersion and fiber nonlinearity to play a role in shaping the laser pulses. The pulse-train timing jitter was found to be primarily due to the electronics and could be reduced by using a cleaner signal generator for jitter-sensitive applications. Finally, this laser's output pulse train consisting of linearly polarized, 2-ps chirped pulses could produce up to 38 mW of average power, making it suitable for many future applications.

ACKNOWLEDGMENT

The authors thank Y. Deng for his assistance with the autocorrelation measurements, W. Bittle for his advice on electronics issues, and W. Knox for his support of this work. This work was supported by the U.S. Department of Energy Office of Inertial Confinement Fusion under Cooperative Agreement No. DE-FC03-92SF19460, the University of Rochester, and the New York State Energy Research and Development Authority. The support of DOE does not constitute an endorsement by DOE of the views expressed in this article.

REFERENCES

1. V. Cautaerts *et al.*, *Opt. Lett.* **22**, 316 (1997).
2. L. Lefort *et al.*, *Opt. Lett.* **27**, 291 (2002).
3. H. Lim, F. Ö. Ilday, and F. W. Wise, *Opt. Lett.* **28**, 660 (2003).
4. O. G. Okhotnikov *et al.*, *Opt. Lett.* **28**, 1522 (2003).
5. A. Liem *et al.*, *Appl. Phys. B* **71**, 889 (2000).
6. J. E. Rothenberg, *Appl. Opt.* **39**, 6931 (2000).
7. S. Lecomte *et al.*, *Opt. Lett.* **27**, 1714 (2002).
8. J. D. Zuegel and D. W. Jacobs-Perkins, "An Efficient, High-Frequency Bulk Phase Modulator," to be published in *Applied Optics*.
9. D. Kuizenga and A. Siegman, *IEEE J. Quantum Electron.* **6**, 694 (1970).
10. J. M. Roth, T. E. Murphy, and C. Xu, *Opt. Lett.* **27**, 2076 (2002).
11. K. Mogi, K. Naganuma, and H. Yamada, *Jpn. J. Appl. Phys. 1, Regul. Pap. Short Notes Rev. Pap.* **27**, 2078 (1988).
12. F. Rana *et al.*, *J. Opt. Soc. Am. B* **19**, 2609 (2002).
13. D. von der Linde, *Appl. Phys. B* **39**, 201 (1986).

Deterministic Microgrinding, Lapping, and Polishing of Glass-Ceramics

Introduction

Glass-ceramics are attractive structural materials due to their good mechanical properties, chemical stability at higher temperatures, and tailored microstructures via appropriate heat treatments. In the cold working of glass-ceramics, several options are available: loose-abrasive grinding (lapping, at fixed nominal pressure) or deterministic microgrinding (at fixed nominal infeed, with bound-abrasive tools), both of which primarily remove material by microcracking. These manufacturing operations are usually followed by polishing to remove the residual stresses or damage left from the grinding operations.

The goal of the work described in this article is twofold: to determine which properties of glass-ceramics are responsible for material removal and the quality of the resulting surface (roughness, residual stresses induced by grinding), and to compare loose-abrasive grinding with deterministic microgrinding.

Measurements

Five novel glass-ceramic materials (labeled GC1-GC5) were provided by Corning, Inc. The surface roughness of the as-received samples was in the range of 4 to 8 μm (peak-to-valley).

1. Elastic Properties and Microindentation Measurements

Longitudinal and shear wave speeds were first measured and then converted to Young's and shear moduli. Young's modulus was also independently measured from the load-displacement curve in 4-pt bending tests. Modulus of rupture was measured in 4-pt bend tests for as-received samples, as well as for samples in which controlled flaws were introduced on the tension side by Vickers indentation. Knoop hardness was measured at loads of 50 to 200 gf. Vickers hardness was measured at loads from 10 to 1000 gf. Between five to ten indents at each load were performed (15-s dwell time). All materials were measured in air.

For the fracture toughness measurements, the length c of the cracks emanating from the Vickers indentation corners

was measured optically. We used indentation¹—the approach of Evans²—to extract the fracture toughness K_c from the measured indentation crack size. In our glass-ceramics tests, the range of indentation crack size to indent diagonal $c/(D/2)$ was from 2 to 3 and thus covered by the Evans approach. Ponton and Rawlings^{3,4} published an exhaustive analysis comparing the prediction of the fracture toughness by many different indentation models to the fracture toughness measured by bulk methods. They examined many ceramics (zirconias and aluminas), as well as many glass-ceramics, concluding that several models gave good agreement between the bulk and indentation fracture toughness measurements. The Evans model² was one such model. Our work on the fracture toughness of optical glasses⁵ also has shown that the Evans model provides a good prediction of fracture toughness.

2. Chemical Susceptibility Measurements

The alkali resistance of the glass-ceramics was tested by immersing two test pieces in a boiling aqueous solution of equal parts Na_2CO_3 and NaOH for 3 h. The resulting mass loss, measured in an analytical balance, indicates the material's chemical susceptibility or alkali resistance. Table 97.II summarizes the measured micromechanical and chemical properties of the glass-ceramic materials.

3. Deterministic Microgrinding Measurements

Deterministic microgrinding is a fixed-infeed-rate material removal process utilizing computer-numerically-controlled (CNC) machining platforms. We sequentially used three thin-walled diamond-bound-abrasive (metal bond 75N, medium hardness) cup wheel tools on the Opticam SX CNC machining platform.⁶ The tools were dressed before grinding each new type of material. To examine the effect of abrasive size in deterministic microgrinding, we used the three tools on glass-ceramics samples in the form of thin disks (aspect ratio about 30/1): first, a rough tool (average abrasive size of 70 μm) at an infeed rate of 100 $\mu\text{m}/\text{min}$, then a medium tool (abrasive size 10 to 20 μm) at an infeed rate of 50 $\mu\text{m}/\text{min}$, and finally a fine tool (abrasive size 2 to 4 μm) at an infeed rate of 10 $\mu\text{m}/\text{min}$. The tool rotation rate was 5000 rpm, and the work rotation rate

was 150 rpm. The tool rotation rate and diameter correspond to a surface speed of about 14.1 m/s. Three to five samples were tested at each setting. Following grinding with each tool, the surface roughness was measured with a white-light interferometer (Model NewView 1000, Zygo Corp., Middlefield, CT) and so was the power (sag), induced by the grinding process.

4. Loose-Abrasive Lapping and Polishing
Removal Rate Measurements

Lapping and polishing experiments used thin glass-ceramic disks of approximately 2.2-mm thickness and 62-mm diameter. The as-received saw-cut specimens were first lapped on a Strasbaugh platform with 22- μm alumina abrasives (cast-iron plate and aqueous slurry), then with 7- μm alumina abrasives (same slurry composition), and finally polished with 1- μm alumina abrasives (aqueous slurry, new polyurethane lap used for each material). The initial condition for each process was the final surface from the previous step. In the

lapping and polishing experiments, the pressure was maintained at 10 to 14 kPa and the relative speed at 1.22 m/s. Surface roughness was measured at the center and near the edge of the circular surfaces.

5. Grinding-Induced Surface Residual Stress Measurements

Surface residual stresses induced by the lapping process (see the previous section), i.e., the Twyman effect for glass-ceramics, were measured on flat disks of samples (aspect ratio of about 30/1) whose two sides (S1 and S2) were first polished to approximately one-wave flatness. Subsequently, one surface (surface S1) was lapped by 22- μm Al_2O_3 abrasives for about 2 to 3 min, then by 7- μm Al_2O_3 abrasives for about 30 min, and finally polished by 1- μm Al_2O_3 abrasives for about 20 to 45 min. The slurry and processing conditions were as described in the previous section. During this process, the other surface (S2) remained polished, and its power (sag) was measured with the white-light interferometer.

Table 97.II: Summary of the measurements of the mechanical and chemical properties of glass-ceramics.

	GC1	GC2	GC3	GC4	GC5
Thermoelastic properties					
Density ρ (kg m^{-3})	3.18	2.93	2.98	2.99	2.98
Thermal expansion coefficient α ($10^{-6} \text{ }^\circ\text{C}^{-1}$)	8.6	6.02	–	–	4.21
Young's modulus E (GPa), $\pm 5\%$	130	130	123	138	113
Shear modulus G (GPa), $\pm 5\%$	52.2	53.4	48.9	56.8	46.0
Poisson ratio ν	0.242	0.219	0.255	0.217	0.229
Modulus of rupture (MPa), $\pm 10\%$					
As-received	178	162	145	159	124
With Vickers flaw @ $P = 1$ kgf	138	120	80	118	76
Microindentation hardness					
Knoop hardness @ 0.2 kgf (GPa), $\pm 5\%$	9.3	10.0	9.4	9.9	8.7
Vickers hardness @ 1 kgf (GPa), $\pm 10\%$	9.5	9.4	9.3	10.0	8.2
Microindentation cracking					
Crack size $2c$ (μm) @ 500 gf	83.6	70.6	81.7	73.0	80.8
Indent. fracture toughness K_c ($\text{MPa } \sqrt{\text{m}}$), $\pm 10\%$	1.41	1.75	1.53	1.63	1.55
Chemical susceptibility (alkali attack)					
Mass loss per unit area (mg/cm^2)	162 \pm 20	43 \pm 12	41.3 \pm 3.3	33 \pm 2.3	114 \pm 0.3

Results

For the deterministic microgrinding experiments (fixed infeed rate), Fig. 97.44 shows the correlation of surface roughness and chemical susceptibility (alkali resistance). The results generally indicate that materials with higher chemical susceptibility also lead to higher surface roughness. Figure 97.45 shows the correlation of surface microroughness with abrasive size, indicating that, for a given material, finer abrasives lead to lower surface roughness. Figure 97.46 shows the dependence of the grinding-induced surface residual force per unit length on the Vickers indentation crack size.

For the loose-abrasive lapping experiments, Fig. 97.47 shows the dependence of the material removal rate on the material figure of merit $E^{5/4}/[K_c \text{ Hv}]$, Fig. 97.48 the dependence of surface microroughness on hardness, and Fig. 97.49 the dependence of surface roughness on chemical susceptibility.

For the polishing experiments, Fig. 97.50 shows the dependence of the polishing rate on Vickers hardness and Fig. 97.51 the polishing rate versus the material figure of merit $E^{5/4}/[K_c \text{ Hv}]$. Figure 97.52 shows the dependence of the lapping-induced surface-grinding force on microindentation crack size.

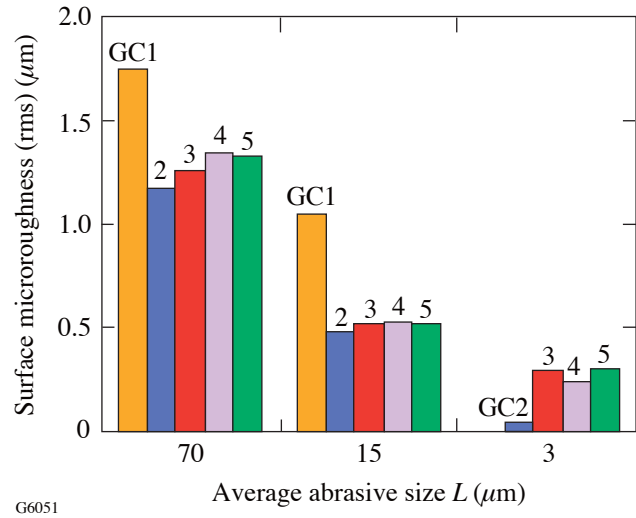


Figure 97.45
Dependence of surface microroughness on abrasive size in deterministic microgrinding.

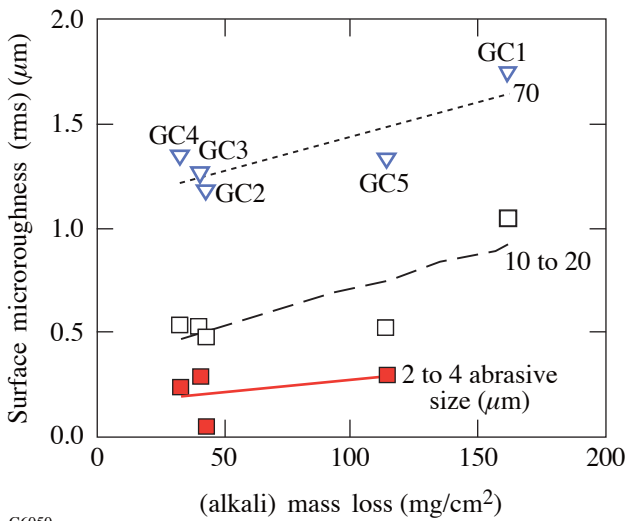


Figure 97.44
Dependence of surface roughness induced by deterministic microgrinding on chemical susceptibility, as measured by the mass loss under alkali attack.

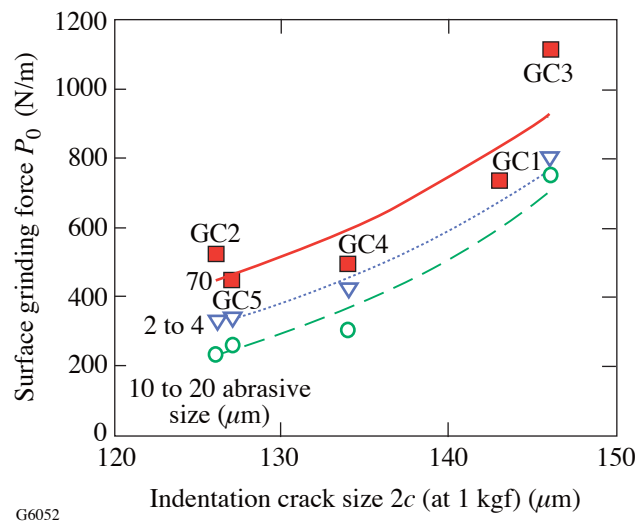
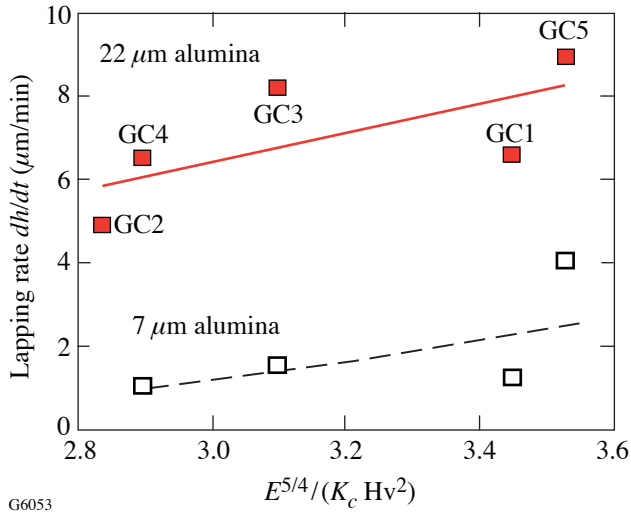
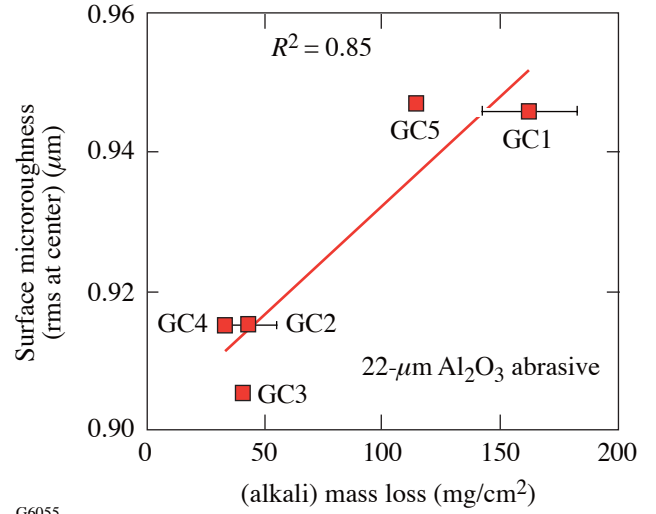


Figure 97.46
Dependence of grinding-induced force P_0 on indentation crack size (at 1 kgf).



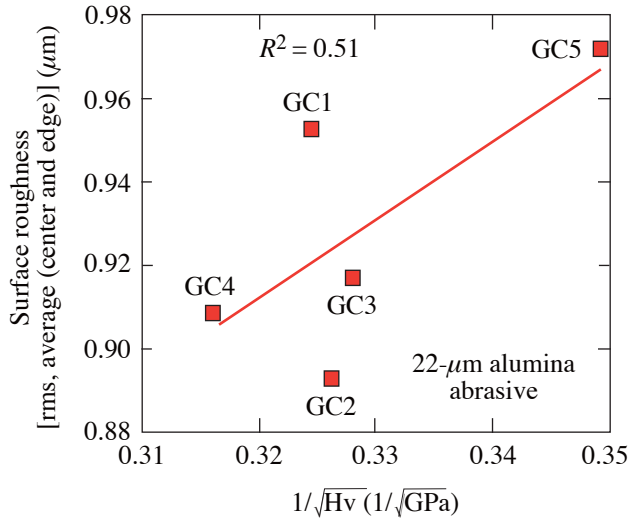
G6053

Figure 97.47
Dependence of lapping rate on mechanical properties. Fracture toughness K_c (MPa m^{1/2}) and Vickers hardness Hv (GPa, at 1 kgf).



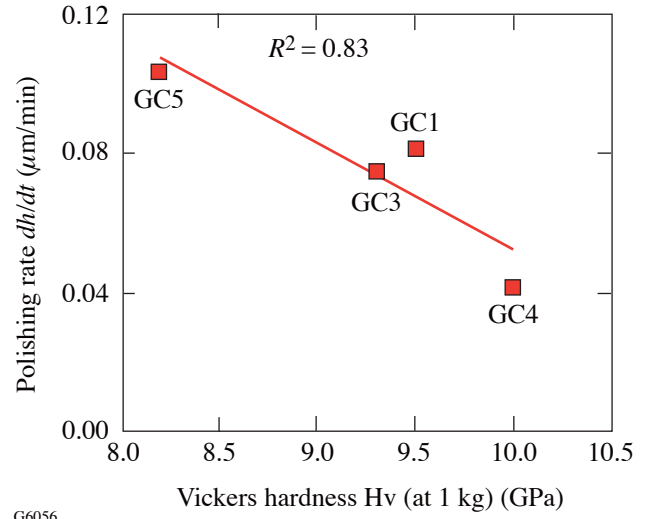
G6055

Figure 97.49
Dependence on chemical susceptibility of surface roughness (measured in center of the plate) induced by lapping with 22- μ m Al₂O₃ abrasives.



G6054

Figure 97.48
Dependence of surface roughness induced by lapping with 22 μ m Al₂O₃ on material hardness.



G6056

Figure 97.50
Dependence of polishing rate on Vickers hardness (at 1 kgf).

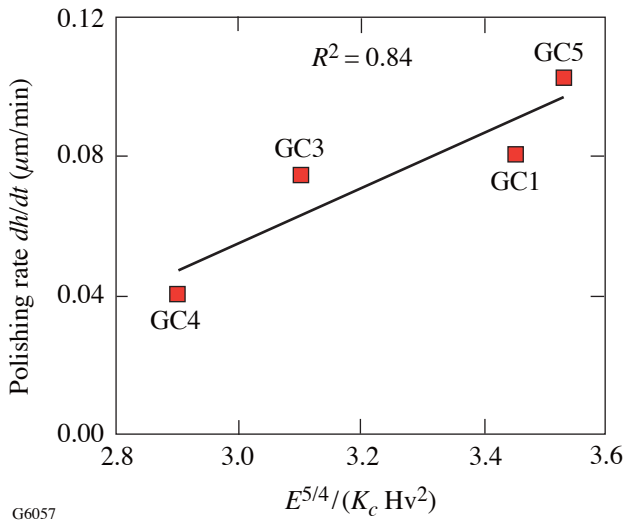


Figure 97.51
Dependence of polishing rate on mechanical properties: fracture toughness K_c (MPa $m^{1/2}$) and Vickers hardness H_v (GPa, at 1 kgf) from microindentation.

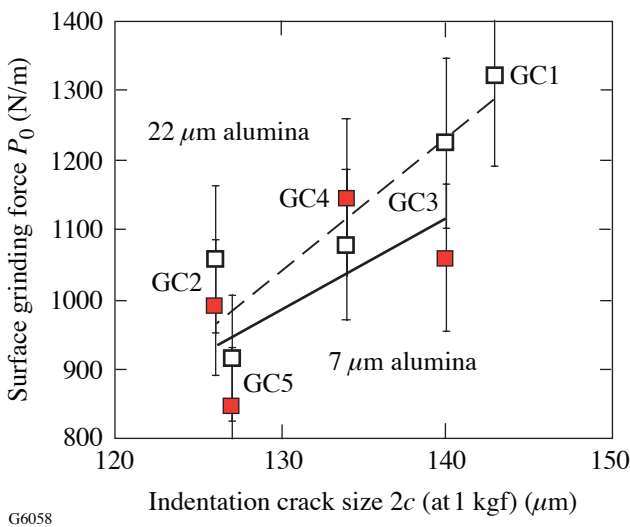


Figure 97.52
Dependence on microindentation crack size (at 1 kgf) of lapping-induced surface grinding force P_0 for lapping with 22- μm and 7- μm Al_2O_3 abrasives. The lapped surface is S1 (originally polished). P_0 is proportional to the change in power, measured on the polished surface S2, from the initial power (S1 polished) to the value after S1 is lapped.

Discussion

Some of our results are as intuitively expected. For example, Figs. 97.44 and 97.49 indicate that higher chemical susceptibility leads to higher surface roughness, both under deterministic microgrinding and under loose-abrasive lapping. Similarly, Fig. 97.45 indicates that larger abrasives lead to higher surface roughness. However, the dependence of grinding-induced surface residual force on abrasive size is not entirely obvious.

It is well known that grinding of brittle surfaces with loose or bound abrasives induces a state of residual compression on the ground surface. This phenomenon is often referred to as the Twyman effect.⁷ The measured power (sag) of the surface is an indication of the extent of the residual force per unit of length along the edge of the ground surface. In the Twyman effect, a thin brittle disk is ground on one side, without altering the other side. As a result of grinding, the ground side is in a state of compressive stress and becomes convex, whereas the other side (on which the power is measured) is concave. The measured power Δh (sag of the thin plate) was converted to an equivalent force P_0 per unit length along the circumference of the ground edge, as described in Ref. 7:

$$P_0 = \frac{4E}{3(1-\nu)} \Delta h \left(\frac{t}{D} \right)^2, \quad (1)$$

where E is the Young's modulus, ν the Poisson ratio, t the plate thickness, and D the plate diameter. The computed force P_0 is shown in Fig. 97.46 for deterministic microgrinding and in Fig. 97.52 for the loose-abrasive lapping experiments.

The results in Fig. 97.46 show that the surface grinding force does not necessarily diminish as the size of the abrasive gets smaller. Rather, for deterministic microgrinding, the intermediate abrasive (10 to 20 μm) gives the lowest surface grinding force. This result may be a consequence of the onset of ductile grinding, i.e., suppression of lateral cracking as the dominant material-removal mechanism in favor of plastic scratching. Ductile grinding is known to lead to high surface grinding forces.⁸

The correlation, reported in Fig. 97.46, between grinding-induced surface force P_0 and indentation crack size $2c$ was first reported for optical glasses by Lambropoulos *et al.*,⁷ whose results show that the same correlation holds also for glass-ceramics.

Figure 97.47 shows the lapping material removal rate versus the combination of mechanical properties, which was used previously by Lambropoulos *et al.*⁹ in optical glasses, extending the work by Buijs and Korpel-Van Houten.^{10,11} Thus, it is concluded that, in lapping of glass-ceramics,

$$\frac{dh}{dt} \sim \frac{E^{5/4}}{K_c H^2}, \quad (2)$$

where E is Young's modulus, K_c is fracture toughness, and H is the hardness. This correlation results from using a lateral crack model as the basis for the material removal mechanism.

Figure 97.48 shows the dependence of the surface roughness of the 22- μm alumina-lapped surface on the glass-ceramic hardness. As in optical glasses,⁸

$$\text{surface roughness} \sim \frac{1}{\sqrt{H}}. \quad (3)$$

The results for polishing material removal rate show that increasing hardness generally leads to a diminishing removal rate, an expected result (see Fig. 97.50). Figure 97.51 shows a new result, however, instances of which have been reported by Lambropoulos *et al.*^{12,13} for polishing of optical glasses: The polishing rate has the same dependence on material properties combination $E^{5/4}/K_c H_v$ as the lapping rate (Fig. 97.47). This result is not unexpected from a fundamental point of view: since in any material removal process atomic bonds must be broken among surface atoms, a property characterizing such bond strength (for example, fracture toughness) is expected to influence the polishing removal rate.

Our measurements on the deterministic microgrinding and lapping of glass-ceramics also allow us to compare these two processes in terms of the material removal rate and quality (surface roughness, residual stresses) of the resulting surface. Table 97.III summarizes the data for the samples studied in this report. Deterministic microgrinding maintains a faster removal rate than lapping (over the range of lapping pressures and relative speeds used), while for comparable abrasive sizes the surface roughness is lower than that for lapping, and the grinding-induced surface residual forces are significantly reduced as compared to lapping.

Table 97.III: Comparison of deterministic microgrinding and loose-abrasive grinding (lapping) for the cold working of glass-ceramic materials (L is the nominal abrasive size used). For deterministic microgrinding the abrasives are diamonds embedded in a metal bond. For lapping and polishing the abrasives are alumina.

	Surface Removal Rate ($\mu\text{m}/\text{min}$)	rms Surface Roughness (μm)	Surface Residual Force (N/m)
Deterministic microgrinding (fixed infeed)			
$L = 70 \mu\text{m}$	100	1.2–1.7	400–1100
$L = 15 \mu\text{m}$	50	0.5–1	200–700
$L = 2 \text{ to } 4 \mu\text{m}$	10	0.05–0.3	300–800
Lapping (fixed pressure)			
$L = 22 \mu\text{m}$	5–9	0.9–1	900–1300
$L = 7 \mu\text{m}$	1–4	0.7–0.8	800–1200
Polishing (fixed pressure)			
$L = 1 \mu\text{m}$	0.04–0.1	0.01–0.1	—

In this article mechanical and chemical properties of glass-ceramics and their response under deterministic or loose abrasive grinding conditions have been correlated. The quality of the resulting surface in terms of the material removal rate, the surface microroughness, and the surface residual stresses induced by microgrinding have been characterized. Neither the effects of material grain size and abrasive grain size nor the correlation of “feeds and speeds” have been examined since these alter the rate at which the tool penetrates into the work surface. In addition, the issue of subsurface damage and that of the deepest flaw induced by microgrinding have not been addressed. These issues should be studied in the context of the mechanical strength of the glass-ceramic components, especially in relation to applied thermal or mechanical forces acting on these components after grinding.

Conclusions

The microgrinding and polishing behavior of five novel glass-ceramics have been studied. The mechanical properties of the glass-ceramics, as well as their material removal rate and quality of the resulting surface, have been measured for deterministic microgrinding (fixed infeed rate; metal bond diamond cup wheel on a CNC machining platform; embedded diamond abrasives of 70 μm , 15 μm , and 3 μm in size), loose-abrasive lapping (fixed nominal pressure, 22 μm and 7 μm Al_2O_3 loose abrasives), and polishing (fixed nominal pressure, 1 μm Al_2O_3 abrasives). The quality of the worked surface was characterized in terms of the grinding-induced surface microroughness and the grinding-induced surface residual force.

Findings on deterministic microgrinding of glass-ceramics under fixed infeed rate include the following:

1. Workpiece surface microroughness scales linearly with chemical susceptibility of the glass-ceramics under alkali attack conditions. Higher mass loss under alkali attack generally leads to higher surface roughness in deterministic microgrinding and higher tool-wear rate.
2. Smaller bound abrasives lead to lower surface microroughness.
3. Intermediate bound abrasives (10 to 20 μm) lead to the lowest grinding-induced surface residual compressive force. Very large or very small bound abrasives lead to higher surface residual forces.
4. The grinding-induced surface residual compressive force increases with indentation-produced surface cracks; thus, microindentation may be used to predict surface-grinding force.

Findings on the loose-abrasive grinding and polishing of glass-ceramics under fixed nominal pressure include the following:

1. The lapping removal rate increases with $E^{5/4}/K_c \text{ Hv}$, as in optical glasses.
2. The surface roughness for 22- μm abrasives increases with $1/\sqrt{H}$, as in optical glasses.
3. The surface roughness for 22- μm abrasives increases with chemical susceptibility to alkali attack, as it did for deterministic microgrinding.
4. The polishing removal rate decreases with increasing hardness H , and increases with increasing $E^{5/4}/K_c \text{ Hv}$. This result identifies fundamental similarities between the lapping and polishing material removal mechanisms.
5. The grinding-induced surface residual compressive force is an increasing function of indentation-produced surface cracks; thus, microindentation may be used to predict surface-grinding force.

In comparing deterministic microgrinding with loose-abrasive microgrinding, it was found that deterministic microgrinding maintains a faster removal rate than lapping, while for comparable abrasive sizes, the surface roughness induced by deterministic microgrinding is lower than that for lapping, while the grinding-induced surface residual forces are significantly reduced.

ACKNOWLEDGMENT

The authors acknowledge technical assistance in property measurements (Prof. S. Gracwski for the NDE measurements; Prof. S. Burns and Dr. F. Dahmani for MOR; and Mr. D. Pomonti and Dr. Fang for the indentation measurements) and the grinding experiments (Dr. Y.-Y. Zhou), and also acknowledge insights on microstructural observations provided by Prof. Paul Funkenbusch.

REFERENCES

1. A. R. Boccaccini, *J. Mater. Sci. Lett.* **15**, 1119 (1996).
2. A. G. Evans, in *Fracture Mechanics Applied to Brittle Materials*, edited by S. W. Freiman (American Society for Testing and Materials, Philadelphia, 1979), Vol. ASTM STP 678, Part 2, pp. 112–135.
3. C. B. Ponton and R. D. Rawlings, *Mater. Sci. Technol.* **5**, 865 (1989).
4. *ibid.*, *Mater. Sci. Technol.* **5**, 961 (1989).
5. J. C. Lambropoulos, T. Fang, P. D. Funkenbusch, S. D. Jacobs, M. J. Cumbo, and D. Golini, *Appl. Opt.* **35**, 4448 (1996).

6. H. M. Pollicove and D. T. Moore, in *Optical Fabrication and Testing Workshop*, Vol. 24, 1992 Technical Digest Series (Optical Society of America, Washington, DC, 1992), pp. 44–47.
7. J. C. Lambropoulos, S. Xu, T. Fang, and D. Golini, *Appl. Opt.* **35**, 5704 (1996).
8. D. Golini and S. D. Jacobs, *Appl. Opt.* **30**, 2761 (1991).
9. J. C. Lambropoulos, S. Xu, and T. Fang, *Appl. Opt.* **36**, 1501 (1997).
10. M. Buijs and K. Korpel-van Houten, *J. Mater. Sci.* **28**, 3014 (1993).
11. *ibid.*, *Wear* **166**, 237 (1993).
12. J. C. Lambropoulos, in *Optical Fabrication and Testing Workshop*, Vol. 7, 1996 OSA Technical Digest Series (Optical Society of America, Washington, DC, 1996), pp. 88–91.
13. J. C. Lambropoulos, S. D. Jacobs, and J. Ruckman, in *Finishing of Advanced Ceramics and Glasses*, edited by R. Sabia, V. A. Greenhut, and C. G. Pantano, Ceramic Transactions, Vol. 102 (The American Ceramic Society, Westerville, OH, 1999), pp. 113–128.

Publications and Conference Presentations

Publications

- A. Agarwal, S. Banerjee, D. F. Grosz, A. P. K ung, D. N. Maywar, and T. H. Wood, "Ultralong-Haul Transmission of 40-Gb/s RZ-DPSK in a 10/40 G Hybrid System Over 2500 km of NZ-DSF," *IEEE Photonics Technol. Lett.* **15**, 1779 (2003).
- K. Anderson and R. Betti, "Theory of Laser-Induced Adiabatic Shaping in Inertial Fusion Implosions: The Decaying Shock," *Phys. Plasmas* **10**, 4448 (2003).
- Y. Geng, A. C. A. Chen, J. J. Ou, S. H. Chen, K. Klubek, K. M. Vaeth, and C. W. Tang, "Monodisperse Glassy-Nematic Conjugated Oligomers with Chemically Tunable Polarized Light Emission," *Chem. Mater.* **15**, 4352 (2003).
- Y. Geng, A. Trajkovska, S. W. Culligan, J. J. Ou, H. M. P. Chen, D. Katsis, and S. H. Chen, "Origin of Strong Chiroptical Activities in Films of Nonafluorenes with a Varying Extent of Pendant Chirality," *J. Am. Chem. Soc.* **125**, 14,032 (2003).
- O. V. Gotchev, L. J. Hayes, P. A. Jaanimagi, J. P. Knauer, F. J. Marshall, and D. D. Meyerhofer, "Large-Grazing-Angle, Multi-Image Kirkpatrick-Baez Microscope as the Front End to a High-Resolution Streak Camera for OMEGA," *Rev. Sci. Instrum.* **74**, 5065 (2003).
- M. J. Guardalben, J. Keegan, L. J. Waxer, V. Bagnoud, I. A. Begishev, J. Puth, and J. D. Zuegel, "Design of a Highly Stable, High-Conversion-Efficiency, Optical Parametric Chirped-Pulse Amplification System with Good Beam Quality," *Opt. Express* **11**, 2511 (2003).
- J. Leuthold, R. Ryf, D. N. Maywar, S. Cabot, J. Jaques, and S. S. Patel, "Nonblocking All-Optical Cross Connect Based on Regenerative All-Optical Wavelength Converter in a Transparent Demonstration Over 42 Nodes and 16800 km," *J. Lightwave Technol.* **21**, 2863 (2003).
- X. Z. Lin, X. Teng, and H. Yang, "Direct Synthesis of Narrowly Dispersed Silver Nanoparticles Using a Single-Source Precursor," *Langmuir* **19**, 10,081 (2003).
- J. D. Lindl, B. A. Hammel, B. G. Logan, D. D. Meyerhofer, S. A. Payne, and J. D. Sethian, "The US Inertial Confinement Fusion (ICF) Ignition Programme and the Inertial Fusion Energy (IFE) Programme," *Plasma Phys. Control. Fusion* **45**, A217 (2003).
- S. G. Lukishova, A. W. Schmid, A. J. McNamara, R. W. Boyd, and C. R. Stroud, Jr., "Room-Temperature Single-Photon Source: Single-Dye Molecule Fluorescence in Liquid Crystal Host," *IEEE J. Sel. Top. Quantum Electron.* **9**, 1512 (2003).
- K. L. Marshall, B. Klehn, B. Watson, and D. W. Griffin, "Recent Advances in the Development of Phase-Shifting Liquid Crystal Interferometers for Visible and Near-IR Applications," in *Advanced Characterization Techniques for Optics, Semiconductors, and Nanotechnologies*, edited by A. Duparr  and B. Singh (SPIE, Bellingham, WA, 2003), Vol. 5188, pp. 48–60.
- K. L. Marshall, B. Schudel, and I. A. Lippa, "Transition Metal Dithiolene Complexes as Near-IR Dyes for Liquid Crystal Device Applications," in *Liquid Crystals VII*, edited by I.-C. Khoo (SPIE, Bellingham, WA, 2003), Vol. 5213, pp. 201–212.
- R. Narayan, I. V. Igumenshchev, and M. A. Abramowicz, "Magnetically Arrested Disk: An Energetically Efficient Accretion Flow," *Publ. Astron. Soc. Jpn.* **55**, L69 (2003).
- X. Teng and H. Yang, "Synthesis of Face-Centered Tetragonal FePt Nanoparticles and Granular Films from Pt@Fe₂O₃ Core-Shell Nanoparticles," *J. Am. Chem. Soc.* **125**, 14,559 (2003).

Y. Wang, J. F. Wong, X. Teng, X. Z. Lin, and H. Yang, “‘Pulling’ Nanoparticles into Water: Phase Transfer of Oleic Acid Stabilized Monodisperse Nanoparticles into Aqueous Solutions of α -Cyclodextrin,” *Nano Lett.* **3**, 1555 (2003).

Y. Xu, M. Khafizov, L. Satrapinsky, P. Kúř, A. Plecenik, and R. Sobolewski, “Time-Resolved Photoexcitation of the Superconducting Two-Gap State in MgB_2 Thin Films,” *Phys. Rev. Lett.* **91**, 197004 (2003).

J. Zhang, N. Boiadjeva, G. Chulkova, H. Deslandes, G. N. Gol’tsman, A. Korneev, P. Kouminov, M. Leibowitz, W. Lo, R. Malinsky, O. Okunev, A. Pearlman, W. Slys, K. Smirnov, C. Tsao, A. Verevkin, V. Voronov, K. Wilsher, and R. Sobolewski, “Noninvasive CMOS Circuit Testing with NbN Superconducting Single-Photon Detectors,” *Electron. Lett.* **39**, 1086 (2003).

Forthcoming Publications

E. L. Alfonso, R. Q. Gram, and D. R. Harding, “Modeling Temperature and Pressure Gradients During Cooling of Thin-Walled Cryogenic Targets,” to be published in *Fusion Science and Technology*.

K. Anderson and R. Betti, “Laser-Induced Adiabatic Shaping by Relaxation in Inertial Fusion Implosions,” to be published in *Physics of Plasmas*.

V. Bagnoud and J. D. Zuegel, “Independent Phase and Amplitude Control of a Laser Beam Using a Single-Phase-Only Spatial Light Modulator,” to be published in *Optics Letters*.

T. J. B. Collins, J. P. Knauer, R. Betti, T. R. Boehly, J. A. Delettrez, V. N. Goncharov, D. D. Meyerhofer, P. W. McKenty, S. Skupsky, and R. P. J. Town, “Reduction of the Ablative Rayleigh–Taylor Growth Rate with Gaussian Picket Pulses,” to be published in *Physics of Plasmas*.

C. Dorrer and D. N. Maywar, “RF Spectrum Analysis of Optical Signals Using Nonlinear Optics,” to be published in the *Journal of Lightwave Technology* (invited).

L. Guazzotto, R. Betti, J. Manickam, and S. Kaye, “Numerical Study of Tokamak Equilibria with Arbitrary Flow,” to be published in *Physics of Plasmas*.

T. J. Kessler, J. Bunkenburg, H. Huang, A. Kozlov, and D. D. Meyerhofer, “Coherent Addition of Multiple Gratings for High Energy Chirped-Pulse Amplified Lasers,” to be published in *Optics Letters*.

A. K. Knight, F.-Y. Tsai, M. J. Bonino, and D. R. Harding, “Suitability of Different Polyimide Capsule Materials for Use

as ICF Targets,” to be published in *Fusion Science and Technology*.

T. I. Lakoba, C. Dorrer, and D. N. Maywar, “Polarization-Mode Dispersion of a Circulating Loop,” to be published in the *Journal of the Optical Society of America B*.

J. Leuthold, R. Ryf, D. N. Maywar, S. Cabot, and J. Jacques, “Demonstration of a Nonblocking Cross Connect Concept Based on Regenerative All-Optical Wavelength Converter over 42 Nodes and 16800 km,” to be published in *IEEE Photonics Technology Letters*.

J. R. Marcianti and D. H. Raguin, “A New Class of High-Efficiency, High-Dispersion Diffraction Gratings Based on Total Internal Reflection,” to be published in *Optics Letters*.

F. J. Marshall, J. A. Delettrez, R. Epstein, R. Forties, R. L. Keck, J. H. Kelly, P. W. McKenty, S. P. Regan, and L. J. Waxer, “Direct-Drive-Implosion Experiments with Enhanced Fluence Balance on OMEGA,” to be published in *Physics of Plasmas*.

R. L. McCrory, D. D. Meyerhofer, R. Betti, T. R. Boehly, R. S. Craxton, T. J. B. Collins, J. A. Delettrez, R. Epstein, V. Yu. Glebov, V. N. Goncharov, D. R. Harding, R. L. Keck, J. H. Kelly, J. P. Knauer, S. J. Loucks, L. Lund, J. A. Marozas, P. W. McKenty, F. J. Marshall, S. F. B. Morse, P. B. Radha, S. P. Regan, S. Roberts, W. Seka, S. Skupsky, V. A. Smalyuk, C. Sorce, C. Stoeckl, J. M. Soures, R. P. J. Town, B. Yaakobi, J. A. Frenje, C. K. Li, R. D. Petrasso, F. H. Séguin, K. A. Fletcher, S. Padalino, C. Freeman, and T. C. Sangster, “Direct-Drive Inertial Confinement Fusion Research at the Laboratory for Laser Energetics,” to be published in the proceedings of *Current Trends in International Fusion Research: A Review*.

R. L. McCrory, D. D. Meyerhofer, S. J. Loucks, S. Skupsky, R. E. Bahr, R. Betti, T. R. Boehly, R. S. Craxton, T. J. B. Collins, J. A. Delettrez, W. R. Donaldson, R. Epstein, J. A. Frenje, V. Yu. Glebov, V. N. Goncharov, D. R. Harding, P. A. Jaanimagi, R. L. Keck, J. H. Kelly, T. J. Kessler, J. P. Knauer, C. K. Li, L. D. Lund, J. A. Marozas, P. W. McKenty, F. J. Marshall, S. F. B. Morse, R. D. Petrasso, P. B. Radha, S. P. Regan, S. Roberts, T. C. Sangster, F. H. Séguin, W. Seka, V. A. Smalyuk, C. Sorce, J. M. Soures, C. Stoeckl, R. P. J. Town, B. Yaakobi, and J. D. Zuegel, "Progress in Direct-Drive Inertial Confinement Fusion Research at the Laboratory for Laser Energetics," to be published in *Nuclear Fusion*.

P. W. McKenty, T. C. Sangster, M. Alexander, R. Betti, R. S. Craxton, J. A. Delettrez, L. Elasky, R. Epstein, A. Frank, V. Yu. Glebov, V. N. Goncharov, D. R. Harding, S. Jin, J. P. Knauer, R. L. Keck, S. J. Loucks, L. D. Lund, R. L. McCrory, F. J. Marshall, D. D. Meyerhofer, S. P. Regan, P. B. Radha, S. Roberts, W. Seka, S. Skupsky, V. A. Smalyuk, J. M. Soures, K. A. Thorp, M. Wozniak, J. A. Frenje, C. K. Li, R. D. Petrasso, F. H. Séguin, K. A. Fletcher, S. Padalino, C. Freeman, N. Izumi, J. A. Koch, R. A. Lerche, M. J. Moran, T. W. Phillips, G. J. Schmid, and C. Sorce, "Direct-Drive Cryogenic Target Implosion Performance on OMEGA," to be published in *Physics of Plasmas* (invited).

B. A. Remington, G. Bazan, J. Belak, E. Bringa, M. Caturla, J. D. Colvin, M. J. Edwards, S. G. Glendinning, D. Ivanov, B. Kad, D. H. Kalantar, M. Kumar, B. F. Lasinski, K. T. Lorenz, J. M. McNaney, D. D. Meyerhofer, M. A. Meyers, S. M. Pollaine, D. Rowley, M. Schneider, J. S. Stölken, J. D. Wark, S. V. Weber, W. G. Wolfer, and B. Yaakobi, "Materials Science Under Extreme Conditions of Pressure and Strain Rate," to be published in *Metallurgical and Materials Transactions A*.

S. Skupsky, J. A. Marozas, R. S. Craxton, R. Betti, T. J. B. Collins, J. A. Delettrez, V. N. Goncharov, P. W. McKenty, P. B. Radha, T. R. Boehly, J. P. Knauer, F. J. Marshall, D. R. Harding, J. D. Kilkenny, D. D. Meyerhofer, T. C. Sangster, and R. L. McCrory, "Polar Direct Drive on the National Ignition Facility," to be published in *Physics of Plasmas* (invited).

X. Teng and H. Yang, "Effects of Surfactants and Synthetic Conditions on the Sizes and Self-Assembly of Monodisperse Iron Oxide Nanoparticles," to be published in the *Journal of Materials Chemistry*.

A. Verevkin, A. Pearlman, W. Slysz, J. Zhang, R. Sobolewski, M. Currie, A. Korneev, G. Chulkova, O. Okunev, P. Kouminov, K. Smirnov, B. Voronov, and G. N. Gol'tsman, "Ultrafast Superconducting Single-Photon Detectors for Near-Infrared-Wavelength Quantum Communications," to be published in the *Journal of Modern Optics*.

B. Yaakobi, D. D. Meyerhofer, T. R. Boehly, J. J. Rehr, B. A. Remington, P. G. Allen, S. M. Pollaine, and R. C. Albers, "Extended X-Ray Absorption Fine Structure Measurements of Laser Shocks in Ti and V and Phase Transformation in Ti," to be published in *Physics of Plasmas* (invited).

B. Yaakobi, D. D. Meyerhofer, T. R. Boehly, J. J. Rehr, B. A. Remington, P. G. Allen, S. M. Pollaine, and R. C. Albers, "Extended X-Ray Absorption Fine Structure Measurements of Laser-Induced V and Ti and Crystal Phase Transformation in Ti," to be published in *Physical Review Letters*.

J. D. Zuegel and D. W. Jacobs-Perkins, "An Efficient, High-Frequency Bulk Phase Modulator," to be published in *Applied Optics*.

Conference Presentations

The following presentations were made at the 87th OSA Annual Meeting, Tucson, AZ, 5–9 October 2003:

S. G. Lukishova, A. W. Schmid, A. J. McNamara, R. W. Boyd, and C. R. Stroud, "Efficient Room Temperature Single-Photon Source: Single Dye Molecule Fluorescence in Photonic-Band-Gap Cholesteric Liquid Crystal Host."

J. R. Marciante, N. O. Farmiga, J. P. Kondis, and J. R. Frederick, "Phase Effects of Secondary Reflections on the Performance of Reflective Liquid-Crystal Cells."

J. R. Marciante, N. O. Farmiga, H. T. Ta, J. I. Hirsh, and M. S. Evans, "Optical Measurement of Depth and Duty Cycle for Binary Diffraction Gratings with Sub- λ Features."

J. R. Marciante and D. H. Raguin, "A New Class of High-Efficiency, High-Dispersion Diffraction Gratings Based on Total Internal Reflection."

J. R. Marciante, D. H. Raguin, J. I. Hirsh, and E. T. Prince, "Polarization-Insensitive High-Dispersion TIR Diffraction Gratings."

The following presentations were made at Education and Training in Optics and Photonics, Tucson, AZ, 6–8 October 2003:

S. D. Jacobs and L. L. Gregg, "OSA Rochester Section Optics Suitcase: A Forty-Minute Middle School Outreach Program for the Cost of a Postage Stamp."

S. D. Jacobs, L. L. Gregg, E. M. Fess, and J. M. Schoen, "Optics Manufacturing Research Projects by Undergraduates Who Happen to be Women."

W. R. Donaldson, J. A. Marozas, R. S. Craxton, D. Jacobs-Perkins, and M. Millecchia, "Spectroscopy of Broadband Harmonic Generation," LEOS 2003, Tucson, AZ, 26–30 October 2003.

The following presentations were made at the 45th Annual Meeting of the APS Division of Plasma Physics, Albuquerque, NM, 27–31 October 2003:

K. Anderson, R. Betti, and J. P. Knauer, "Adiabatic Shaping by Relaxation in Plastic and Cryogenic Shells for Experiments on the OMEGA Laser."

R. Betti and K. Anderson, "Laser-Induced Adiabatic Shaping by Relaxation."

T. R. Boehly, D. G. Hicks, T. J. B. Collins, G. W. Collins, P. M. Celliers, E. Vianello, D. D. Meyerhofer, R. C. Cauble, W. Unites, D. Jacobs-Perkins, R. Earley, M. J. Bonino, W. J. Armstrong, S. G. Noyes, D. Turner, D. Guy, S. Scarantino, T. Lewis, F. A. Rister, and L. D. Lund, "Quartz Equation-of-State (EOS) Measurements at the OMEGA Laser Facility."

M. Canavan, J. R. Rygg, J. A. Frenje, C. K. Li, F. H. Séguin, R. D. Petrasso, S. W. Haan, S. P. Hatchett, J. A. Koch, O. L. Landen, V. Yu. Glebov, D. D. Meyerhofer, and T. C. Sangster,

"The Utility of Knock-On D, T, and P for Diagnosing NIF Implosions."

T. J. B. Collins and S. Skupsky, "High-Gain Direct-Drive Foam Target Designs for the National Ignition Facility."

R. S. Craxton, "Hydrodynamic Simulations of Polar Direct Drive on the NIF and LMJ Based on Three-Dimensional Ray Tracing."

J. DeCiantis, B. E. Schwartz, J. A. Frenje, F. H. Séguin, S. Kurebayashi, C. K. Li, R. D. Petrasso, J. A. Delettrez, J. M. Soures, V. Yu. Glebov, D. D. Meyerhofer, S. Roberts, T. C. Sangster, and S. P. Hatchett, "Studying the Burn Region in ICF Implosions with Proton-Emission Imaging."

J. A. Delettrez, P. B. Radha, C. Stoeckl, S. Skupsky, and D. D. Meyerhofer, "Simulation of Enhanced Neutron Production in OMEGA EP Cryogenic Implosions."

R. Epstein, F. J. Marshall, J. A. Delettrez, P. W. McKenty, P. B. Radha, and V. A. Smalyuk, "Effects of Low-Order Irradiation Nonuniformity on X-Ray Images of ICF Implosions Experiments on OMEGA."

J. A. Frenje, C. K. Li, F. H. Séguin, J. DeCiantis, J. R. Rygg, S. Kurebayashi, B. E. Schwartz, R. D. Petrasso, J. A. Delettrez, V. Yu. Glebov, D. D. Meyerhofer, T. C. Sangster, J. M. Soures, and C. Stoeckl, "Measuring Shock-Coalescence Timing and ρR Evolution of D³He Implosions at OMEGA" (invited).

J. A. Frenje, R. D. Petrasso, C. K. Li, F. H. Séguin, J. DeCiantis, S. Kurebayashi, J. R. Rygg, B. E. Schwartz, J. A. Delettrez, V. Yu. Glebov, D. D. Meyerhofer, T. C. Sangster, J. M. Soures, S. P. Hatchett, S. W. Haan, G. J. Schmid, O. L. Landen, N. Izumi, and D. Stelter, "A Magnetic Recoil Spectrometer (MRS) for ρR_{fuel} and Ti Measurements of Warm, Fizzle, and Ignited Implosions on OMEGA and NIF."

V. Yu. Glebov, C. Stoeckl, T. C. Sangster, P. B. Radha, S. Roberts, S. Mott, S. Padalino, L. Baumgart, K. Voltz, H. M. Jiang, S. P. Hatchett, M. J. Moran, S. Kurebayashi, F. H. Séguin, and R. D. Petrasso, "Secondary Neutron Energy Spectra Measurements with the 1020 Array on OMEGA."

V. Yu. Glebov, C. Stoeckl, S. Roberts, T. C. Sangster, J. A. Frenje, R. D. Petrasso, R. A. Lerche, and R. L. Griffith, "Proton Temporal Diagnostic for ICF Experiments on OMEGA."

- V. N. Goncharov, T. R. Boehly, J. P. Knauer, V. A. Smalyuk, S. P. Regan, O. V. Gotchev, P. W. McKenty, S. Skupsky, P. B. Radha, and D. D. Meyerhofer, "Designing Shock-Timing and Imprint Experiments for the Direct-Drive Inertial Confinement Fusion Implosions."
- O. V. Gotchev, V. N. Goncharov, P. A. Jaanimagi, J. P. Knauer, and D. D. Meyerhofer, "Streaked Imaging of Ablative Richtmyer–Meshkov Growth in ICF Targets on OMEGA."
- L. Guazzotto and R. Betti, "High- β Tokamak Equilibria with Poloidal Flows Exceeding the Poloidal Alfvén Velocity."
- J. P. Knauer, V. N. Goncharov, K. Anderson, R. Betti, V. Yu. Glebov, F. J. Marshall, P. W. McKenty, P. B. Radha, S. P. Regan, T. C. Sangster, C. Stoeckl, J. A. Frenje, C. K. Li, R. D. Petrasso, and F. H. Séguin, "Direct-Drive ICF Implosions with Picket-Fence Pulse Shapes."
- J. P. Knauer, S. Sublett, T. J. B. Collins, A. Frank, I. V. Igumenshchev, D. D. Meyerhofer, A. Poludnenko, J. M. Foster, P. A. Rosen, P. Keiter, B. H. Wilde, B. Blue, T. S. Perry, H. F. Robey, A. M. Khokhlov, and R. P. Drake, "Development of a Test Bed for Astrophysical Jet Hydrodynamics."
- S. Kurebayashi, F. H. Séguin, J. A. Frenje, C. K. Li, R. D. Petrasso, J. R. Rygg, B. E. Schwartz, J. DeCiantis, V. Yu. Glebov, J. A. Delettrez, T. C. Sangster, J. M. Soures, and S. P. Hatchett, "Investigation of the Use of Secondary Protons and Neutrons for Studying Fuel Areal Density in Imploded, D₂-Filled Capsules."
- J. A. Marozas, P. B. Radha, T. J. B. Collins, P. W. McKenty, and S. Skupsky, "Optimization of Low-Order Uniformity for Polar Direct Drive on the National Ignition Facility (NIF)."
- F. J. Marshall, J. A. Delettrez, R. Epstein, R. Forties, V. Yu. Glebov, J. H. Kelly, T. J. Kessler, J. P. Knauer, P. W. McKenty, S. P. Regan, V. A. Smalyuk, C. Stoeckl, J. A. Frenje, C. K. Li, R. D. Petrasso, and F. H. Séguin, "Direct-Drive Implosions on OMEGA with Optimized Illumination Uniformity."
- A. V. Maximov, J. Myatt, R. W. Short, W. Seka, and C. Stoeckl, "Modeling of the Two-Plasmon-Decay Instability Driven by Incoherent Laser Beams."
- P. W. McKenty, T. C. Sangster, J. A. Delettrez, R. Epstein, V. Yu. Glebov, D. R. Harding, J. P. Knauer, R. L. Keck, S. J. Loucks, L. D. Lund, R. L. McCrory, F. J. Marshall, D. D. Meyerhofer, S. F. B. Morse, S. P. Regan, P. B. Radha, W. Seka, S. Skupsky, V. A. Smalyuk, J. M. Soures, C. Stoeckl, K. A. Thorp, J. A. Frenje, C. K. Li, R. D. Petrasso, F. H. Séguin, K. A. Fletcher, S. Padalino, and C. Freeman, "Experimental Results from Cryogenic D₂ Implosions on the OMEGA Laser."
- H. Sawada, S. P. Regan, V. N. Goncharov, J. P. Knauer, R. Epstein, R. S. Craxton, J. A. Delettrez, F. J. Marshall, B. Yaakobi, D. D. Meyerhofer, W. Seka, M. Alexander, R. S. Craxton, M. D. Wittman, M. Pandina, L. S. Iwan, L. M. Elasky, D. R. Harding, T. J. Kessler, R. L. Keck, L. D. Lund, D. Weiner, A. Warrick, T. G. Brown, and C. Cotton, "Cryogenic Target Characterization at LLE."
- J. Myatt, A. V. Maximov, R. W. Short, J. A. Delettrez, and C. Stoeckl, "Intense Electron-Beam Transport in Dense Cryogenic DT Fast-Ignition Fusion Targets."
- R. D. Petrasso, J. R. Rygg, C. K. Li, F. H. Séguin, S. P. Hatchett, V. Yu. Glebov, D. D. Meyerhofer, T. C. Sangster, and J. M. Soures, "Experimental Studies of Time-Dependent Mix in OMEGA Direct-Drive Implosions."
- S. P. Regan, H. Sawada, V. A. Smalyuk, V. N. Goncharov, J. A. Delettrez, P. B. Radha, R. Epstein, F. J. Marshall, B. Yaakobi, D. D. Meyerhofer, T. C. Sangster, and D. A. Haynes, Jr., "Diagnosing Shell Mix in Direct-Drive with Time-Resolved X-Ray Spectroscopy."
- J. R. Rygg, F. H. Séguin, C. K. Li, J. A. Frenje, R. D. Petrasso, S. P. Hatchett, J. A. Delettrez, V. Yu. Glebov, V. N. Goncharov, R. L. Keck, J. P. Knauer, F. J. Marshall, D. D. Meyerhofer, T. C. Sangster, and V. A. Smalyuk, "The Effects of Implosion Asymmetry on Shock Dynamics in OMEGA Direct-Drive Experiments."
- T. C. Sangster, J. A. Delettrez, R. Epstein, V. Yu. Glebov, V. N. Goncharov, D. R. Harding, D. Jacobs-Perkins, R. L. Keck, J. D. Kilkenny, J. P. Knauer, S. J. Loucks, L. D. Lund, R. L. McCrory, P. W. McKenty, J. A. Marozas, F. J. Marshall, D. D. Meyerhofer, S. F. B. Morse, S. P. Regan, P. B. Radha, W. Seka, S. Skupsky, V. A. Smalyuk, J. M. Soures, C. Stoeckl, K. A. Thorp, J. A. Frenje, C. K. Li, R. D. Petrasso, F. H. Séguin, K. A. Fletcher, S. Padalino, and C. Freeman, "Experimental Results from Cryogenic D₂ Implosions on the OMEGA Laser."

Meyerhofer, P. B. Radha, T. C. Sangster, and W. Seka, "Experimental Investigation of Coronal Plasma Conditions in Direct-Drive ICF Using Time-Resolved X-Ray Spectroscopy."

F. H. Séguin, J. R. Rygg, J. A. Frenje, C. K. Li, R. D. Petrasso, V. Yu. Glebov, V. N. Goncharov, J. P. Knauer, J. P. Marshall, D. D. Meyerhofer, T. C. Sangster, V. A. Smalyuk, J. M. Soures, and S. P. Hatchett, "Measuring Time Evolution of Areal-Density Asymmetries in OMEGA Direct-Drive Implosions."

W. Seka, C. Stoeckl, A. V. Maximov, R. S. Craxton, R. W. Short, S. P. Regan, H. Baldis, S. Depierreux, J. Myatt, and R. E. Bahr, "Experimental Investigation of the Two-Plasmon-Decay Instability at Oblique Incidence."

R. W. Short, "On the Role of Electron-Acoustic Waves in Two-Plasmon Decay and Stimulated Raman Scattering."

A. Simon and R. W. Short, "Convective Growth of the Three-Wave Parametric Instability in a Nonuniform Plasma."

S. Skupsky, J. A. Marozas, R. S. Craxton, R. Betti, T. J. B. Collins, J. A. Delettrez, V. N. Goncharov, P. W. McKenty, P. B. Radha, T. R. Boehly, J. P. Knauer, F. J. Marshall, D. R. Harding, J. D. Kilkenny, D. D. Meyerhofer, T. C. Sangster, and R. L. McCrory, "Polar Direct Drive on the National Ignition Facility" (invited).

J. M. Soures, S. J. Loucks, R. L. McCrory, D. D. Meyerhofer, S. F. B. Morse, T. C. Sangster, and C. Stoeckl, "Inertial Confinement Fusion and High-Energy-Density Physics Research Opportunities at the National Laser Users' Facility (NLUF)."

C. Stoeckl, J. A. Delettrez, T. C. Sangster, R. B. Stephens, S. P. Hatchett, J. A. Frenje, S. Fujioka, H. Shiraga, and K. A. Tanaka, "Fuel Assembly Experiments with Fast-Ignitor Cone Targets on OMEGA."

S. Sublett, J. P. Knauer, H. F. Robey, and B. Blue, "Development of a Point Projection Backlighter for Laboratory Astrophysics Experiments on OMEGA."

W. Theobald, L. Veisz, and R. Sauerbrey, "Three-Halves-Harmonic Generation in Femtosecond-Laser-Produced, Solid-Density Plasmas."

E. Vianello, T. R. Boehly, R. S. Craxton, V. N. Goncharov, J. P. Knauer, D. D. Meyerhofer, J. E. Miller, T. C. Sangster, D. G. Hicks, and P. M. Celliers, "Timing of Multiple Shocks in Planar Direct-Drive Laser-Driven Targets."

B. Yaakobi, D. D. Meyerhofer, T. R. Boehly, J. J. Rehr, B. A. Remington, P. G. Allen, S. M. Pollaine, and R. C. Albers, "Extended X-Ray Absorption Fine Structure Measurements of Laser Shocks in Ti and V and Phase Transformation in Ti" (invited).

I. V. Igumenshchev, "Radiatively Inefficient Accretion Flows," Stellar-Mass, Intermediate-Mass, and Supermassive Black Holes, Kyoto, Japan, 28–31 October 2003.

D. R. Harding, F.-Y. Tsai, E. L. Alfonso, S. H. Chen, A. K. Knight, and T. N. Blanton, "Properties of Vapor-Deposited Polyimide Films," Third International Symposium on Polyimides and Other High Temperature Polymers, Orlando, FL, 17–19 December 2003 (invited).

UNIVERSITY OF
ROCHESTER